

# **NITROGEN and ARGON TREATMENT of TITANIUM DIOXIDE NANOWIRE ARRAYS**

**A Dissertation in  
Physics  
by  
Ian Patrick Cupido**

Submitted in partial fulfilment of the requirements of  
for Degree of Magister of Scientiae  
in the Discipline of Physics

**Supervisor:**

**Dr FR Cummings, University of the Western Cape (UWC)**

Department of Physics and Astronomy  
University of the Western Cape

UNIVERSITY of the  
WESTERN CAPE



**UNIVERSITY of the  
WESTERN CAPE**

March 2021

## COPYRIGHT STATEMENT

Copyright © 2020 by Ian Patrick Cupido

All rights reserved. No part of this publication may be reproduced, stored in a retrieval system, or transmitted, in any form or by any means (including and withholding electronic, mechanical, photocopying, recording or otherwise) without prior written permission from the author.





UNIVERSITY *of the*  
WESTERN CAPE

**To my parents**

# Acknowledgments

---

**I am extremely grateful to the following people and organisations for the assistance, guidance and support given. Without whom, this thesis would not have been completed.**

Many thanks I can express to my supervisor, Dr Franscious Cummings. This thesis and subsequent completion are a direct result of his guidance and help. His continued support renewed my motivation to overcome difficulties I experienced.

I sincerely express my gratitude to all the students and staff of the University of the Western Cape Department of Physics and Astronomy who assisted me.

To my parents, Dennis and Deidre, for your belief in me, for your continuous love, support in times of need and constant encouragement.

To my immediate and extended family and friends, for their encouragement and support:

Pepper, Jennifer, Lyle, Patrick, Freda, Christina, Friedel, Benjamin, Noline, Judy, Walter, Clive, Gary, Adele, Jarred, Natasha, Tarryn, Bianca, Byron, Danielle, Conroy.

Timothy, Matthew, Fabian, Leyanda, Asheley, Amy, Esmond, Lionel, FFloyd, Emmanuel, Lerato, Muhammed, Sihle, Captain.

The National Research Foundation (NRF) and University of the Western Cape for the financial support during this study.



# Declaration

---

I declare that

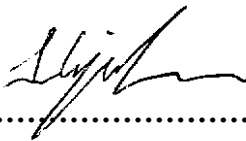
**“NITROGEN and ARGON TREATMENT of TITANIUM  
DIOXIDE NANOWIRE ARRAYS”**

is my own work, that has not been submitted for any degree or examination in any other university, and that all sources I have used or quoted have been indicated and acknowledged by means of complete references

Ian Patrick Cupido

March 2021

Signature: .....



.....

# Keywords

---

Photovoltaics

Electron Transport Layer

Nanowires

Nanostructures

Nanoscience

Hydrothermal Synthesis

Plasma Treatment

Scanning Electron Microscopy

X-Ray Diffraction

X-Ray Photoelectron Spectroscopy

Ultraviolet-Visible Spectroscopy

Substitutional

Interstitial



# Abstract

---

TiO<sub>2</sub> nanoparticle films are important electron transport layers (ETLs) in photovoltaics such as dye-sensitised, perovskite and polymer hetero-junction solar cells. These films, however, have significant electron trap-sites as a result of the large density of oxygen vacancies present in nano-sized TiO<sub>2</sub>. These trap-sites cause electron-hole recombination and ultimately lower photon-to-current conversion efficiency of the underlying cell during operation. Doping the TiO<sub>2</sub> lattice with low atomic number elements such as nitrogen is a proven method to overcoming the charge transport inefficiency of TiO<sub>2</sub> ETLs; another is the use of one-dimensional (1D) nanowires (NWs), instead of nanoparticles.

Modification of TiO<sub>2</sub> with non-metals leads to optical bandgap narrowing, improvement in electron conductivity and increased electron lifetime in the ETL layer. However, a lot of scope exists in understanding and fully quantifying the relationship between optical property, for example light transmission and bandgap modification, versus the doping concentration and type. Most doping approaches are in-situ and involve the addition of a dopant precursor (usually a salt) during the synthesis of TiO<sub>2</sub> nanostructures – this invariably leads to uncontrolled doping levels, anion contamination and poor-quality materials – a need thus exists to develop simple, controllable doping approaches. One such approach, which forms the basis of this study, is ex-situ doping by means of plasma generated species in a controlled environment. This field of study is fairly novel and not widely studied, requiring more research to understand the doping mechanisms and influence on the optical and electronic properties of the underlying nanomaterials. In particular, controlled doping of TiO<sub>2</sub> with nitrogen using radio-frequency generated (RF) plasma requires vigorous experimentation and characterisation. Inaccuracy of the deposition parameters during exposure remains a common drawback for this approach in addition to a lack of understanding of the surface interaction between the N<sub>2</sub> species and specimen during irradiation.

Based on these knowledge gaps this study focuses on investigating the formation of the Ti-N bonding network in the TiO<sub>2</sub> lattice upon exposure of hydrothermally-synthesised TiO<sub>2</sub> NWs with an RF generated nitrogen plasma and observing its influence on the measured light transmission

through the nanowire array; light transmission through the nanowire arrays is an important parameter to investigate if they are to be used as ETLs in photovoltaics. Three plasma parameters are investigated in rigour in this work, namely the plasma power, time of exposure and the specimen (or substrate) temperature during irradiation.

Morphological and structural studies using scanning (SEM) and transmission electron microscopy (TEM) show that nitrogen doping under increasing plasma power (from 100W to 500W) leads to the dissociation of the electrostatic Van der Waals forces bundling the nanowires, subsequently resulting in decreased areal density due to non-alignment of the NW array. This, in turn, leads to improved light transmission and red-shift of the absorption curve, both of which are advantageous for photovoltaic applications. These positive findings are ascribed to the higher nitrogen doping concentrations at higher plasma power as shown by x-ray photoelectron spectroscopy (XPS) studies. By making use of the Williamson-Hall (WH) method during X-ray diffraction (XRD) studies, it is shown that the high nitrogen doping concentration at high plasma power leads to a decrease in the lattice parameters of the rutile TiO<sub>2</sub> lattice.

Similarly, SEM micrographs show that increasing the exposure time allows the plasma radicals to significantly distort the Van Der Waals electrostatic forces and as such the orientation of the nanowires to the substrate. XPS spectra show a decrease in the O-O bonding network in the bulk of the sample with increasing nitrogen plasma exposure time. This decrease coincides with an increase of the surface Ti-OH bonds, which may be a result of increased substitutional N-Ti-O and Ti-N as the oxygen bonds are decreasing. However, it is found that the best light transmission and red shift occur at a plasma exposure of 10 mins, using a plasma power of 100W which may not generate nitrogen radicals with sufficient kinetic energy allowing for deep-level doping in the TiO<sub>2</sub> lattice. This is supported by WH studies which show minimal lattice parameter distortion at high exposure periods.

Increasing the specimen temperature from room temperature to 300 °C during irradiation leads to similar trends in the SEM micrographs to that observed when increasing the plasma power, thus leading to a conclusion that the chemical states of the nitrogen doped in the TiO<sub>2</sub> may be and coexist in the form of substitutional N-Ti-O and Ti-N, also as interstitial NO/ NO<sub>2</sub> can be made.

These multi-type nitrogen doping species can induce the formation of new energy levels in the forbidden band of TiO<sub>2</sub> and relate to the enhancement of photo-catalytic activity in the visible range for controlled fabrication. It is thus inferred that TiO<sub>2</sub> nanowires are successfully implanted with N atoms during plasma irradiation with advantageous optical transmission shifts towards longer wavelengths under an optimised experimental condition of 300W, 30 min exposure and a substrate temperature of 100°C.



# Table of Contents

---

<i>NITROGEN and ARGON TREATMENT of TITANIUM DIOXIDE NANOWIRE ARRAYS</i> .....	i
Dedication.....	iii
Acknowledgements.....	iv
Declaration.....	v
Keywords.....	vi
Abstract.....	vii
<b>CHAPTER 1: Introduction</b> .....	<b>11</b>
1.1 Background.....	11
1.2 Generations of Photovoltaics.....	12
1.3 TiO <sub>2</sub> Semiconductor.....	13
1.4 Aims and Outline.....	15
References.....	18
<b>CHAPTER 2: Literature Review of TiO<sub>2</sub></b> .....	<b>20</b>
2.1 Structure of TiO <sub>2</sub> .....	20
2.2 Thermodynamic Properties.....	22
2.3 Electronic Properties of Rutile TiO <sub>2</sub> .....	24
2.3.1 Band Structure.....	24
2.3.2 Density of States.....	25
2.3.3 Electron Density.....	27
2.4 Optical Properties of Rutile TiO <sub>2</sub> .....	29
2.5 Methods of Synthesis of Rutile TiO <sub>2</sub> .....	33
2.5.1 Physical Vapour Deposition.....	33
2.5.2 Chemical Vapour Deposition.....	34
2.5.3 Electrochemical Anodisation.....	35
2.5.4 Hydrothermal Synthesis.....	35
2.6 Growth Models of TiO <sub>2</sub> .....	36

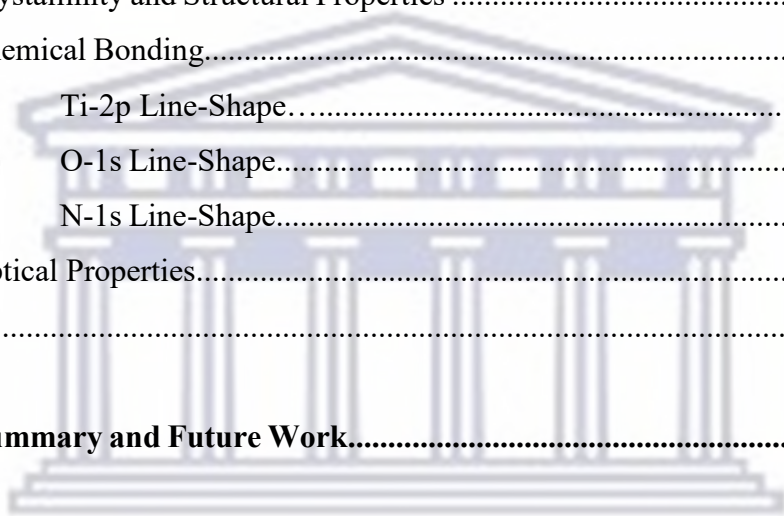
2.6.1	Vapour-Liquid-Solid Growth Model (VLS).....	36
2.6.2	Vapour-Solid Growth Model (VS).....	37
2.7	Doping of TiO <sub>2</sub> .....	38
2.8	Plasma Treatment.....	39
2.8.1	Overview.....	39
2.8.2	Types of Species.....	40
2.9	TiO <sub>2</sub> Doping with Plasma.....	41
2.10	TiO <sub>2</sub> as an Electron Transport Layer (ETL) .....	42
2.11	Summary.....	42
	References.....	43
<b>CHAPTER 3: Experimental and Analytical Techniques.....</b>		<b>48</b>
3.1	Introduction.....	48
3.2	Hydrothermal Synthesis.....	49
3.3	Plasma Vapour Deposition of Nitrogen Treatment.....	53
3.4	Effect of Plasma on Surfaces.....	53
3.5	Experimental Procedure.....	54
3.5.1	Substrate Preparation.....	54
3.5.2	TiO <sub>2</sub> Nanowire Growth.....	56
3.5.3	Plasma Treatment.....	56
	Analytical Techniques.....	58
3.6	Scanning Electron Microscopy.....	58
3.6.1	Introduction.....	58
3.6.2	Resolution of the SEM.....	59
3.6.3	Working Distance, Depth of Field and Depth of Focus.....	63
3.6.4	Secondary Electrons and Image Formation.....	63
3.6.5	The Scattering of Electrons by Atoms.....	66
3.6.6	The Preparation for the Specimen in the SEM.....	67
3.7	X-Ray Diffraction.....	68
3.7.1	Introduction.....	68
3.7.2	Crystal Structure and Bravais Lattices.....	68



3.7.3	Bragg's Law for Diffraction.....	72
3.7.4	Instrumentation.....	74
3.7.5	Grazing-Incidence X-Ray Diffraction.....	74
3.7.6	Characterisation.....	75
3.8	X-Ray Photoelectron Spectroscopy.....	76
3.8.1	Introduction.....	76
3.8.2	Principles of XPS.....	76
3.8.3	Preparing and Mounting Samples.....	79
3.8.4	Experimental Setup.....	80
3.9	Ultraviolet-Visible Spectroscopy for Transmission.....	81
3.9.1	Introduction.....	81
3.9.2	Principles of UV-Vis.....	81
3.9.3	Experimental Setup.....	82
3.9.4	Charaterisation.....	82
	References.....	84
<b>CHAPTER 4: Results and Discussion .....</b>		<b>87</b>
4.1	Hydrothermal Growth of TiO <sub>2</sub> Nanowires on FTO.....	87
4.2	Effect of Nitrogen Plasma Power on the Morphological, Structural and Optical Properties of Individual TiO <sub>2</sub> Nanowires.....	89
4.2.1	TiO <sub>2</sub> Nanowire Morphology.....	90
4.2.2	Crystallinity and Structural Properties.....	92
4.2.3	Chemical Bonding.....	95
	(a) Ti-2p Line-Shape.....	95
	(b) O-1s Line-Shape.....	98
	(c) N-1s Line-Shape.....	101
4.2.4	Optical Properties.....	102
4.3	Effect of Extended Exposure Time on the Morphological, Structural and Optical Properties of Individual TiO <sub>2</sub> Nanowires.....	106
4.3.1	TiO <sub>2</sub> Nanowire Morphology.....	106
4.3.2	Crystallinity and Structural Properties .....	109



4.3.3	Chemical Bonding.....	111
(a)	Ti-2p Line-Shape.....	111
(b)	O-1s Line-Shape.....	113
(c)	N-1s Line-Shape.....	115
4.3.4	Optical Properties.....	118
4.4	Effect of FTO Substrate Temperature on the Morphological, Structural and Optical Properties of Individual TiO <sub>2</sub> Nanowires.....	119
4.4.1	TiO <sub>2</sub> Nanowire Morphology.....	119
4.4.2	Crystallinity and Structural Properties .....	121
4.4.3	Chemical Bonding.....	124
(a)	Ti-2p Line-Shape.....	124
(b)	O-1s Line-Shape.....	126
(c)	N-1s Line-Shape.....	128
4.4.4	Optical Properties.....	131
	References.....	133
	<b>CHAPTER 5: Summary and Future Work.....</b>	<b>136</b>



UNIVERSITY of the  
WESTERN CAPE

# List of Figures

---

Fig. 1.1	Solar cell current efficiencies throughout the years for the different types of solar cells and best research-cell efficiencies. The world record efficiency of a solar cell is 46.0%, which was achieved by a four-junction solar cell.....	13
Fig. 1.2	Schematic representation of the components of a dye-sensitized solar cell.....	14
Fig. 1.3	(a) The structure and (b) energy level diagram of a perovskite PV cell.....	15
Fig. 2.1	(left) Tetragonal rutile and anatase TiO <sub>2</sub> structure. (right) Assembly bulk stacked patterns of rutile and anatase TiO <sub>2</sub> .....	20
Fig. 2.2	Enthalpies of the different phases of TiO <sub>2</sub> .....	22
Fig. 2.3	Electronic band structure of TiO <sub>2</sub> along high symmetry directions. With the top valence band taken as the zero of energy.....	23
Fig. 2.4	Density of states for TiO <sub>2</sub> in states/eV/spin/unit cell compared to experimental UPS for the TiO <sub>2</sub> (110) surface at a photon energy of 46 eV and the TiO <sub>2</sub> XAS spectra of the O1s edge.....	25
Fig. 2.5	Pseudo-atom valence density difference maps for the (a) (110) and (b) (110) lattice planes. Contours of constant charge density are separated by 3e/V <sub>o</sub> . In (c) it is seen that the experimental electron density map in the (110) plane.....	27
Fig. 2.6	Pseudo-charge-density contour plot of the (a) e <sub>g</sub> , (b) t <sub>2g</sub> and (c) upper O2p valence bands in the (110) lattice plane. Contours of constant charge density are separated by 10e/V <sub>p</sub> .....	29
Fig. 2.7	Imaginary part of the dielectric function for polarisation vector (a) perpendicular and (b) parallel to the c-axis. Present results (solid line) are compared to the experimental room-temperature results of Cardona <i>et al.</i> .....	31
Fig. 3.1	SEM micrograph of the cross section showing TiO <sub>2</sub> nanowire array grown in toluene on TCO substrate.....	50
Fig. 3.2	SEM micrograph showing TiO <sub>2</sub> nanowire array grown using water as a solvent.....	51
Fig. 3.3	Schematic of the plasma vapour deposition system.....	52

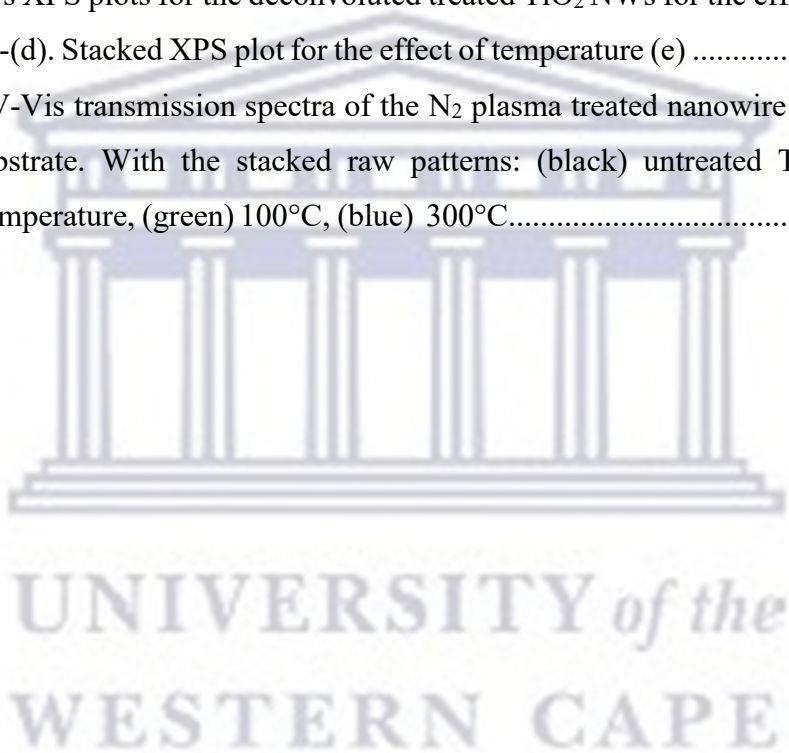
Fig. 3.4	Schematic representation of the autoclave high-pressure vessel and the associated growth process of the TiO <sub>2</sub> nanowire array at the experimental conditions used in this study.....	54
Fig. 3.5	Image of the plasma vapour deposition system used for N <sub>2</sub> treatment.....	56
Fig. 3.6	Images of (Top) Vacutech loading chamber with nanowire arrays fitted onto heat-able substrate (Bottom) red-glowing N <sub>2</sub> plasma irradiating the nanowire film.....	56
Fig. 3.7	Airy rings due to the diffraction of a laser beam by small pinholes left: 75um and right: 100um.....	58
Fig. 3.8	Variation of light intensity across a set of Airy rings. Corresponding most intense region being d <sub>1</sub> .....	59
Fig. 3.9	Intensity of airy rings from two neighbouring pinholes. Solid lines show intensity distributions. dotted line shows combined profile.....	60
Fig. 3.10	Definition of half-angle alpha, subtended by an aperture, in this case the objective aperture.....	60
Fig. 3.11	Depth of field of an optical system showing both the aperture and the plane of optimum focus.....	61
Fig. 3.12	Usable SEM signals that originate from the specimen as result of the incident beam and surface interaction.....	63
Fig. 3.13	Interaction volume and detection regions for secondary electrons, backscattered electrons and X-rays.....	63
Fig. 3.14	(a) Secondary electron generation. (b) Secondary electron spatial distribution.....	64
Fig. 3.15	Schematic of a point lattice.....	68
Fig. 3.16	Indices for directions of a general unit cell, with the diagonal indices included.....	70
Fig. 3.17	Relationship between the reciprocal lattice vector and the crystal plane (hkl).....	70
Fig. 3.18	Conditions for Bragg's Law shown for the interaction of X-rays with the normal plane.....	72
Fig. 3.19	Schematic of a conventional X-ray diffractometer.....	73
Fig. 3.20	Schematic of GIXRD geometry on InAs nanowires grown on an InP substrate....	74
Fig. 3.21	XRD spectra of TiO <sub>2</sub> NWs grown at different concentrations.....	74
Fig. 3.22	Relative binding energies for an atom.....	77
Fig. 3.23	Schematic for the XPS spectrograph with main components shown.....	78

Fig. 3.24	Illustration for the Electromagnetic spectrum.....	80
Fig. 3.25	Schematic of a conventional spectrophotometer system.....	81
Fig. 3.26	Transmission spectra for TiO <sub>2</sub> thin films grown at different Ar/O <sub>2</sub> ratios.....	82
Fig. 4.1	SEM micrograph of the as-synthesised nanowire array on the FTO substrate. The inset in the top-right corner shows the top-view and a high-resolution micrograph of the nanowire structure, in which individual nano-fingers, as discussed by Wisnet et al , can be observed.....	87
Fig. 4.2	TEM micrograph of an individual TiO <sub>2</sub> nanowire grown for 3 hours at 150 °C in a hydrothermal solution consisting of 2 ml HCl, 10 ml of H <sub>2</sub> O and 0.25 ml TBT (top-right) high-resolution micrograph indicating the growth direction of an individual nanowire; (bottom-right) zoomed-in micrograph highlighting the nano-fingers.....	88
Fig. 4.3	<i>Top Row:</i> 100 W plasma treatment: (a) untreated, (a') treated, (a'') cross-section; <i>Middle Row:</i> 300 W plasma treatment: (b) untreated, (b') treated, (b'') cross-section. <i>Bottom Row:</i> 500 W plasma treatment: (c) untreated, (c') treated, (c'') cross-section. For all irradiated samples, the time of exposure and substrate temperature are fixed at 10 mins and room temperature, respectively.....	90
Fig. 4.4	W-H plots: (a) untreated TiO <sub>2</sub> , (b) 100 W, (c) 300W, (d) 500W. (e) Stacked raw GIXRD patterns.....	93
Fig. 4.5	Ti-2p plots showing the deconvolution of the peak profiles for (a) untreated, (b) 100 W (c) 300 W and (d) 500 W irradiated TiO <sub>2</sub> nanowire arrays; (e) Stacked plot directly comparing the changes in line-shapes. For all irradiated samples, the time of exposure and substrate temperature are fixed at 10 mins and room temperature, respectively.....	96
Fig. 4.6	O-1s plots showing the deconvolution of the peak profiles for (a) untreated, (b) 100 W (c) 300 W and (d) 500 W irradiated TiO <sub>2</sub> nanowire arrays; (e) Stacked plot directly comparing the changes in line-shapes.....	99
Fig. 4.7	N-1s plots showing the deconvolution of the peak profiles for (a) untreated, (b) 100 W (c) 300 W and (d) 500 W irradiated TiO <sub>2</sub> nanowire arrays; (e) Stacked plot directly comparing the changes in line-shapes.....	102

Fig. 4.8	UV-Vis transmission spectra of the N <sub>2</sub> plasma treated nanowire array on the FTO substrate. With the stacked raw patterns: (black) untreated TiO <sub>2</sub> , (red) 100 W, (green) 300W, (blue)500W.....104
Fig. 4.9	<i>Top Row</i> : 10 mins plasma treatment: (a) untreated, (a') treated, (a'') cross-section; <i>Middle Row</i> : 30 min plasma treatment: (b) untreated, (b') treated, (b'') cross-section. <i>Bottom Row</i> : 60 min plasma treatment: (c) untreated, (c') treated, (c'') cross-section. For all irradiated samples, the plasma power and substrate temperature are fixed at 100W and room temperature, respectively.....107
Fig. 4.10	Williamson-Hall plot for: (a) untreated TiO <sub>2</sub> , (b) Nitrogen treated TiO <sub>2</sub> NWs for 10 mins and (c) Nitrogen treated TiO <sub>2</sub> NWs 30 mins at 100 W and the substrate at room temperature. (d) Stacked raw GIXRD data for (hkl) planes of the time series.....109
Fig. 4.11	Ti-2p plots showing the deconvolution of the peak profiles for a) as-synthesised, (b) 10-min (c) 30-min and (d) 60-min exposed TiO <sub>2</sub> nanowire arrays; (e) Stacked plot directly comparing the changes in line-shapes. For all irradiated samples, the plasma power and substrate temperature are fixed at 100W and room temperature, respectively.....111
Fig. 4.12	O-1s plots showing the deconvolution of the peak profiles for (a) as-synthesised, (b) 10-min (c) 30-min and (d) 60-min exposed TiO <sub>2</sub> nanowire arrays; (e) Stacked plot directly comparing the changes in line-shapes.....113
Fig. 4.13	N-1s plots showing the deconvolution of the peak profiles for (a) as-synthesised, (b) 10- (c) 30- and (d) 60-min exposed TiO <sub>2</sub> nanowire arrays; (e) Stacked plot directly comparing the changes in line-shapes.....115
Fig. 4.14	UV-Vis transmission spectra of the N <sub>2</sub> plasma treated nanowire array on the FTO substrate. With the stacked raw patterns: (black) untreated TiO <sub>2</sub> , (red) 10 min, (green) 30 min, (blue) 60 min.....117
Fig. 4.15	<i>Top Row</i> : Room temperature irradiation: (a) untreated, (a') treated, (a'') cross-section; <i>Middle Row</i> : 100 °C irradiation: (a) untreated, (b') treated, (b'') cross-section. <i>Bottom Row</i> : 300 °C irradiation: (c) untreated, (c') treated, (c'') cross-section. For all irradiated samples, the time of exposure and plasma power are fixed at 10 mins and 100 W, respectively.....119



Fig. 4.16	Williamson-Hall plot for: (a) untreated TiO <sub>2</sub> , (b) Nitrogen treated TiO <sub>2</sub> NWs at RT. (c) Nitrogen treated TiO <sub>2</sub> NWs at 100°C and (d) Nitrogen treated TiO <sub>2</sub> NWs 300°C. (3) Stacked raw GIXRD data for (hkl) planes of the temperature series.....121
Fig. 4.17	Ti2p XPS plots for the deconvoluted treated TiO <sub>2</sub> NWs for the effect of temperature (a)-(d). Stacked XPS plot for the effect of temperature (e).....124
Fig. 4.18	O1s XPS plots for the deconvoluted treated TiO <sub>2</sub> NWs for the effect of temperature (a)-(d). Stacked XPS plot for the effect of temperature (e) .....126
Fig. 4.19	N1s XPS plots for the deconvoluted treated TiO <sub>2</sub> NWs for the effect of temperature (a)-(d). Stacked XPS plot for the effect of temperature (e) .....128
Fig. 4.20	UV-Vis transmission spectra of the N <sub>2</sub> plasma treated nanowire array on the FTO substrate. With the stacked raw patterns: (black) untreated TiO <sub>2</sub> , (red) Room Temperature, (green) 100°C, (blue) 300°C.....131



# List of Tables

---

Table 2.1	Experimental structure in the imaginary part of the dielectric function of Cardona et al compared to the present first-principles results for polarisations perpendicular and parallel to the c-axis.....	32
Table 3.1	Analytical techniques for the study of N <sub>2</sub> plasma treated TiO <sub>2</sub> nanowires.....	57
Table 3.2	Simplified description of the fourteen Bravais lattices.....	69
Table 4.1	Summary of the diameter and length of the nanowire arrays before and after plasma irradiation at increasing plasma power.....	91
Table 4.2	Calculated Structural properties for the effect of power series treated TiO <sub>2</sub> .....	93
Table 4.3	Relative quantum efficiencies of the de-convoluted Ti-2p.....	97
Table 4.4	Relative quantum efficiencies of the de-convoluted O-1s peaks.....	100
Table 4.5	Relative quantum efficiencies of the de-convoluted N-1s peaks.....	103
Table 4.6	Summary of the diameter and length of the nanowire arrays before and after plasma irradiation at increasing exposure time.....	108
Table 4.7	Calculated structural properties of the as-synthesised TiO <sub>2</sub> versus 10- and 30-min plasma exposure time.....	110
Table 4.8	Relative quantum efficiencies of the de-convoluted Ti-2p.....	112
Table 4.9	Relative quantum efficiencies of the de-convoluted O-1s.....	114
Table 4.10	Relative Quantum efficiencies of the de-convoluted N1s.....	116
Table 4.11	Summary of the diameter and length of the nanowire arrays before and after plasma irradiation at increasing substrate annealing temperature.....	120
Table 4.12	Calculated Structural properties for the effect of temperature for treated TiO <sub>2</sub> .....	122
Table 4.13	Relative quantum efficiencies of the de-convoluted Ti-2p.....	125
Table 4.14	Relative quantum efficiencies of the de-convoluted O-1s.....	127
Table 4.15	Relative Quantum efficiencies of the de-convoluted N1s.....	130

# Chapter 1: Introduction

---

## 1.1 Background

As the demand for fossil fuels increases and strategic reserves of coal and oil run dry, internationally there is a growing concern to supplement these energy sources. World nations are investing and developing new technologies to secure future energy supplies, with more focus centred on alternative and green energy, due to issues of climate change, environmental protection and independence from nations with larger fossil reserves [1.1]. To address global energy consumption, future electricity generation needs to be able to keep up with demand, be widely available, relatively cheap and most of all, safe to use. A few exciting generation methods are: wind power, oceanic power, nuclear power and solar power, with varying levels of design, cost and expertise needed for research and development.

For a direct comparison of each of the types of electrical generation methods mentioned above, it is seen that wind power in particular has the disadvantage of being dependent on seasonal winds and constant maintenance. Ocean power is currently extremely expensive due to the inability to manufacture facilities large enough to ensure adequate electrical generation. Nuclear power, like ocean power, is expensive and requires a number of safety procedures and processes to be rendered usable [1.2, 1.3]. Solar power presents the most logical and smart investment for generating relatively inexpensive electricity for future generations. This can be seen from the fact that photovoltaic (PV) devices (or solar cells) convert sunlight directly into electricity, making it easy to use. Solar cells can be grown in commercial labs relatively easily with consistent results. Add to this, sunlight directs  $4.3 \times 10^{20}$  J [1.4] of energy to the earth in one hour, which is comparable to the entire energy consumption of the world in 2001 [1.5].



## 1.2 Generations of Photovoltaics

Photovoltaics can be classified into three or four generations of devices, with silicon-based cells being the first breakthrough, first developed by Chapin *et al* [1.6] in 1954. The second generation of cells were based on thin-film solar cells in the 1960s. While the third generation of photovoltaics are largely based on dye-sensitised cells, perovskite, organic and inorganic cells, first developed in the 1990s [1.7].

The major drawback preventing large-scale commercialisation of different PV technologies has been their low sunlight-to-electricity conversion efficiencies, compared to traditional fossil-based methods. Fig. 1.1 shows the progress of the efficiencies over the years for different types of solar cells [1.8]. First generation silicon-based cells have a trend of attaining a relatively high efficiency of 20 percent for polycrystalline silicon and around 27 percent efficiency for single crystal silicon. This high efficiency coupled with vast research into development and production of silicon have made solar cells of this nature dominant in use. Limiting factors, however, include high production cost and possible environmental issues resulting from fabrication.

Current research is thus focusing on developing suitably cost-effective methods to substitute the traditional manufacturing processes, while maintaining the same efficiency [1.9]. Third generation dye-sensitised solar cells (DSSCs) are earmarked to offer relatively high efficiency with a comparably low cost compared to traditional semiconductor-based cells. In 2011, Yella *et al* [1.9] produced DSSCs with a 12% efficiency using a cobalt-based redox electrolyte. During operation, the electron that is excited from the dye molecule is injected into a semi-conductor and send via an external load to a back electrode; see schematic in Fig. 1.2 The semi-conductor material has a dual role in the DSSC. Initially, it allows for excited electrons to be injected from the dye molecule and secondly forms a connection to the counter electrode for the electrons gathered from the dye molecule.

## Best Research-Cell Efficiencies

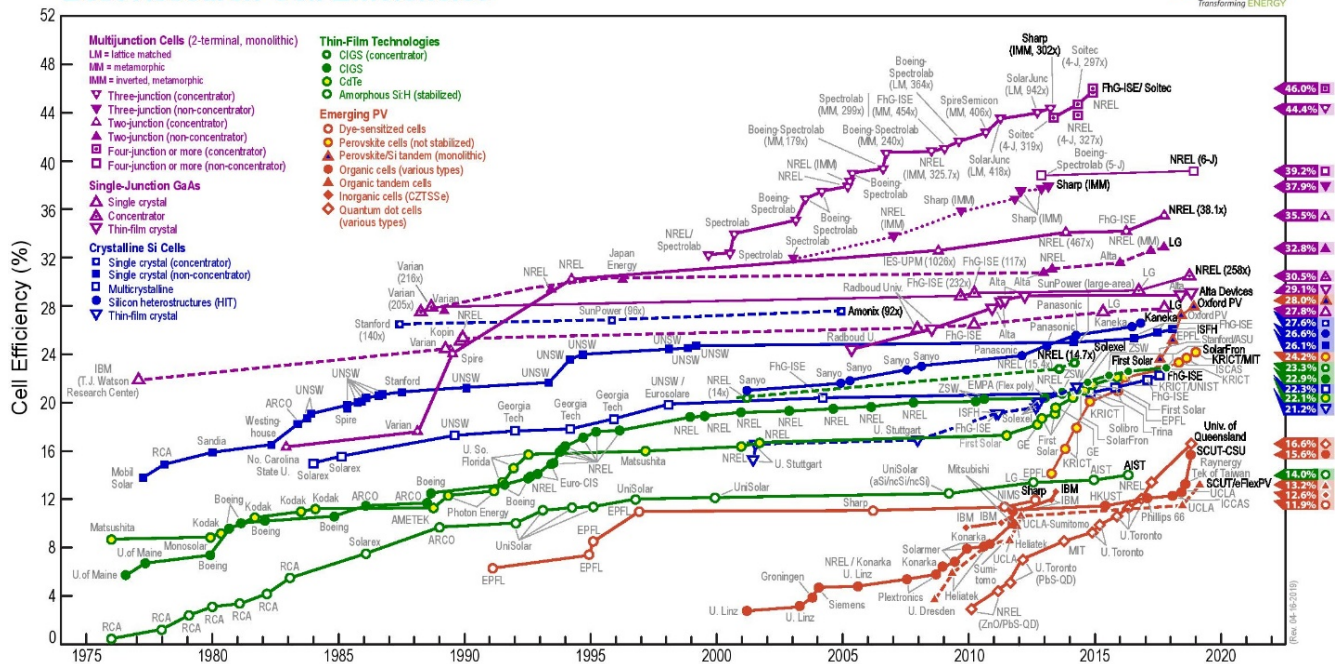


**Fig. 1.1:** Solar cell current efficiencies throughout the years for the different types of solar cells and best research-cell efficiencies. The world record efficiency of a solar cell is 46.0%, which was achieved by a four-junction solar cell [1.8]

### 1.3 TiO<sub>2</sub> Semiconductor

The most prominent semiconductor used is a dense layer of TiO<sub>2</sub> nanoparticles, due to the comparable band alignment of TiO<sub>2</sub> with various ruthenium and cobalt-based dye molecules. This allows for fast electron injection and minimal recombination with holes in the redox electrolyte. In addition, the TiO<sub>2</sub> nanoparticle-based porous film provides a large surface area compared to a continuous thin film of TiO<sub>2</sub>, thereby yielding improved photocurrent generation and ultimately, efficiency [1.10].

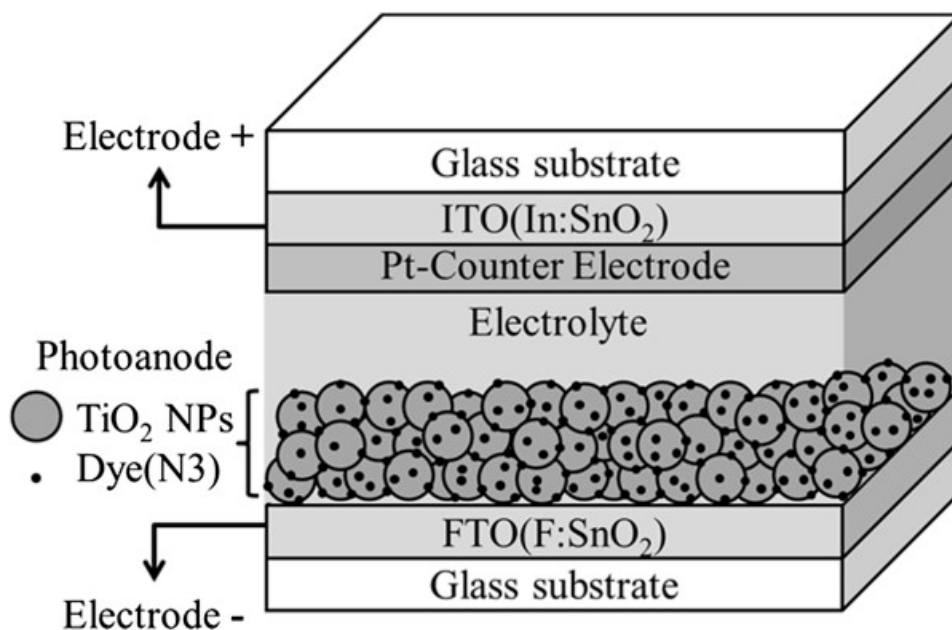


**Fig. 1.2:** Schematic representation of the components of a dye-sensitised solar cell [1.9]

One significant disadvantage of the layer of nanoparticles is charge loss during electron transport between two nanoparticles; known as charge hopping. This causes major shunt resistance during device operation, requiring intense optimisation of the solar cell design. To overcome this tedious process, one approach is to replace the TiO<sub>2</sub> nanoparticles with a layer of one-dimensional nanowires or nanotubes. Studies indicate that TiO<sub>2</sub> nanowires are more suitable, with single-crystal TiO<sub>2</sub> nanowires having notably fewer trapping sites which result in electron recombination and photocurrent loss in photovoltaics [1.11]. To shorten the electron transfer, vertically grown nanowires provide the needed bridge from the top of the nanowires to the substrate [1.12].

Issues involving nanowire materials in the manufacturing of solar cells include high temperature dependent techniques and exposure of environments with extreme levels of pH. All of which have a high likelihood of damaging and in some cases destroying substrates. Resulting in solar cells of poor quality and performance. High temperatures needed for these methods indicate why plastic is not a suitable substrate material for hydrothermal synthesis [1.13].

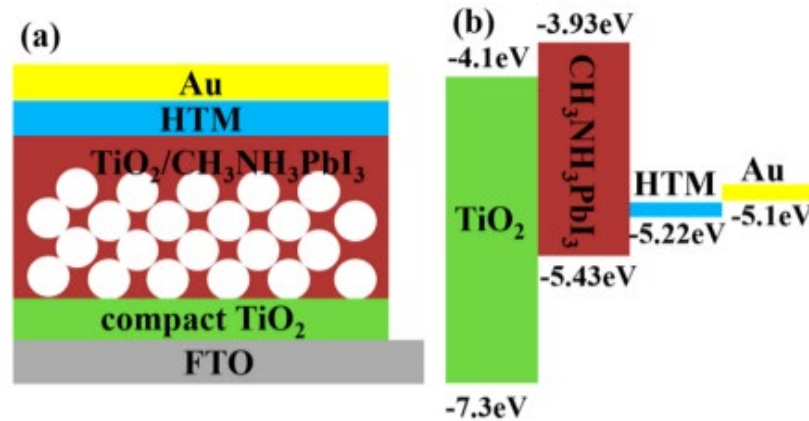


**Fig. 1.3:** (a) The structure and (b) energy level diagram of a perovskite PV cell [1.15]

Noting that different substrates have different surfaces structures and energies, vastly different techniques with careful optimisation are needed for morphological control regarding nano-materials on each substrate [1.14]. In perovskite based solar cells which include a conductive substrate, a compact layer, a perovskite-sensitised TiO<sub>2</sub> porous layer, a hole transporting layer, and a metal electrode. The TiO<sub>2</sub> compact film transports the electron and inhibits recombination[1.15]. Most light will be absorbed by the perovskite film. The matching band structure leads the electron and the hole to separate effectively. To achieve a high efficiency, a TiO<sub>2</sub> porous film with a compatible pore size and thickness should be filled with the perovskite film.

#### 1.4 Aims and Outline

TiO<sub>2</sub> nanostructures doped with non-metals such as nitrogen is a known method to improve the electron transport properties of TiO<sub>2</sub> when used as an ETL in photovoltaics. Most doping approaches make use of the addition of a dopant precursor, typically usually a salt, during the synthesis of the TiO<sub>2</sub> nanostructure. This approach, however, consistently yields uncontrolled doping levels, anion contamination and in general, low quality materials. Thus, a need exists to develop simple, controllable doping approaches. One such approach, which will form the basis of this study, is ex-situ doping using plasma generated nitrogen species in a controlled environment.



This field of study is not widely researched and requires more investigation to understand the doping mechanisms and influence on the optical and electronic properties of the underlying nanomaterial. The inability to have precise control over the deposition parameters during plasma irradiation remains a common drawback for this approach in addition to a lack of understanding of the surface interaction between the nitrogen species and specimen during the experiment.

Based on these knowledge gaps this study will focus on (1) surface etching and (2) formation of the Ti-N bonding network in the TiO<sub>2</sub> lattice upon exposure to a RF generated N<sub>2</sub>/Ar plasma mixture initially, followed by pure N<sub>2</sub> plasma at controlled plasma power, time and substrate temperature conditions. To further improve the ETL properties of the TiO<sub>2</sub> layer, the plasma exposure will be performed on hydrothermally-synthesised TiO<sub>2</sub> nanowire arrays, thereby combining the positive effects of nitrogen doping with the one-dimensional transport properties of the nanowire architecture. As an added incentive, due to the chemical nature of hydrothermal synthesis and the gas nature of the N<sub>2</sub> plasma treatment, the industrialisation of these two techniques for mass production of N-doped TiO<sub>2</sub> nanowires can potentially be scaled effectively. Optimisation of the plasma irradiation conditions will be achieved by studying the effect of the following experimental parameters on the morphologically optimised TiO<sub>2</sub> nanowire arrays:

- Plasma Power (in Watts)
- Exposure Time (in mins)
- Substrate Temperature (in °C)

The outline of this thesis is as follows:

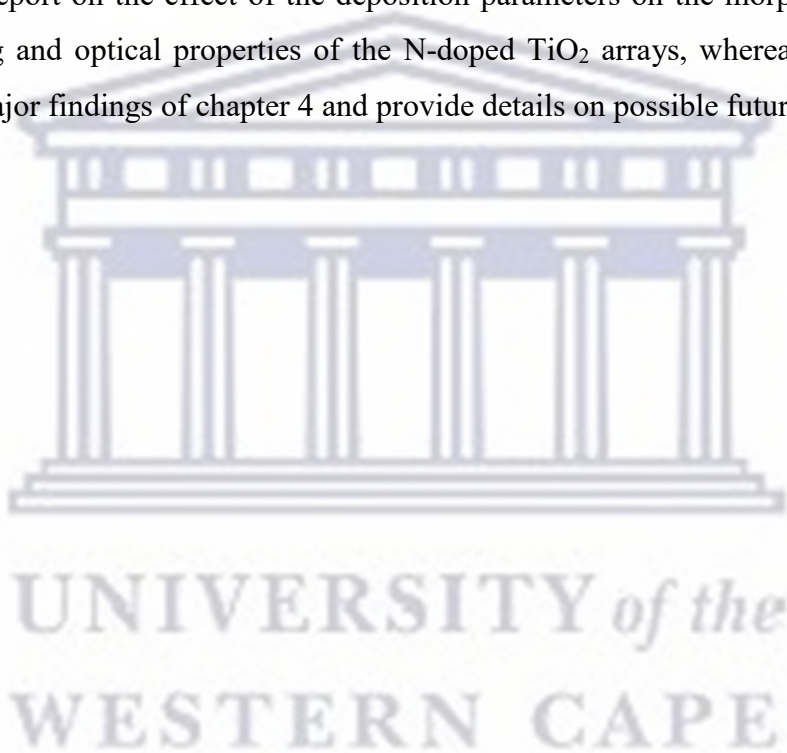
In **Chapter 1**, an introduction into the need and development of photovoltaics were given, with the focus on the role of TiO<sub>2</sub> as a prominent electron carrier material in different photovoltaic types. Topics such as the global energy reliance, generations of photovoltaics and advantages of semiconductors like TiO<sub>2</sub> were discussed.

**Chapter 2** will provide a detailed description of the properties of TiO<sub>2</sub>. The structure, thermodynamic properties, electrical properties, optical properties and role as an electron transport layer will be discussed. Various TiO<sub>2</sub> synthesis methods will also be discussed with specific focus

on nanoparticles/nanowires/nanorod growth. The role of doping TiO<sub>2</sub> will be explained as well as the need for N<sub>2</sub> implantation and its effects.

**Chapter 3** will discuss the experimental methods used in this study, as well as the characterisation techniques used to investigate the structure, morphology, chemical bonding and optical properties of TiO<sub>2</sub> and the effects of N<sub>2</sub> plasma treatment. Furthermore, each section will make specific mention of results supporting the findings of this study.

**Chapter 4** will report on the effect of the deposition parameters on the morphology, structure, chemical bonding and optical properties of the N-doped TiO<sub>2</sub> arrays, whereas **Chapter 5** will summarise the major findings of chapter 4 and provide details on possible future studies.



## References

- [1.1] D. Gielen, F. Boshell, D. Saygin, M. Bazilian, N. Wagner, R. Gorini, “*The role of renewable energy in the global energy transformation*”, *Energy Strat. Rev.* 24 (2019) 38
- [1.2] B. Sovacool, “*Critically weighing the costs and benefits of a nuclear renaissance*”, *J. E. Sci.* 7 (2010) 105
- [1.3] A. Uihlein, D. Magagna, “*Wave and tidal current energy – a review of the current state of research beyond technology*”, *Renew. Sus. Rev.* 58 (2016) 1070
- [1.4] A. Hagfeldt, G. Boschloo, L. Sun, L. Kloo, H. Pettersson, “*Dye-sensitised solar cells*”, *Chem. Rev.* 110 (2010) 6595
- [1.5] N. Lewis, D. Nocera, “*Powering the planet: chemical challenges in solar energy utilisation*”, *P. Natl. Acad. Sci.* 103 (2006) 15729
- [1.6] D. Chapin, C. Fuller, G. Pearson, “*A new silicon p-n junction photocell for converting solar radiation into electrical power*”, *J. Appl. Phys.* 25 (1954) 676
- [1.7] W. Rhodes, T. Asakura, K. Brenner, T. Hänsch, T. Kamiya, F. Krauz, B Konemar H. Weinfurter, “*Photovoltaic solar energy generation*”, *Springer Series in Optical Sciences*, Berlin, 115 (2005) 11-21, 23-41, 85-94
- [1.8] L. Peter, “*Towards sustainable photovoltaics: the search for new materials*”, *Trans. R. S.* 396 (1942) 1840
- [1.9] A. Yella, H. Lee, H. Tsao, C. Yi, A. Chandiran, M. Nazeeruddin, E. Diau, C. Yeh, S. Zakeerhiddin, M. Grätzel, “*Porphyrin-sensitised solar cells with cobalt (II/III)-based redox electrolyte exceed 12 percent efficiency*”, *Sci.* 334 (2011) 629
- [1.10] C. Li, D. Zhang, X. Liu, S. Han, T. Tang, J. Han, C. Zhou, “*In<sub>2</sub>O<sub>3</sub> nanowires as chemical sensors*”, *Appl. Phys. Lett.* 82 (2003) 1613
- [1.11] M. Law, L. Greene, J. Johnson, R. Saykally, P. Yang, “*Nanowire dye-sensitised solar cells*”, *Nat. Mater.* 4 (2005) 455
- [1.12] M. Park, G. Yi, “*Electroluminescence in n-ZnO nanorod arrays vertically grown on p-GaN*”, *Adv. Mater.* 16 (2004) 87
- [1.13] R. McConnell, “*Assessment of the dye-sensitised solar cell*”, *E. Rev.* 6 (2002) 271
- [1.14] A. Hochbaum, R. Fan, R. He, P. Yang, “*Controlled growth of Si nanowire arrays for device integration*”, *Nano. Lett.* 5 (2005) 457

[1.15] W. Ke, G. Fang, J. Wang, P. Qin, H. Tao, H. Lei, Q. Liu, X. Dai, X. Zhou, “*Perovskite solar cell with an efficient TiO<sub>2</sub> compact film*”, ACS Appl. Mat. Int. 6 (2014) 15959





## CHAPTER 2: Literature Review of TiO<sub>2</sub>

---

TiO<sub>2</sub> plays the role of being the frontrunner in the photo-catalyst market. With plans that include, degrading organic pollutants, photo-water splitting, reverse osmosis and high efficiency DSSCs [2.1]. Research into the properties of TiO<sub>2</sub> have been catalogued over the last 100 years [2.2]. In tandem with the development of nanophysics and nanoscience, particularly interesting properties of TiO<sub>2</sub> were uncovered with the manipulation of grain size to nanometres [2.3].

### 2.1 Structure of TiO<sub>2</sub>

The most common phases of TiO<sub>2</sub> are rutile, anatase and brookite. Two other phases which are uncommon are an orthorhombic  $\alpha$ -PbO<sub>2</sub> form and a monoclinic baddeleyite form. Which were discovered only in extreme pressure conditions [2.4]. Rutile TiO<sub>2</sub> is found to be at equilibrium at all temperatures. While anatase and brookite TiO<sub>2</sub> nanoparticles are observed to phase change to rutile after annealing at high temperature [2.5]. Due to the stability of the rutile phase as well as the high activity of the anatase phase, continued research has been dedicated and usage of these two phases of TiO<sub>2</sub> has increased [2.6]. The rutile and the anatase phase both have a tetragonal crystal structure. In TiO<sub>2</sub>, the crystal structure can be described by chains of TiO<sub>6</sub> octahedra as shown in Fig. 2.1. [2.7]. The composition of octahedra chains in anatase and rutile phases of TiO<sub>2</sub> have variations of distortions and assembly patterns of the chains. For the rutile phase, Ti<sup>4+</sup> is at the centre of a distorted octahedron with six O<sup>2-</sup> ions around [2.8]. For each of the octahedron, there are ten neighbouring octahedral, which in turn share the associate edges with two neighbours and corners with the other eight neighbours [2.8]. The bond angles for the Ti-O rutile two nearest O<sup>2-</sup> ions are 90° and 81.21°, respectively. In the rutile phase the lengths of the Ti-O bonds are 1.949 Å and 1.980 Å. With lattice constants of rutile: a = 4.5937 Å and c = 2.9587 Å.

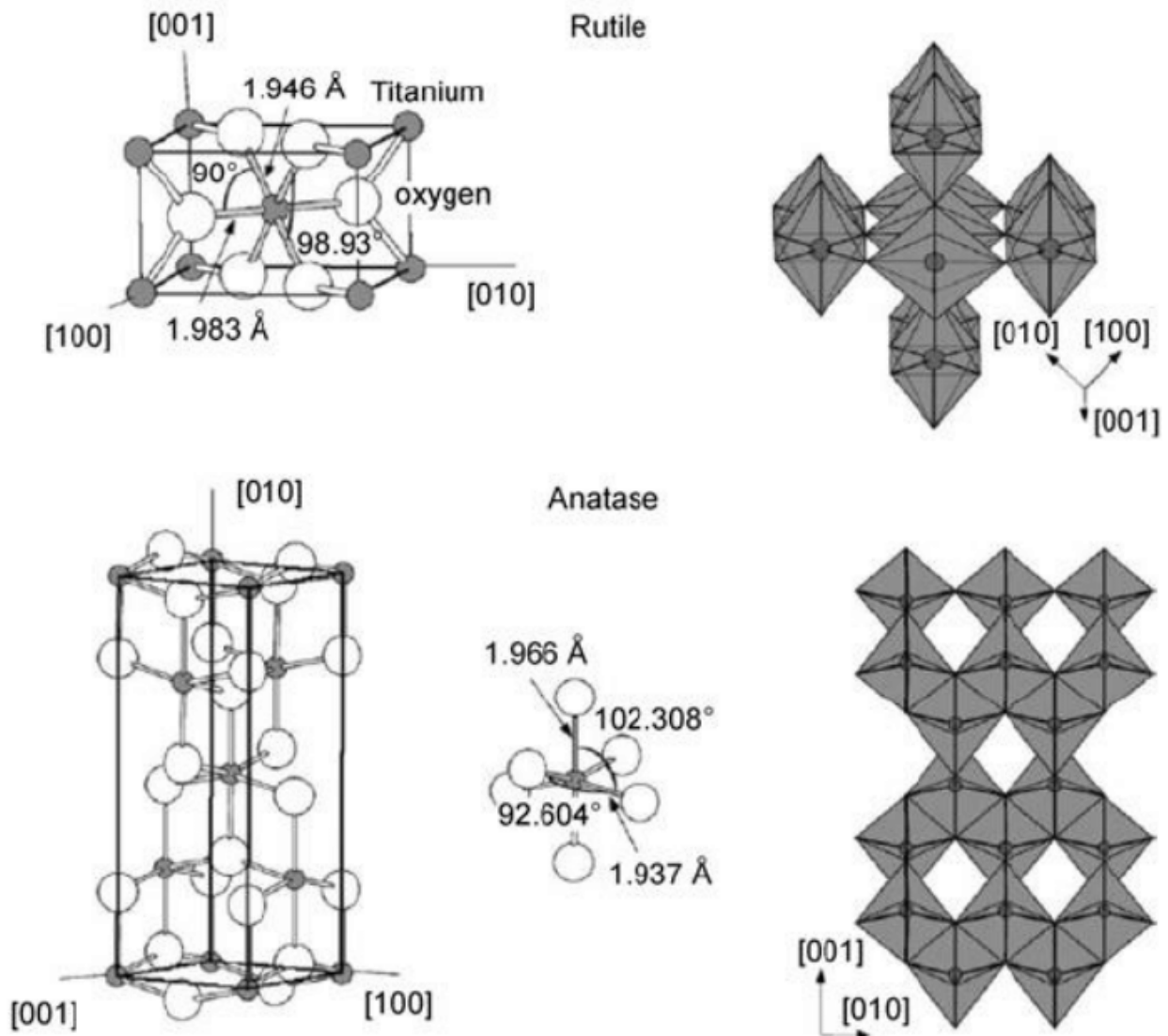


**Fig. 2.1:** (left) Tetragonal rutile and anatase  $\text{TiO}_2$  structure. (right) Assembly bulk stacked patterns of rutile and anatase  $\text{TiO}_2$  [2.8]

The anatase phase is comprised of the same  $\text{TiO}_2$  octahedra chains, which is shown in Fig. 2.1. Compared to the rutile structure, the octahedra in the anatase structure have greater distortions in their bonds. The bond angles for the two Ti-O bonds are found to be  $78.12^\circ$  and  $92.41^\circ$ . For anatase, there are eight surrounding octahedra for each octahedron. With four octahedra sharing edges and the remaining four octahedra sharing corners. There are comparatively shorter Ti-O bonds for anatase than for rutile. Lengths include,  $1.934 \text{ \AA}$  and  $1.980 \text{ \AA}$ .  $a$  and  $c$ , the lattice constants for anatase are  $3.79 \text{ \AA}$  and  $9.510 \text{ \AA}$  respectively. For rutile  $\text{TiO}_2$  the tetragonal structure with  $a = 4.95 \text{ \AA}$  and  $2.96 \text{ \AA}$ . The surface families with the lowest energy and therefore the

thermodynamically equilibrium morphology of rutile TiO<sub>2</sub> is a trunked octahedron. The differences in the lattice constants for rutile and anatase result in the differing mass densities, which are 4.25 g/cm<sup>3</sup> and 3.89 g/cm<sup>3</sup> respectfully [2.9].

## 2.2 Thermodynamic Properties

The most stable phase of TiO<sub>2</sub> is rutile. At every temperature the rutile (110) surface is thermodynamically the surface with most stability in the structure [2.10]. Reconstructed rutile surfaces can be achieved after high temperature annealing, resulting in the lowest energy. The nanocrystals have transformations among the known three phases of TiO<sub>2</sub> have been thoroughly researched. There have been extensive studies conducted by Czanderna *et al* [2.5] for anatase to rutile transformation under differing annealing conditions. This research indicated that there was no anatase to rutile phase transformation occurring below 610 °C. Further annealing at 730 °C and above induced rapid phase change for anatase. It was observed by Zhang [2.11] that anatase and brookite nanocrystals transformed to rutile during synthesis process for a certain size of the nanocrystals. Li *et al* [2.12] found that there was evidence in small anatase nanoparticles aggregating to form larger rutile nanoparticles. When observed to reach a certain size during the synthesis process. Larger rutile particles interacting with the surrounding anatase nanoparticles to conglomerate into larger rutile particles.

It was reported by Ye *et al* [2.13] that slow transformation from brookite to anatase occurred below 1053 K and both brookite-anatase phase transformation and anatase-rutile phase transformations were found to occur quickly between 1053 K and 1123 K. As the temperature reaches above 1123 K, grain growth of the rutile is only observed resulting in rutile becoming the dominant phase for TiO<sub>2</sub>. Understanding the phase stability requires the Gibbs free energy ( $\Delta G$ ) first has to be defined.

Gibbs free energy is then:

$$\Delta G = \Delta H - T\Delta S \quad (2.1)$$

Where T can be defined as the absolute temperature in kelvin,  $\Delta H$  is the enthalpy and  $\Delta S$  is the entropy. Mitsuhashi *et al* [2.14] experiments showed that both anatase and rutile have the same

$\Delta S$ . Resulting in the phase stability being solely determined by the enthalpy of the different phases of  $\text{TiO}_2$ . Banfield and Zhang [2.15] together calculated the various enthalpies of: anatase, rutile and brookite nanocrystals through modelling. With the use of atomistic simulation, the experiments showed that anatase had the lowest enthalpy, while rutile had the highest enthalpy for the nanocrystals. Fig. 2.2 shows the estimated enthalpies of the three most common phases of  $\text{TiO}_2$  at various particle sizes [2.16]. As observed in the Fig. 2.2, the most stable phase is estimated to be anatase in the region of high surface area, which corresponds to the particle size between 10-20 nm in diameter. The trend shows that decreasing surface area results in the increase of particle size. At this surface area, rutile and brookite are the more stable phase. The trend indicates that equally sized nanoparticles for anatase, rutile and brookite are thermodynamically stable for  $\text{TiO}_2$  nanocrystal dimensions diameter: smaller than 11 nm, greater than 35 nm and between 11 nm and 35 nm respectfully.

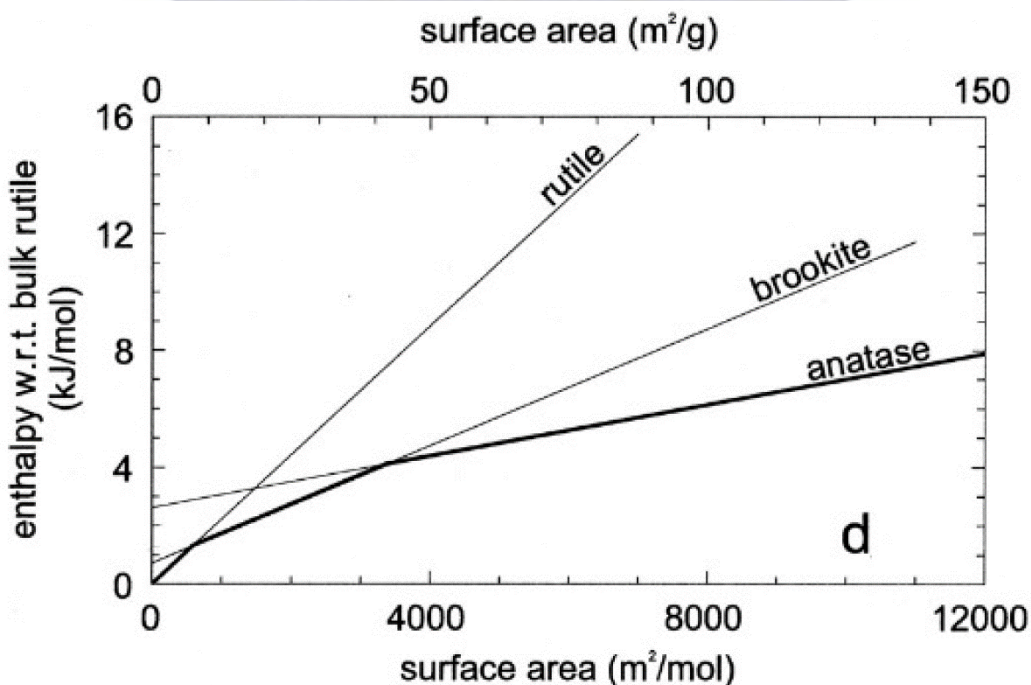


**Fig. 2.2:** Enthalpies of the different phases of  $\text{TiO}_2$  [2.16]

Apart from the results above, there has been some conflicting results for anatase structure. However, for the anatase structure to hold at minimum one dimension needs to be less than 35 nm [2.17]. When HF acid is added for synthesis of anatase particles over 1 micron, due to fluorine

ions being absorbed by the surface of TiO<sub>2</sub> particles and the energy change of the anatase surfaces [2.18]. It was reported by Feng *et al* [2.19] for rutile nanowires of 20nm were synthesized via the hydrothermal method.

## 2.3 Electronic Properties of Rutile TiO<sub>2</sub>

### 2.3.1 Band Structure:

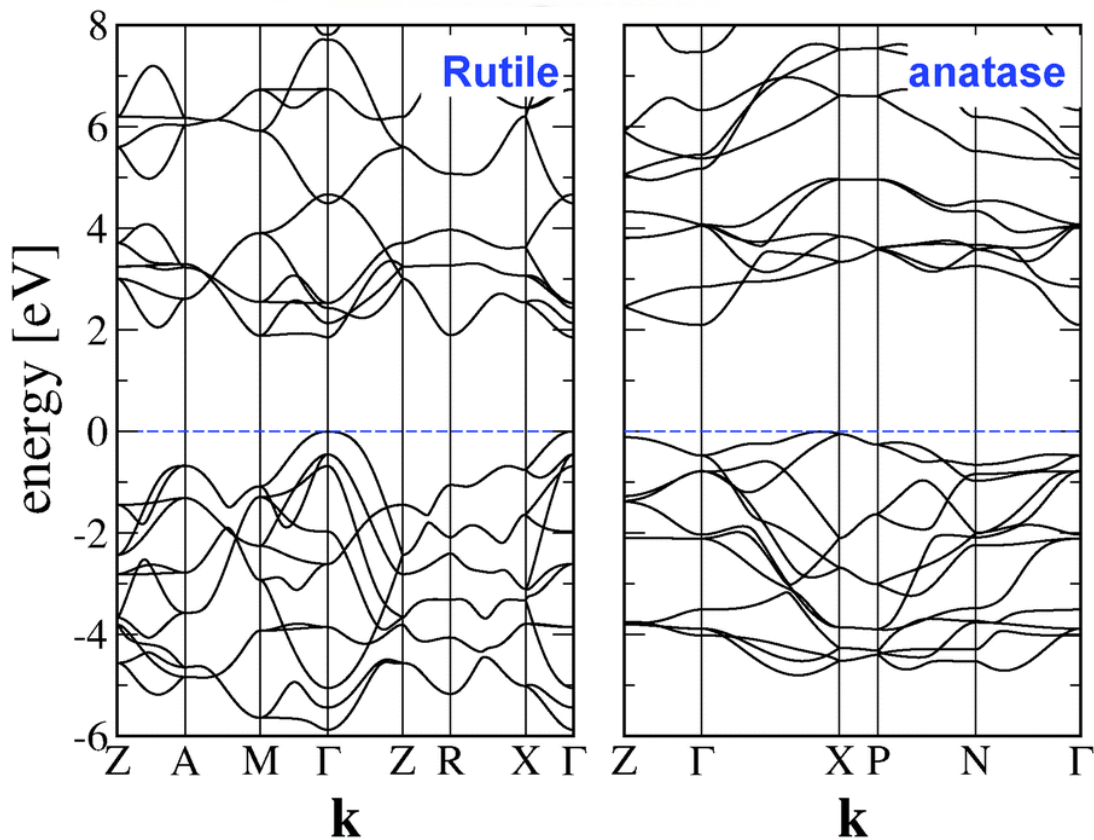


**Fig. 2.3:** Electronic band structure of TiO<sub>2</sub> along high symmetry directions. With the top valence band taken as the zero of energy [2.20]

The TiO<sub>2</sub> electrical structure has been studied at length [2.21]. Experimentation through various characterisation methods: (i) resonant photoelectron spectroscopy (R-UPS) [2.22], (ii) electron-energy-loss spectroscopy (EELS), (iii) ultraviolet photoelectron spectroscopy (UPS) [2.23], (iv)



Auger-electron spectroscopy [2.22], (v) x-ray emission (XES) and absorption spectroscopy (XAS) [2.24], (vi) x-ray-induced Auger-electron spectroscopy and (vii) x-ray photoemission spectroscopy (XPS) [2.21]. Recent calculations probing the near-edge structure at core-level spectroscopies use the linear muffin-tin orbital (LMTO) method [2.25]. Using theoretical equilibrium values for the lattice constants  $a$ ,  $c$  and  $u$ , the electronic structure can be calculated [2.24]. In Fig. 2.3 the band structure of rutile  $\text{TiO}_2$  indicates high symmetry alongside the direction of the Brillouin Zone (BZ). Vos *et al* [2.26] found similar comparable results with empirical tight binding. With the predicted band gap at a transition  $\Gamma$  at 2 eV, it is significantly lower than the experimental value of 3eV. Which is commonplace for insulators and semiconductors when in direct comparison to the experimental values [2.37]. A bandwidth of 1.8 eV is a direct result of low dispersion from O 2s bands showed in the lowest panel of Fig. 2.4 [2.37]. 17 eV is the valence band maximum and the O 2s separation. Auger spectroscopy [2.28] and photoelectron spectroscopy [2.29] confirm the separation is between the values of 16 eV and 18 eV. The upper valence bands have a bandwidth of 5.7 eV, with constituents of O 2p states hybridised with Ti 3d states. Which corresponds to the experimental value of 5-6 eV. The conduction band may be further divided into two groups with Ti-d states. The upper group conduction bandwidth 3 eV, with an average energy of 6 eV. The lower group conduction bandwidth of 2.9 eV, with an average energy of 3.5 eV. At 4.6 eV an overlap occurs between the upper and lower groups of the conduction band. [2.27] Optical reflectivity studies and molecular orbital studies of Fischer *et al* [2.29] found the separation between the upper and lower groups to be 2.1 eV, which compares to the theoretical value of 2 eV Transition metal oxides that have similar conduction band separation are  $\text{NbO}_2$ ,  $\text{RuO}_2$ , and  $\text{IrO}_2$  from linear muffin-tin orbital (LMTO) calculations [2.27].

### 2.3.2 Density of States:

The density of states (DOS) for the rutile structure of  $\text{TiO}_2$  is shown in Fig. 2.4. DOS is needed to evaluate integrals over constant energy surfaces by using the linear analytic tetrahedron method. Experimentally the valence band spectra are determined through measurements of XPS, XES and UPS [2.30]. The  $\text{TiO}_2$  (110) surface valence band density of states is observable on Fig 2.4 [2.21], at photon energy 46 eV. Self-consistent features have been found through XPS [2.34] and UPS

[2.21], with notable splitting between two major peaks ranging from 1.7 to 2.0 eV. Both theoretical and experimental results agree on the separation of peaks to be 2.4 eV.

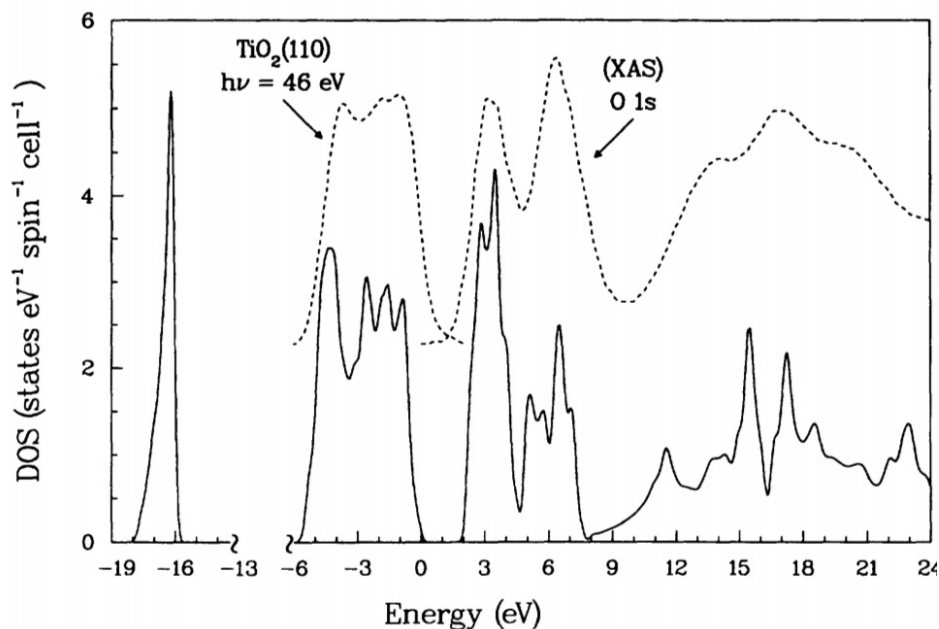


**Fig. 2.4:** Density of states for  $\text{TiO}_2$  in states/eV/spin/unit cell compared to experimental UPS for the  $\text{TiO}_2$  (110) surface at a photon energy of 46 eV and the  $\text{TiO}_2$  XAS spectra of the O 1s edge

Noting that the major features of the valence band have been found to negligible to surface effects. Which is supported in theory that show tight-binding calculations in which discrepancies between the bulk and the surface DOS were found to be insignificant. Recent XAS [2.24] measurements probe the unoccupied conduction band states in transition metal oxides. From Fig. 2.4, the O 1s XAS spectra can be approximated as the oxygen p-projected density of states in the conduction band. The initial peaks result from the crystal-field splitting of the Ti 3d wave functions into states with  $t_{2g}$  and  $e_g$  symmetries. With these states representing the  $\pi$  and  $\sigma$  Ti d orbitals being hybridised with O 2p states and the  $\sigma$ -e orbitals being in higher energy. The Ti 4sp character is prominently found in the DOS between 9 eV and 24 eV. Using EELS [2.24] and XAS similar results have been observed, representing the conduction band Ti 3d character.

### 2.3.3 *Electron Density:*

There is a resulting covalent character arising from the inclusion of d-orbitals in the electronic properties of transition metal oxides. Characterising this manner of covalent bonding in  $\text{TiO}_2$  is done through deformation electron density using the independent atom model. The model in question defines the difference between the total valence electron density and linear superposition of radically symmetric atomic charge densities. In the positive deformation regions, charge build-up occurs and forms so called bonding electrons, while the negative deformation regions form so called antibonding states. The degree of ionic bonding is due to the relative displacement of the maximum towards the more electronegative atom. A proposition by Pauling states that edge-shared polyhedral decrease the stability of an ionic crystal. It is therefore expected that a large degree of covalent character between the Ti-O bonds be present in order to compensate for a reduced stability accompanying the shared edges of the oxygen octahedral. Positive charge deformation along the perpendicular to the Ti-O bonds is then the resultant [2.27].

Fig. 2.5 (a), (b) shows contour plots of the valence deformation maps for (110) and (110) planes of the tetragonal unit cell. The solid and dashed contours indicate the positive and negative deformation densities. The (110) plane has two apical bonds, the (110) plane has four equatorial bonds. Three-fold coordinated oxygen atoms can be identified for the (110) plane with site symmetry  $C_2$ . The  $D_2$  and site symmetry of the Ti atom is observed from the distortion of the lobes of considerable degree of covalent character present in the Ti-O bonds. Due to electronegativity differences between Ti and O, there is a 40% decrease in the covalent character for the Ti-O bond.



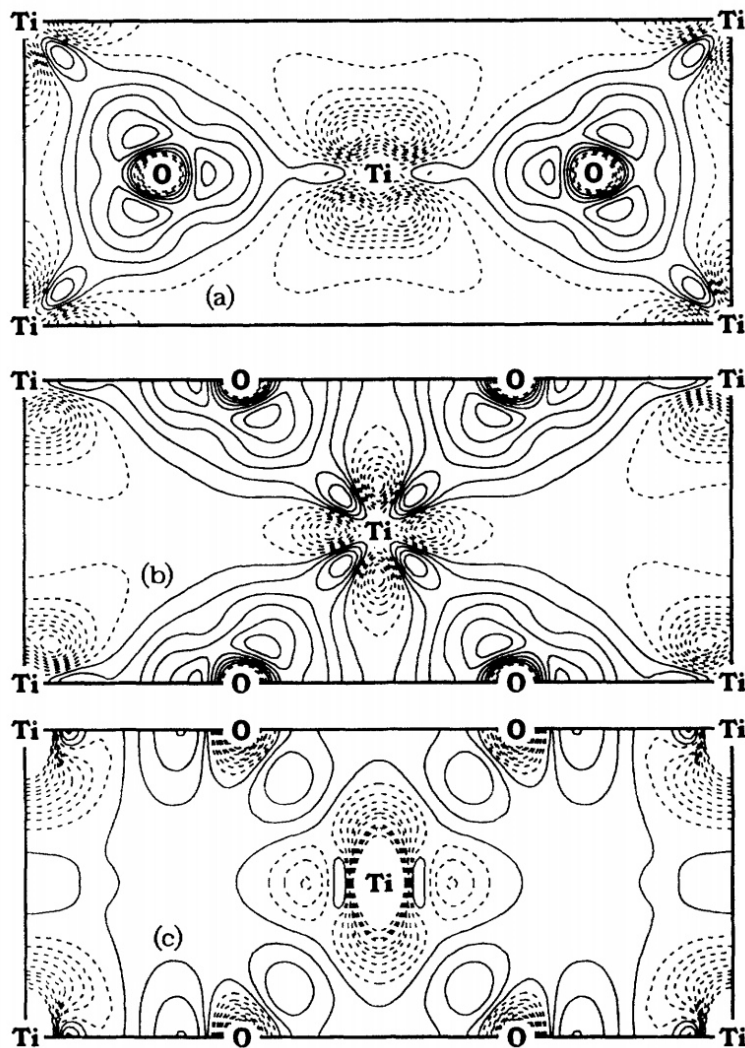


**Fig. 2.5:** Pseudo-atom valence density difference maps for the (a) (110) and (b) (110) lattice planes. Contours of constant charge density are separated by  $3e/V_0$ . In (c) it is seen that the experimental electron density map in the (110) plane [2.27]

The covalency is a direct result of the hybridisation between the O 2p and Ti 3d wave functions. A significant amount of Ti 3d character is in the O 2p valence band, which indicates the participation of the Ti 3d character in bonding. Resonant photoemission studies whereby photon energy is swept through the optical transition energy from Ti 3p~3d have shown evidence for participation of the Ti 3d character bonding. Figure 2.6 (c) the experimental electron-deformation maps for the (110) plane can be observed. The major features show a significant degree of covalent

character for the Ti-O bonds and the charge depletion regions near the Ti sites, elongating along the [001] direction to the nearest neighbour Ti atoms [2.27].

Fig. 2.6 (a) and (b) display the  $e_g$  and  $t_{2g}$  conduction band complexes, with Fig. 2.6 (c) shows the upper valence band states of mostly O2p character creating charge density. At 0 atoms in the conduction band states and at the Ti charge in the valence band there is a prominent feature of the figures, observing a significant amount of charge. The lower energy  $t_{2z}$  derived anti-bonding m-like bands and the higher energy anti-bonding e-derived bands with are Ti-O  $\sigma$  bonding are visible in the aforementioned figures [2.27].

#### 2.4 Optical Properties of Rutile TiO<sub>2</sub>

Reflectance [2.31], electro-reflectance [2.32], absorption [2.33], electro-absorption [2.34] and wavelength modulated transmission [2.35], spectroscopies have determined the optical properties of TiO<sub>2</sub>. Spectral features particular to the electronic excitations within the BZ are dependent upon accurate electronic structure calculations. The resulting HKS eigenvalues and eigenvectors commonly related to single particle excitation energies and their wave-functions. A many body nature of the electron-electron interaction is needed to surpass the single-particle description. Formalism for many body effects is successful in simpler insulators and semiconductors with near perfect wave-functions to that obtained with the local density approximation (LDA) [2.36]. The LDA has difficulty modelling transition metal oxides, as the LDA models NiO as metal, despite NiO being an insulator [2.37]. The dielectric function is defined as the response function for the optical properties of a solid describing of the absorption or emission of electrons and photons. The dielectric function is calculated from accurate band structure leading to the assignment of spectral features in particular excited regions in the BZ.

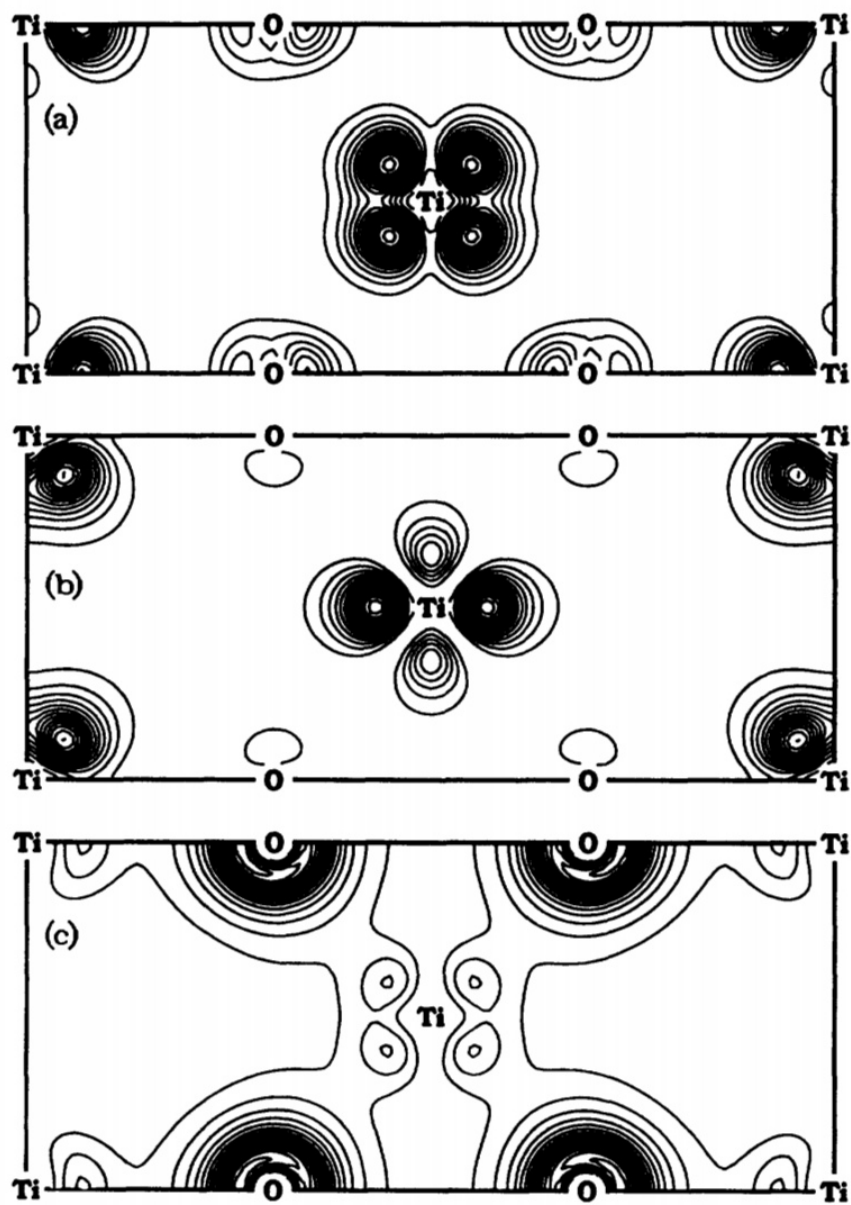


**Fig. 2.6:** Pseudo-charge-density contour plot of the (a)  $e_g$ , (b)  $t_{2g}$  and (c) upper O2p valence bands in the (110) lattice plane. Contours of constant charge density are separated by  $10e/V_p$

This method is difficult for materials with complex structures as well as insulators. Using the frequency-dependent dielectric function:

$$\epsilon(\omega) = \epsilon_1(\omega) + i\epsilon_2(\omega) \quad (2.2)$$

Is evaluated using the Ehrenreich and Cohen formalism [2.38]. The imaginary part of the dielectric function is then:

$$\epsilon_2(\omega) = \frac{4\pi^2 e^2 \hbar}{m^2 \omega^2} \sum_{v,c} \frac{2}{(2\pi)^3} \int_{BZ} \delta(\omega_{cv}(\mathbf{k}) - \omega) \times |\mathbf{M}_{cv}(\mathbf{k})|^2 d^3k \quad (2.3)$$

Where the integral that is over the first BZ,  $\mathbf{M}_{cv}(\mathbf{k}) = \langle \mathbf{u}_{c\mathbf{k}} | \hat{\mathbf{e}} \cdot \nabla | \mathbf{u}_{v\mathbf{k}} \rangle$  are the dipole matrix elements of the direct transitions between valence and conduction band states,  $\hbar\omega_{cv}(\mathbf{k}) = E_{c\mathbf{k}} - E_{v\mathbf{k}}$  is the excitation energy  $\hat{\mathbf{e}}$  is the polarisation vector of the electric field, and  $\mathbf{u}_{c\mathbf{k}}(\mathbf{r})$  is the periodic part of the Bloch wave function for a conduction band state with vector  $\mathbf{k}$ . Due to the large anisotropic nature of the tetragonal cell of rutile, the optical properties are strongly dependent on the incoming direction of the polarised light. A perpendicular polarisation direction or parallel to the c-axis results in a high degree of fine structure in the optical properties [2.31]. Fig. 2.7 (a) and 2.7 (b) show the imaginary part of the dielectric function for both the perpendicular and parallel incident light. Cardona *et al* [2.31] performed the experiment.

Experimental reflectivity [2.31] and electro-reflectance [2.32] experimentation show the significant features  $A_1$  and  $A_2$  in Fig 2.7 (a) have been a direct consequence of the splitting in the O  $2p_{xy}$  orbitals [2.39].  $A_1$  occurs at the first major peak at 3.06 eV and is the result of transitions between the top of the valence band to the bottom of the conduction band. The following major peak  $A_2$  occurs at 4.67 eV and is the direct result from the transition between the top four valence bands and the  $t_{2g}$  conduction band states corresponding to the first six conduction bands. There are two additional features located between the two peaks [2.31]. Further features and higher energy structures are seen in Table 2.1.

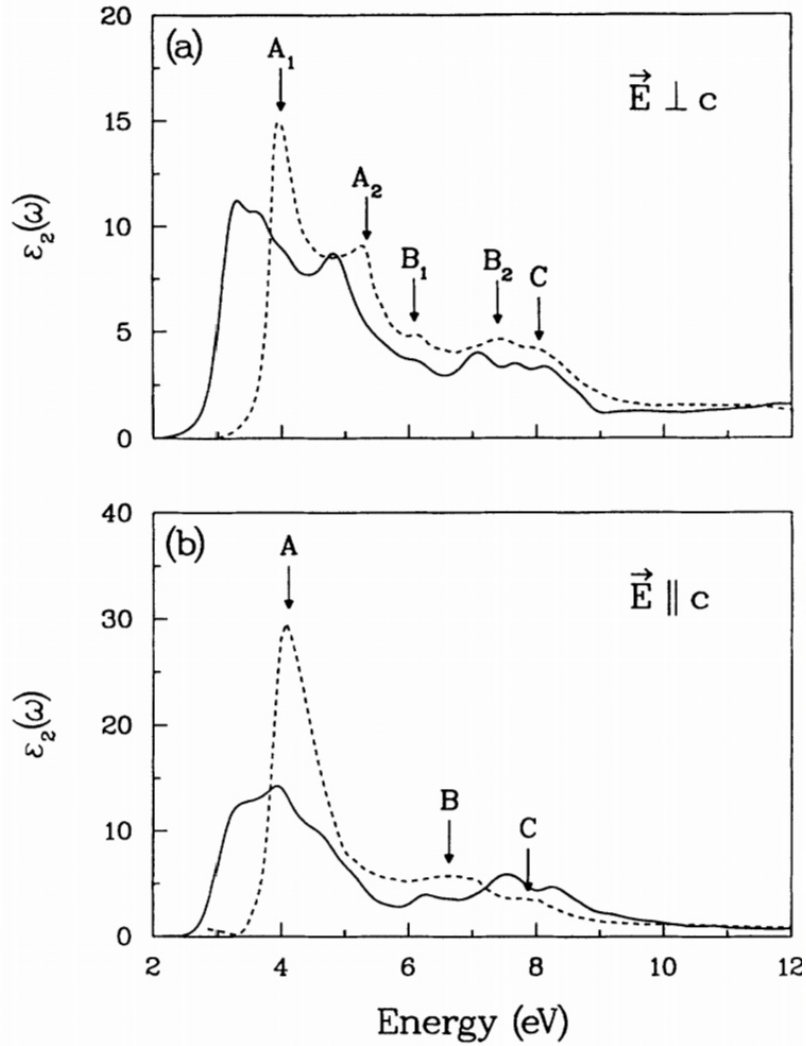


**Fig. 2.7:** Imaginary part of the dielectric function for polarisation vector (a) perpendicular and (b) parallel to the c-axis. Present results (solid line) are compared to the experimental room-temperature results of Cardona *et al* [2.31]



**Table 2.1:** Experimental structure in the imaginary part of the dielectric function of Cardona *et al* [2.31] compared to the present first-principles results for polarisations perpendicular and parallel to the c-axis.

$E_1$	Experiment	Theory	$E_g$	Experiment	Theory
$A_1$	4.00	3.06	$A$	4.11	3.06
$A_2$	5.35	4.67			
$B_1$	6.10	6.06	$B$	6.63	6.15
$B_2$	7.40	6.96			
$C$	8.05	7.59	$C$	7.87	7.27

Absorption experiments [2.39] reveal exciton behaviour for the direct-forbidden transition. Peak contribution is not as a result of excitonic behaviour, rather primarily due to inter-band transitions. From Cardona *et al* [2.31] the real part of the equation results in the perpendicular polarisation direction dielectric constant to be 7.07 and the parallel polarisation constant to be 5.80 respectively.

## 2.5 Methods for Synthesis of Rutile TiO<sub>2</sub>

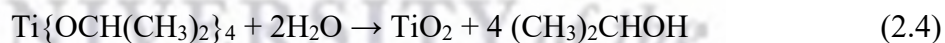
### 2.5.1 Physical Vapour Deposition (PVD)

There are a number of methods to synthesise rutile TiO<sub>2</sub>. A typical physical vapour deposition system consists of the following. A three-zone tube furnace that separates the metal source and the growth substrate. Allowing for nanostructures to be grown on different substrates. The metal source placed in the high temperature zone to produce a metal vapour. From one end of the quartz tube through a carrier gas an oxidant agent is introduced and the growth substrate is placed in the second low temperature zone in the reaction tube. At the high temperature zone, the metal source is evaporated and then brought to the low temperature zone by the carrier gas along with the oxidant. Metal oxide or metal particles are then used as a growth catalyst. Deposition on the catalyst is from metal oxide droplets that solidify around the catalyst. A dense nanowire array can

be grown on the substrate at low temperature using this method [2.40]. Some specific substrates including FTO glass provides some difficulties with growing nanowires, due to the substrates having to match the crystal structure of the metal oxide and also survive high temperature annealing.

### 2.5.2 Chemical Vapour Deposition (CVD)

CVD has similarities to physical vapour deposition (PVD), the difference is how the metal source in the CVD process is brought into the reaction vessel by the carrier gas to meet the oxidant at a high temperature zone. Metal evaporation is not needed in this method, allowing for a significantly lower heating temperature compared to the PVD method. Allowing for a broader variety of substrate materials of recommended durability. During synthesis, metal and oxygen solutions are transferred into a high tube furnace. Melting-point depression theory defines that when the smaller the particle size, the lower the melting point [2.35]. The reaction generates droplets on the surface of substrate from the product. An alloy is formed from the small droplets of metal oxide from the reaction. A common titania source for CVD is the chemical titanium iso-prop oxide (TTIP), with the formula  $\text{Ti}\{\text{OCH}(\text{CH}_3)_2\}_4$ . TTIP is highly reactive with water and deposits  $\text{TiO}_2$  according to the reaction:



Wu *et al* [2.41] reported successfully reported well-aligned rutile and anatase  $\text{TiO}_2$  nano-rods using the MOCVD method. In their experiment, TTIP was heated to 60 °C to increase the concentration of titanium in the vapor and two flows of hot nitrogen gas passed through TTIP and water separately. Anatase nano-rods were then synthesized at 560°C and rutile nano-rods were synthesised at 650°C.

### 2.5.3 Electrochemical Anodisation

Titania nanotube arrays were synthesised by anodising Ti foil in a fluorine-based electrolyte by Paulose *et al* [2.42]. Electrochemical anodisation focused on the precision of control of the morphological structure of the nanotube array, such as wall thickness, pore size and length. Anodisation of titania nanotubes occurs in a two-electrode electrochemical cell. A platinum foil is used as a cathode at a constant potential. Ti foil may be anodised at various potential voltages. Depending on the experiment, a low applied voltage between 3-5 V results in a porous layer on the surface of the Ti foil. For voltages above 10 V, tube-like structures are produced on the Ti foil. Control of TiO<sub>2</sub> nanotube morphology can be controlled by adjusting the synthesis temperature, electrolyte composition and the applied voltages [2.43]. Initially amorphous, the anodised nanotubes are crystallized by high temperature annealing.

### 2.5.4 Hydrothermal Method

The hydrothermal method revolves around a high-pressure solution crystallising at high temperature. Commonly used in many studies to grow TiO<sub>2</sub> nanowires and nanoparticles. The advantage of this method is the uniform nature of synthesising single crystal nanostructures at scale. The synthesis is conducted via wet chemical solution in a sealed metal vessel known as an autoclave. The solution is placed within a Teflon-liner<sup>©</sup> inside the autoclave to prevent corrosion and cross contamination. As the temperature inside the autoclave exceeds the boiling temperature, the internal pressure increases, increasing the boiling temperature as well. Precipitation of a saturated solution occurs on the substrate in the solution. Single crystals can be synthesised using this method without extreme temperatures. Controlled morphology is of keen interest in the majority of research into the hydrothermal method.

Liu *et al* [2.44] successfully grew TiO<sub>2</sub> nanowires on a Ti substrate using an alkali hydrothermal method. Using this method, single crystalline sodium titanate (Na<sub>2</sub>Ti<sub>2</sub>O<sub>5</sub>H<sub>2</sub>O) nanowires are first synthesised on Ti foil. Concluding an ion-exchange process, H<sub>2</sub>Ti<sub>2</sub>O<sub>5</sub>H<sub>2</sub>O nanowires are produced from Na<sub>2</sub>Ti<sub>2</sub>O<sub>5</sub>H<sub>2</sub>O nanowires without morphology changing. Through annealing nanowires at various temperatures, aligned single crystalline anatase and rutile nanowires are grown on a metal

substrate. Different parameters for growth were experimented including, growth time, temperature, concentration of chloride ion and substrate [2.45].

## 2.6 Growth Models of TiO<sub>2</sub>

Nanostructures have many grow patterns. Commonly, introduction of a constituent species in the gas phase is used. The reaction of the gaseous species with a solid, with the second constituent species in a vapour form or then condenses on a surface to deposit a nanostructure. Assisted growth in the vapour phase is routinely used for the production of nanoparticles and nanowires on a substrate. The constituents of the vapour phase can be a metal as is the case of the vapour-solid (VS) and vapour-liquid-solid (VLS). The other option being an oxygen bearing gas as with growth by oxidation.

There are two methods predominately used to generate vapourised metal. The straightforward method uses the substrate as the source of the vapour phase. Which then requires a high temperature producing enough pressure of the material. On preferential sites on the substrate, the vapour phase condenses for growth to occur. The other method is to use a metal source upstream from the substrate to produce the required vapour phase. High temperature is also needed for downstream condensation. Vapour-liquid-solid and vapor solid are known growth models for TiO<sub>2</sub> nanowires [2.46].

### 2.6.1 Vapour-Liquid-Solid Growth Model (VLS)

Limiting the surface locations to produce 1D nanostructures while the vapourised constituents deposit on the confined surface substrates remains an issue. Through a liquid metal catalyst, successful confinement is possible. The VLS mechanism provides confinement where preferential deposition is performed by a catalyst at sites for the vapourised material and give chemical adsorption confinement necessary for 1D growth. Eutectic reactions between a source material and catalyst form liquid droplets. The source material is absorbed into the droplet diffuses to the liquid solid interface of the substrate only after exceeding the solubility limit. 1D grown nanostructures

then spring forth from created nucleation sites. Confinement occurs in the liquid droplet through the enhancement of diffusion and adsorption of the vapour species at the catalyst site [2.46]. A higher reaction rate occurs for the nanostructure forming constituents at the liquid droplet than that of the surrounding are effectively confining the resulting growth to one dimension. An identifying feature for this growth model is the presence of a cap on the tip of the nanostructures produced when the liquid catalyst solidifies during the cooling process.

With an Au cap present, being a strong indicator of the VLS process clearly visible at the tip of the nanowire. It is hypothesised that the Au cap allows for preferential adsorption of O which combines with Ti diffused from the thin film to form a single crystal TiO<sub>2</sub>. Heat treatment was found to have a direct impact on the length of the nanowires while flow rate of the inert gas had no effect [2.46].

### 2.6.2 Vapour-Solid Growth Model (VS)

A key difference between VLS and VS is a metal catalyst not needed to provide confinement for 1D growth from a condensed vapour phase. Explanation of the 1D growth of nanostructures when no catalyst is used is the VS mechanism, with no metal cap after the growth process. Defects on the surface of the substrate provide all the needed confinement needed for 1D growth. Impurity driven, strain induced and dislocation dependent can be the defects needed. Screw dislocations intersecting the surface provides high diffusivity sites compared to that of the non-dislocation containing interface. Sites containing increased diffusivity allow for preferential attachment of the nanostructure constituents in the vapour phase. The nanostructure grows in 1D as more of the gas molecules bond to these sites [2.46].

VS mechanism describes nearly all nanowire growth in which the metal constituent of the metal oxide structure exists in the vapour phase, without a liquid phase present. Research showed a two-step process of thermal evaporation for the growth of TiO<sub>2</sub> nanowires through the VS mechanism. Using a radio frequency heater for significant Ti vapour pressure to condense downstream inducing 1D nanostructures to form. The first step included high surface energy TiO<sub>2</sub> seeds formed on alumina substrates after the seeded substrate was inserted into a low temperature zone while



supplying Ti vapour species generated from a high temperature zone. The transport of Ti vapour species condensing on the seeds grew as nanowires. Diameters for the nanowires included in the range of 50-100nm and length between the ranges of 1-2 $\mu$ m [2.46].

## 2.7 Doping of TiO<sub>2</sub>

Doping refers to the deliberate introduction of impurities into a pure crystal to induce a change in the electrical properties. Most commonly doping is used on semiconductors to increase conductivity by reducing the large gap between the valence and conduction bands. Practical applications arise from the photocatalytic reactions at the surface of TiO<sub>2</sub>. A relatively high reactivity and chemical stability is present in TiO<sub>2</sub> under ultraviolet light, exceeding the bandgap of 3.3 eV for the anatase crystalline phase. Photo-catalysts for high reactivity under visible light allows for the peak of the solar spectrum to be utilised. Modification of TiO<sub>2</sub> has been proposed including: metal-ion implantation with the use of transition metals: Cu, Co, Ni, Cr, Mn, Mo, Nb, V, Fe, Ru, Au, Ag, Pt. Reduced TiO<sub>x</sub> photo catalysts, non-metal doped-TiO<sub>2</sub> (N, S, C, B, P, I, F) composites of TiO<sub>2</sub> with semiconductors having a lower bandgap energy (Cd-S particles), sensitising of TiO<sub>2</sub> with dyes and TiO<sub>2</sub> doped with up-conversion luminescence agent [2.47].

Absorption of the photon  $h\nu_1$  is the initial stage of the photocatalytic mechanism with energy greater or equal to the band gap of TiO<sub>2</sub> (3.3 eV for the anatase phase), producing an electron-hole pair on the surface of the nanostructure. Metal-doped TiO<sub>2</sub> visible light photo-activity is explained by the new energy level produced in the bandgap of TiO<sub>2</sub> by the dispersion of metal nanoparticles in the TiO<sub>2</sub> matrix. Transition metal doping has an additional advantage of improving trapping of electrons to inhibit electron-hole recombination during irradiation. With the decrease of charge carriers recombination resulting in enhanced photo-activity [2.47].

Popular hypothesis of the modification mechanism of TiO<sub>2</sub> doped with non-metals are: (1) bandgap narrowing, (2) impurity energy levels and (3) oxygen vacancies. Asashi *et al* [2.48] found that N 2p state hybrids with O 2p states in anatase TiO<sub>2</sub> doped with nitrogen due to the similar energies and the shortening of the bandgap of N-TiO<sub>2</sub> to absorb visible light. Irie *et al* [2.49] found

that TiO<sub>2</sub> oxygen sites substituted with N<sub>2</sub> atoms form isolated impurity energy levels in the valence band. UV light irradiation excites the electrons in both the VB and impurity levels, with visible light illumination only exciting electrons in the impurity energy level. Ihara *et al* [2.50] observed that oxygen-deficient sites formed in the grain boundaries are integral to emerge vis-activity and n-doped in part of oxygen-deficient sites performs the role of the blocker for re-oxidation. Zhao [2.51] investigated N-TiO<sub>2</sub> and found that TiO<sub>2</sub> doped with substitutional N<sub>2</sub> has shallower acceptor states above the valence state. While, TiO<sub>2</sub> doped with interstitial N<sub>2</sub> has an isolated impurity states in the middle of the bandgap. Hybridized by the N 2p and O 2p states.

## 2.8 Plasma Treatment

### 2.8.1 Overview

Physically, plasma is an ionised gas with an essentially equal density of positive and negative charges. Existing over various ranges of temperature and pressure. Plasma treatment of materials base reactions on free radical chemistry. The density of the plasma creates free radicals both in the gas phase and in the surface of organic materials. Surface radicals created by direct gas-phases free-radicals, ions or photo-decomposition of the surface by vacuum-ultraviolet light generated in the primary plasma. Surface free-radicals react together or with species in the plasma environment.

There are four major effects caused by free radicals at low pressure gas plasma on organic substrates: (1) surface cleaning, (2) ablation (micro-etching), (3) crosslinking and (4) surface activation. These effects occur simultaneously, depending on conditions one may dominate. The effects only penetrate the top few layers of the material and therefore do not change the appearance or bulk of the material. Major improvements can include bonding, printing, painting and wettability for processes that require adhesion [2.52].

Though the plasma's ionised gas is neutral, the ions nearest to the electrodes or material surfaces can be accelerated by sheath voltage to 10s of eV energies. Accelerated ions like these may cause bond breaking and generate free radicals in the material surface. During the plasma treatment of

samples, reactions are rooted in free-radical chemistry. Gas phase free radicals of high density are efficiently generated by the glow discharge with bombardment and photochemical processes. A large amount of the free radicals remains in the ground state. While a portion of the free radicals that have more energy exist in excited states.

When organic surfaces are exposed to gas-phase radicals or ions, the radicals/ions have the right amount of energy to break the bonds in that surface. With the bonds broken in the surface, abstraction occurs of the atoms and molecular fragments. Further reaction in the plasma is possible, forming a volatile species to be removed under the vacuum. Abstraction results in a prolonged ablation of the organic surface and the formation of leftover free radicals in the surface. Cross linking due to ablation or reaction to the plasma gas may even occur for the ground state molecules, resulting in the formation of newer chemical species in the surface. Inert gases produce a large number of stable radicals in the surface until the sample is exposed to a reactive gas [2.52].

### 2.8.2 *Types of Species*

Plasma processing involves many different gases and gas combinations depending on the surface type modification to be desired. Oxidising gases such as O<sub>2</sub>, air, N<sub>2</sub>O and H<sub>2</sub>O are used in the removal of organics by oxidation and implantation of oxygen species in the surface of the polymer. Reducing gases such as H<sub>2</sub> or mixtures of H<sub>2</sub> are used in the replacement of Fluorine and Oxygen in surfaces while also facilitating the removal of organics on oxidation sensitive materials. Volatile low molecular-weight species that do not polymerise or re-deposit on adjacent surfaces are converted from the contamination. Noble gases such as Ar or He generate free radicals in surfaces, causing (i) cross linking, (ii) leaving active sites for a later reaction with a purge gas. Other gases use the noble gases as diluents to increase ultraviolet light, increasing dissociation of the other gases. Active gases such as NH<sub>3</sub> will cause surfaces to be implanted with amino groups that are known to react covalently with adhesives, epoxies. Fluorinated gases such as CF<sub>4</sub> and SF<sub>6</sub> have a replacement effect, replacing the H with F or CF<sub>x</sub> in the polymer surfaces that contain minimal amounts of oxygen. This results in good chemical inertness on a low energy surface that is hydrophobic. The presence of oxygen in the boundary layer is a problem as competition arises

with reactional fluorination to produce polar oxygen-species in the surface. Polymerising gases have been used for direct polymerisation of layered coatings onto substrates [2.52].

## 2.9 TiO<sub>2</sub> Doping using Plasma Techniques

One of the most effective means for bandgap narrowing via mixing of the 2p state of substituted N with the 2p state of O in the TiO<sub>2</sub> lattice is nitrogen-doped TiO<sub>2</sub>. Sources include N<sub>2</sub> gas, ammonium chloride, ammonia gas or N-containing compounds. Doping occurs into TiO<sub>2</sub> photocatalysts for the enhancement of photocatalytic activity in the visible light range. Documented methods for prepared N-TiO<sub>2</sub> include surface treatment of TiO<sub>2</sub> by sputtering or plasma, plasma enhanced chemical vapour deposition (PECVD) process, pulse laser deposition and the ion-assisted electron beam evaporation method [2.48]. Much research has been done in the acceptance of TiN doping in TiO<sub>2</sub> photocatalyst having a positive effect on the visible light photocatalytic activity since Asahi [2.48]. N-doping exists in other types such as (NO), (NO<sub>2</sub>) and (O-Ti-N) with visible light absorbance being the contributed by TiN and (NO) doping.

A trend appeared to favour TiN for an increase in visible light photocatalytic activity with (NO) doping having a negative effect on visible light photocatalytic activity. N-doped anatase TiO<sub>2</sub> powders were prepared by Sato *et al* [2.53] and Yin *et al* [2.54] which found (NO) doping as the sole status of N-doped TiO<sub>2</sub>. Result in their work showed -(NO) at the N 1s binding energy of ~400 eV as an effective N-doping site. An observed peak at 399.6 eV by Diwald *et al* [2.55] is responsible for the shifting of the photochemical threshold to about 2.4 eV. A probable located nitrogen interstitial site bound to hydrogen is formed. N 2p states may be the cause of visible light induced photocatalytic activity. An observation by Di Valentine *et al* [2.56] noted that N-doping has opposing effects for the photoactivity of anatase and rutile TiO<sub>2</sub> due to different densities and structures. Resulting in a red shift and a blue shift of the absorption band-edge. For both the anatase and rutile case the doping is found with indication of well-localised N 2p states above the O 2p valence band, but in rutile the shift of the top of the valence band toward lower energies lead to an increased band gap transition.



## 2.10 TiO<sub>2</sub> as an Electron Transport Layer (ETL)

Porous crystalline TiO<sub>2</sub> remains a widely used industry standard charge transport layer for use in dye-sensitised solar cells. Overall, studies show that power conversion efficiency of TiO<sub>2</sub> based devices depends a great amount on the structure of the TiO<sub>2</sub> utilised. Films or arrays that have well-defined morphology and are homogeneous in nature, with crystal size on average 50 nm is characterised with an optimised morphology and interaction. Which in turn favours exciton dissociation and charge separation. Less charge recombination occurs with improved charge transport through the inorganic layer.

## 2.11 Summary

TiO<sub>2</sub> is prominent as photo-catalyst, with applications in degrading organic pollutants, photo-water splitting, reverse osmosis, high efficiency DSSCs and an active role as an ETL. The rutile phase of TiO<sub>2</sub> is highly stable and therefore continued research has focussed on its development. The rutile and the anatase phase both have a tetragonal crystal structure. In TiO<sub>2</sub>, the crystal structure can be described by chains of TiO<sub>6</sub> octahedra. There is a trend indicates that equally sized nanoparticles for anatase, rutile and brookite are thermodynamically stable for TiO<sub>2</sub> nanocrystal dimensions diameter: smaller than 11 nm, greater than 35 nm and between 11 nm and 35 nm respectively. Electrical properties of TiO<sub>2</sub> are comparable with other transition metal-oxides with a bandgap of between 2.5-3.5 eV. It was established that an effective means for bandgap narrowing via mixing of the 2p state of substituted N with the 2p state of O in the TiO<sub>2</sub> lattice is nitrogen-doped TiO<sub>2</sub>. A trend appeared to favour TiN for an increase in visible light photocatalytic activity with (NO) doping having a negative effect on visible light photocatalytic activity. Which further increase TiO<sub>2</sub> and N-doped TiO<sub>2</sub> characteristics as an ETL.



## References

- [2.1] E. Pelizzetti, C. Minero, “*Mechanism of the photo-oxidative degradation of organic pollutants over TiO<sub>2</sub> particles*”, *Electrochim. Acta.* 38 (1993) 47
- [2.2] R. Breckenridge, W. Hosler, “*Electrical properties of titanium dioxide semiconductors*”, *Phys. Rev.* 91 (1953) 793
- [2.3] C. Sanchez, M. Escuti, C. van Heesch, C. Bastiaansen, D. Broer, J. Loos, R. Nussbaumer, “*TiO<sub>2</sub> nanoparticle-photopolymer composites for volume holographic recording*”, *Adv. Fun. Mater.* 15 (2005) 1623
- [2.4] S. Hwang, P. Shen, H. Chu, T. Yui, “*Nanometer-size  $\alpha$ -PbO<sub>2</sub>-type TiO<sub>2</sub> in garnet: a thermobarometer for ultrahigh-pressure metamorphism*”, *Sci.* 288 (2000) 321
- [2.5] A. Czanderna, C. Rao, J. Honig, “*The anatase-rutile transition. part I-kinetics of transformation of pure anatase*”, *Trans. Faraday Soc.* 54 (1958) 1069
- [2.6] R. Spurr, H. Myers, “*Quantitative analysis of anatase-rutile mixtures with an x-ray diffractometer*”, *Anal. Chem.* 29 (1957) 760
- [2.7] A. Linsebigler, G. Lu, J. Yates, “*Photocatalysis on TiO<sub>2</sub> surfaces – principles, mechanisms, and selected results*”, *Chem. Rev.* 95 (1995) 735
- [2.8] U. Diebold, “*The surface science of titanium dioxide*”, *Surf. Sci. Rep.* 48 (2003) 53
- [2.9] X. Wang, Z. Li, J. Shi, Y. Yu, “*One-dimensional titanium dioxide nanomaterials: nanowires, nanorods, and nanobelts*”, *Chem. Rev.* 114 (2014) 11330
- [2.10] D. Vogtenhuber, R. Podloucky, A. Neckel, S. Steineman, A. Freeman, “*Electronic structure and relaxed geometry of the TiO<sub>2</sub> rutile (110) surface*”, *Phys. Rev. B.* 49 (1994) 2099
- [2.11] H. Zhang, J. Banfield, “*Thermodynamic analysis of phase stability of nanocrystalline titania*”, *J. Mater. Chem.* 8 (1998) 2073
- [2.12] W. Li, C. Ni, H. Lin, C. Huang, S. Shah, “*Size dependence of thermal stability of TiO<sub>2</sub> nanoparticles*”, *J. Appl. Phys.* 96 (2004) 6663
- [2.13] X. Ye, J. Sha, Z. Jiao and L. Zhang, “*Thermoanalytical characteristic of nanocrystalline brookite-based titanium dioxide*”, *Nano. Mat.* 8 (1997) 919
- [2.14] T. Mitsuhashi, O. Kleppa, “*Transformation enthalpies of the TiO<sub>2</sub> polymorphs*”, *J. Am. Ceram. Soc.* 62 (1979) 356

- [2.15] H. Zhang, J. Banfield, “*Understanding polymorphic phase transformation behaviour during growth of nanocrystalline aggregates: insights from TiO<sub>2</sub>*”, J. Phys. Chem. B. 104 (2000) 3481
- [2.16] M. Ranade, A. Navrotsky, H. Zhang, J. Banfield, S. Elder, A. Zaban, P. Borse, S. Kulkarni, G. Doran, H. Whitfield “*Energetics of nanocrystalline TiO<sub>2</sub>*”, P. Nat. Acad. Sci. USA 99 (2002) 6476
- [2.17] A. Barnard, L. Curtiss, “*Prediction of TiO<sub>2</sub> nanoparticle phase and shape transitions controlled by surface chemistry*”, Nano. Lett. 5 (2005) 1261
- [2.18] H. Yang, C. Sun, S. Qiao, J. Zou, G. Liu, S. Smith, H. Cheng, G. Lu, “*Anatase TiO<sub>2</sub> single crystals with a large percentage of reactive facets*”, Nature 253 (2008) 638
- [2.19] X. Feng, K. Shankar, O. Varghese, M. Paulose, T. Latempa, C. Grimes, “*Vertically aligned single crystal TiO<sub>2</sub> nanowire arrays grown directly on transparent conducting oxide coated glass: synthesis details and applications*,” Nano. Lett. 8 (2008) 3781
- [2.20] Z. Cui, F. Wu, H. Jiang, “*First-principles study of relative stability of rutile and anatase TiO<sub>2</sub> using the random phase approximation*”, Phys. Chem. Chem. Phys. 18 (2016) 29914
- [2.21] W. Gopel, J. Anderson, D. Frankel, M. Jaehnig, K. Phillips, J. Schafer, G. Rocker, “*Surface study of TiO<sub>2</sub> (110): a combined xps, xaes and els study*”, Surf. Sci. 139 (1984) 333
- [2.22] Z. Zhang, S. Jeng, V. Henrich, “*Cation-ligand hybridisation for stoichiometric and reduced TiO<sub>2</sub> (110) surfaces determined by resonant photoemission*”, Phys. Rev. B. 43 (1991) 12004
- [2.23] R. Tait, R. Kasowski, “*Ultraviolet photoemission and low-energy-electron diffraction of TiO<sub>2</sub> (rutile) and (001) and (110) surfaces*”, Phys. Rev. B. 20 (1979) 5178
- [2.24] K. Tsutsumi, O. Aita, K. Ichikawa, “*X-ray Ti K band structures of oxides of titanium*”, Phys. Rev. B. 15 (1997) 4638
- [2.25] D. Allan, M. Teter, “*Local density approximation of total energy calculations for silica and titania structure and defects*”, J. Am. Ceram. Soc. 73 (1990) 3247
- [2.26] K. Vos, “*Reflectance and electroreflectance of TiO<sub>2</sub> single crystals. II. assignment to electronic energy levels*”, J. Phys. Chem. 10 (1977) 3917
- [2.27] K. Glassford, J. Chelikowsky, “*Structural and electronic properties of titanium dioxide*”, Phys. Rev. B. 46 (1992) 1284

- [2.28] M. Knotek, P. Feibelman, “*Ion desorption by core-hole Auger decay*”, Phys. Rev. Lett. 40 (1978) 964
- [2.29] D. Fischer, “*X-ray band spectra and molecular-orbital structure of rutile TiO<sub>2</sub>*”, Phys. Rev. B. 5 (1972) 4219
- [2.30] L. Grunes, “*Study of K edges in 3d transition metals in pure and oxide form by x-ray-absorption spectroscopy*”, Phys. Rev. B. 27 (1983) 2111
- [2.31] M. Cardona, G. Harbeke, “*Optical properties and band structure of wurtzite-type crystals and rutile*”, Phys. Rev. 137 (1965) 1467
- [2.32] A. Frova, P. Boddy, Y. Chen, “*Electromodulation of the optical constants of rutile in the UV*”, Phys. Rev. 157 (1967) 700
- [2.33] J. Pascual, J. Camassel, H. Mathieu, “*Band-structure enhancement of the indirect forbidden transitions*”, Phys. Rev. B. 20 (1979) 5292
- [2.34] F. Arntz, Y. Yacoby, “*Electroabsorption in rutile (TiO<sub>2</sub>)*”, Phys. Rev. Lett. 17 (1966) 857
- [2.35] S. Lai, J. Guo, V. Petrova, G. Ramanath, L. Allen, “*Size-dependent melting properties of small tin particles: noncalorimetric measurements*”, Phys. Rev. Lett. 77 (1996) 99
- [2.36] M. Hybertsen, S. Louie, “*Electron correlation in semiconductors and insulators: bandgaps and quasiparticle energies*”, Phys. Rev. B. 34 (1986) 5390
- [2.37] S. Svane, O. Gunnarsson, “*Transition metal-oxides in the self-interaction-corrected density-functional formalism*”, Phys. Rev. Lett. 65 (1190) 1148
- [2.38] H. Ehrenreich, M. Cohen, “*Self-consistent field approach to the many electron problem*”, Phys. Rev. 115 (1959) 786
- [2.39] J. Pascual, J. Camassel, H. Mathieu, “*Resolved quadrupolar transition in TiO<sub>2</sub>*”, Phys. Rev. Lett. 39 (1977) 1490
- [2.40] J. Wu, H. Shih, W. Wu, “*Formation and photoluminescence of single crystalline rutile TiO<sub>2</sub> nanowires synthesised by thermal evaporation*”, Nanotech. 17 (2006) 105
- [2.41] J. Wu, C. Yu, “*Aligned TiO<sub>2</sub> nanorods and nanowalls*”, J. Phys. Chem. B. 108 (2004) 3377
- [2.42] M. Paulose, K. Shankar, S. Yoriya, H. Prakasam, O. Varghese, G. Mor, T. Latempa, A. Fitzgerald, C. Grimes, “*Anodic growth of highly ordered TiO<sub>2</sub> nanotube arrays to 135 μm in length*”, J. Phys. Chem. B. 110 (2006) 16179

- [2.43] G. Mor, O. Varghese, M. Paulose, K. Shankar, C. Grimes, “*A review on highly ordered, vertically orientated TiO<sub>2</sub> nanotube arrays: fabrication, material properties, and solar energy applications*”, Sol. Ener. Mat. Sol. C. 90 (2006) 2011
- [2.44] B. Liu, J. Boercker, E. Aydil, “*Oriented single crystalline titanium dioxide nanowires*”, Nanotech. 19 (2008) 505604
- [2.45] B. Liu, E. Aydil, “*Growth of orientated single-crystalline rutile TiO<sub>2</sub> nanorods on transparent conduction substrates for dye-sensitised solar cells*”, J. Am. Chem. Soc. 131 (2009) 3985
- [2.46] B. Dinan, S. Akbar, “*One-dimensional oxide nanostructures produced by gas phase reaction*”, F. Mat. Lett. 2 (2009) 87
- [2.47] A. Zaleska, “*Doped-TiO<sub>2</sub>: a review*”, Rec. Pat. Eng. 2 (2008) 157
- [2.48] R. Asahi, T. Morikawa, T. Ohwaki, J. Aoki, Y. Taga, “*Visible-light photocatalysis in nitrogen-doped titanium dioxide*”, Science 293 (2001) 269
- [2.49] H. Irie, Y. Watanabe, K. Hashimoto, “*Nitrogen-concentration dependence on photocatalytic activity of TiO<sub>2-x</sub>N<sub>x</sub> powders*”, J. Phys. Chem. B. 107 (2003) 5483
- [2.50] T. Ihara, M. Miyoshi, Y. Triyama, O. Marsumato, S. Sugihara. “*Visible-light-active titanium oxide photocatalyst realised by an oxygen-deficient structure and by nitrogen doping*,” Appl. C. B. 42 (2003) 403
- [2.51] Z. Zhao, Q. Liu, “*Mechanism of higher photocatalytic activity of anatase TiO<sub>2</sub> doped with nitrogen under visible-light irradiation from density functional theory calculation*”, J. Phys. D. Appl. Phys. 41 (2008) 1
- [2.52] E. Liston, “*Plasma treatment for improved bonding: a review*”, J. Adh. 30 (1989) 199
- [2.53] S. Sato, R. Nakamura, S. Abe, “*Visible-light sensitisation of TiO<sub>2</sub> photocatalysts by wet method N-doping*”, S. Appl. C. 284 (2005) 131
- [2.54] S. Yin, Y. Aita, M. Komatsu, J. Wang, Q. Tang, T. Sato, “*Synthesis of excellent visible-light responsive TiO<sub>2</sub>xNy photocatalyst by a homogeneous precipitation-solvothermal process*”, J. Mat. Chem. 15 (2005) 675
- [2.55] O. Diwald, T. Thompson, T. Zubkov, E. Goralski, S. Walck, J. Yates, “*Photochemical activity of nitrogen-doped rutile TiO<sub>2</sub>(110) visible light*”, J. Phys. Chem. B. 108 (2004) 6004



- [2.56] C. Di Valentin, G. Pacchioni, A. Selloni, “*Origin of the different photoactivity of N-doped anatase and rutile TiO<sub>2</sub>*”, Phys. Rev. B. 70 (2004) 085116
- [2.57] S. Lattante, “*Electron and hole transport layers: their use in inverted bulk heterojunction polymer solar cells*”, Elec. 3 (2014) 132





## Chapter 3: Experimental and Analytical Techniques

---

In this section the experimental process of synthesising TiO<sub>2</sub> NWs as well as the Nitrogen treatment. The well-established growth model for TiO<sub>2</sub> NWs is detailed as well as doping mechanism used for Nitrogen gas under various conditions. Sample preparation and lab conditions are detailed in tandem with equipment and chemicals utilised in synthesis.

### 3.1 Introduction

Over the last decade, the hydrothermal technique has increased in popularity, finding interest from engineers, researchers and scientists of all disciplines. An understanding of the mineral formation in nature under elevated pressure and temperature conditions in the presence of water led to the development of the hydrothermal technique. Studies of the mineral formation under raised temperature and pressure in nature broke new ground in the development of the hydrothermal technique. In 1845 Schaffhaul reported the earliest success in implementing the hydrothermal method to obtain quartz crystals via transformation of silicic acid that was newly precipitated in Papin's digester. Applications in the commercial sector took off when Karl Josef Bayer in 1892 reported the use of sodium hydroxide to leach bauxite to obtain pure aluminium hydroxide. The aluminium hydroxide could then be converted to Al<sub>2</sub>O<sub>3</sub> for further processing [3.1]. Further importance of the hydrothermal technique for the synthesis of inorganic compounds in a commercial way was realised soon after the synthesis of large single crystals of quartz by Nacken and zeolites by Barrer during late 1930s and 1940s, respectively. In the recent years, hydrothermal synthesis of 1-dimensional TiO<sub>2</sub> (titania) nanostructures have found much interest amongst researchers. The chemical process has many advantages, namely 1D nanowires can be grown in numerous amounts and is relatively inexpensive [3.1].

Another advantage is the production of highly uniform crystalline structure, which can be consistently obtained at temperatures lower than 150°C. A decreased agglomeration between particles remain the most important feature in the hydrothermal synthesis. This also includes a

decrease in narrow particle size distributions, controlled particle morphology and phase homogeneity. Homogeneous composition, mono-dispersed particles, size and shape control as well as product purity all are featured advantages. Desired shape and size have seen the best results with the hydrothermal technique with uniformity in composition and crystallinity of a high degree. TiO<sub>2</sub> nanowires can be synthesized in small autoclaves of the type Morey, with Teflon<sup>®</sup> liners inserted inside. Synthesis conditions are selected at temperatures smaller than 200°C and pressures smaller than 100 bars. Teflon<sup>®</sup> liners facilitate the use of autoclaves to produce uniform and pure TiO<sub>2</sub> NWs.

In this chapter, the chemical understanding for the hydrothermal synthesis for TiO<sub>2</sub> will be explored as well as the Plasma Vapour Deposition system. Furthermore, experimental details of the sample preparation, NW growth and nitrogen treatment will also be discussed. This chapter concludes by describing the procedure that was followed for the NW growth and plasma treatment.

### **3.2 Hydrothermal Synthesis**

Researchers have reported extensively on the mild hydrothermal synthesis of TiO<sub>2</sub> particles/nanowires and the influence of various parameters. Parameter including temperature, duration, pressure (percentage fill), solvent type, pH, and the starting charge on the resultant product [3.2-3.5]. It is worth mentioning that the size of the titania crystallite is a most important factor for the performance of the material's photocatalytic activity, and the mono-dispersed nanoparticles have the best reported performance. A crucial factor is the particle size. The particle size influences the electron/hole recombination process, which drives the benefits from extreme surface area of nanocrystalline TiO<sub>2</sub>. TiO<sub>2</sub> has shown differing dominant e-h recombination pathways. Regimes of differing particle sizes are well documented for improvement in the photocatalytic efficiencies of different systems [3.6].

Crystallisation process occurs in autoclaves. Autoclaves are usually containing a Teflon<sup>®</sup> reactor and a metal high pressure vessel. Conducting a hydrothermal process, firstly a substrate containing solution and precursor is placed in the autoclave. As heating of the autoclave occurs,

supersaturation will in turn occur, resulting in the metal-oxide seed nucleate on the said substrate and the metal oxide to grow along the direction of the crystal. Size and morphology of the metal oxide can usually be controlled by changing the substrates, precursors, solvents, temperature, reaction time, concentration of the solution, and pH value of the solution.

Within the autoclave and Teflon® liner, when the boiling point is reached and exceeded, this causes the internal pressure within the autoclave to be also increased, resulting in the boiling temperature becoming higher. Precipitation starts to occur when a saturated solution is formed. This precipitation occurs on the substrate and in some reported cases in the solution. One advantage to this method is that single crystal semiconductors can be synthesised without the need for extreme temperature. Development of two procedures have been researched to grow TiO<sub>2</sub> nanowires and TiO<sub>2</sub> nanotubes with homogeneous morphologies; using an alkali solution and using an acid solution.

TiO<sub>2</sub> nanotubes were first researched by Kasuga *et al* grown in NaOH solution with the hydrothermal method [3.7]. Similar results have been reported on with various growth conditions [3.8, 3.9]. It was shown in these studies that morphology is influenced by the growth conditions. A possibility as to why this occurs is the Teflon® liner's size. The size of the Teflon® liner determines at which pressure rises to during synthesis. Using alkali solutions, results in titania formation. TiO<sub>2</sub> with the preferred single crystal structures can be obtained by heat treatment at various temperatures. Rutile and anatase nanowire growth are well suited using the hydrothermal method [3.10-3.12].

Researchers Liu and Feng, reported on two different hydrothermal procedures growing TiO<sub>2</sub> nanowire arrays on transparent conductive oxide (TCO) substrates [3.13, 3.14]. During experimentations which resulted in the growth of super-hydrophobic TiO<sub>2</sub> nanorods arrays, [3.15] Feng *et al* replaced water as the solvent with toluene [3.13]. Precursors used in the experiment as for titanium 27 were 1 mL Tetra-butyl titanate (TBT) and 1ml titanium tetrachloride (1 M in toluene) were added to a 23 ml autoclave with 1ml hydrochloric acid 10 ml toluene. Heating at 150 °C for 4 hours resulted in a thick vertical nanowire array TCO observed in Figure 3.1. With the nanowire observed to be 20 nm in diameter and 4 - 20  $\mu\text{m}$  in length.

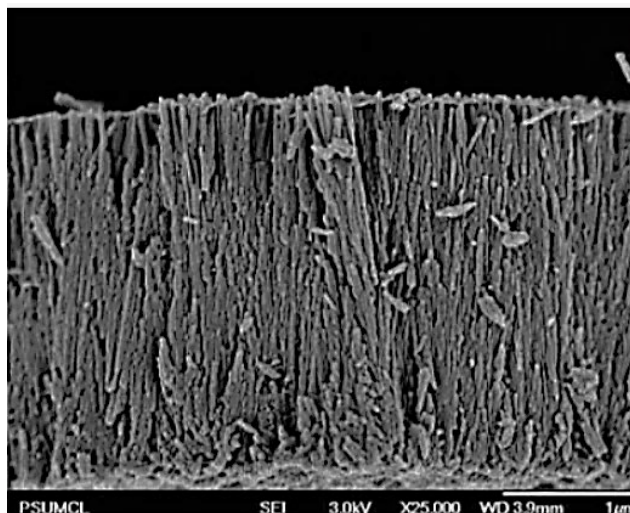


**Fig 3.1:** SEM micrograph of the cross section showing  $\text{TiO}_2$  nanowire array grown in toluene on TCO substrate [3.13]

Liu reported on a hydrothermal procedure for synthesizing nanorods on TCO with water as the solvent, instead of toluene (see Fig. 3.2) [3.14]. The TCO substrate showed nanorods with uniform height at the end of the growth. The nanorods were of the rutile phase. The average observed diameter of a nanorod is 80 nm and the film lengths are seen till 4  $\mu\text{m}$ . In this specific study, various growth parameters were researched, including temperature, growth time, concentration of chloride ion and substrate type. Conclusions the study made are that the hydrothermal method is used to grow nanorods on Fluorine Tin-Oxide (FTO) and that silicon and glass substrates have no nanorod growth [3.14].



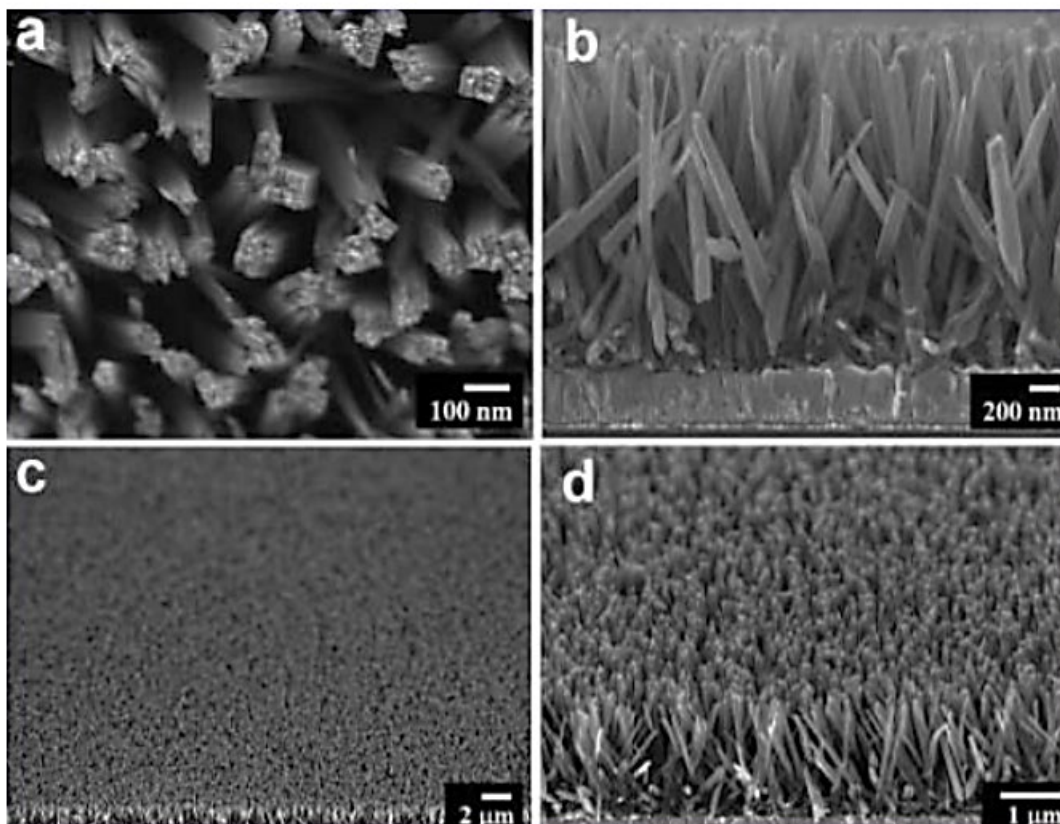


**Fig 3.2:** SEM micrograph showing TiO<sub>2</sub> nanowire array grown using water as a solvent [3.14]

Another significant aspect for hydrothermal synthesis is the chloride ion's role in the solution. Morphology and crystalline structure of the resultant is determined by in part by the chloride ions. It is shown by Hosono *et al* that the TiO<sub>2</sub> nanorod synthesis may occur even in the presence of a saturated NaCl solution [3.15]. NaCl was also reported in Liu's work. An important point to note is, it is only rutile TiO<sub>2</sub> single crystalline nanorods were grown when the reaction had chloride ions present. An explanation that may be given is that the precipitates absorb the chloride ions. While rutile phase became stable in the reaction. Only nanorod shaped structured crystals were grown due to the differing growth speed of the surface. Replacing chloride ions with fluoride ions, a high percentage of anatase TiO<sub>2</sub> single crystals on the (101) surface forms, according to Yang *et al* [3.17]. The Fluoride ions change the free energy of the precipitation by attaching to the surface of TiO<sub>2</sub>. The stable phase then becomes anatase with the (001) surface.



### 3.3 Plasma Vapour Deposition for Nitrogen Treatment

For the last half-century, plasma has been known to affect changes of a desirable nature in the surface properties of materials. Commercial advancements have led to the practise and application of plasma systems becoming reliable and scaled, (see Fig.3.3) . Free radical chemistry is the basis for plasma treatment of all materials. Gas phase, surface of organic materials and even stable polymers can have high density of free radicals thanks to the glow discharge efficiency. Surface free radicals are the result of direct attack of gas-phase free-radicals, ions, or by photodecomposition of the surface by the primary plasma generating vacuum-ultraviolet light [3.16]. The surface free radicals are then able to react either with each other and with species in the plasma environment.

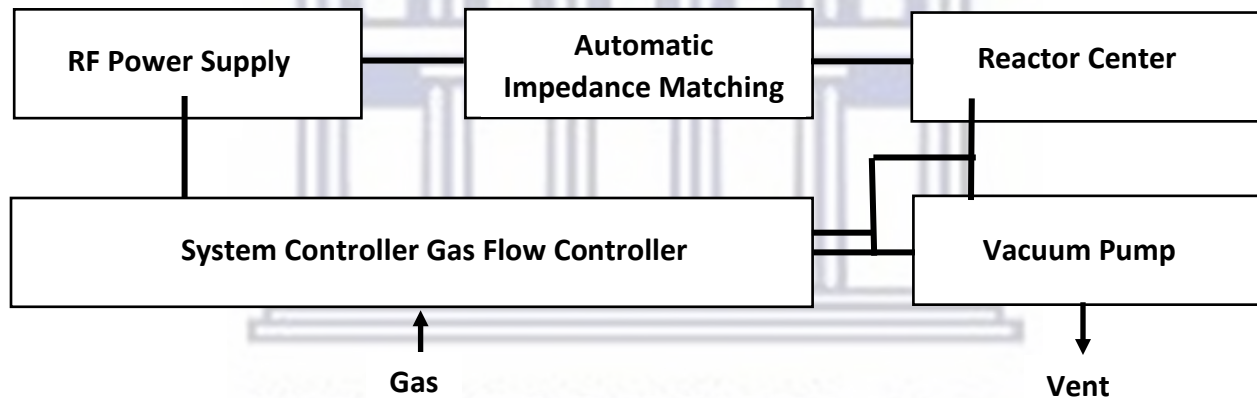


**Fig 3.3:** Schematic of the plasma vapour deposition system [3.16]

### 3.4 Effect of Plasma Exposure on Surfaces

There are four known major effects that plasma has on surfaces. There is always some degree of each effects present; however, depending on substrate chemistry, processing conditions and reactor design one or the other effect can be favoured one effect may be favoured over another. These effects can be categorised as: surface organic contamination cleaning; micro-etching material removal, increasing surface area or removing a weak boundary layer; cross-linking and branching to strengthen the surface cohesively; and the modification of surface chemistry to improve

chemical and physical interactions at the bonding interphase. Surface cleaning is attributed to a significant improving in bonding on plasma treated surfaces. An example given is the known fact that  $0.1 \text{ pg/cm}^2$  contamination of organic material on a metal surface interferes with bonding. This amount corresponds to 1 molecular layer. Stated differently, residual contamination on 1 cm of surfaces amounts to less than 4 drops of liquid containing 10 ppm non-volatile organics. As it is difficult to obtain solvents or water with less than 10ppm non-volatiles, samples generally are contaminated after a rinse with liquid.

Micro-etching is important for the cleaning of heavily contaminated surfaces, the removal of weak boundary layers formed during the synthesis of a part, and for the treatment of filled or semi-crystalline materials. A change in surface of this magnitude can improve mechanical bonding as well as increase the surface area available for chemical interactions. Ion implantation consists of ion bombardment on the target surface. In an experiment, Ghicov *et al* [3.17] prepared N-TiO<sub>2</sub> nanotubes using an ion bombardment of N at the dose of  $1 \times 10^{16}$  ions/cm<sup>2</sup> with an accelerating energy of 60 keV. The study showed the ion bombardment improved a significant band gap decrease, lowering the bandgap from 3.15eV to 2.20 eV, but during the implantation, there was an anatase change to an amorphous phase. Converting to an anatase phase required a calcination step at 450°C for three hours [3.17]. Plasma treatment involves a relatively high consumption of energy during the annealing of the material at high temperatures. Chen *et al* [3.18] mixed titanium tetra-isopropoxide, water vapour, and N<sub>2</sub> stream before feeding it into a plasma reactor. The reactor has two electrodes and an electrical field of 9.6 kV/cm at standard pressure [3.18].

## 3.5 Experimental Procedure

### 3.5.1 Substrate Preparation

In this study single-side, fluorine-doped tin-oxide (F:SnO<sub>2</sub> or FTO, 10 Ω/square, Hartford Glass Company) wafers were used as substrates for the growth of NWs. FTO was specifically chosen as it is found to be stable at high temperatures and a transparent conduction oxide (TCO). Moreover, the preferential tetragonal crystal structure of the SnO<sub>2</sub> lattice allows for direct growth of the TiO<sub>2</sub>

(also tetragonal crystallinity) nanowires, eliminating the need of a seed-layer. The FTO wafers were cut into 2 x 1 cm<sup>2</sup> rectangles, after which they were sequentially ultrasonically cleaned in 2 vol% Hellmanex® aqueous solution and acetone for 5 minutes each, to rid their surfaces of initial contamination. This was followed by rinsing of the FTO wafers with deionised water to remove all traces of organics; the cleaned substrates were finally dried in a stream of nitrogen gas.

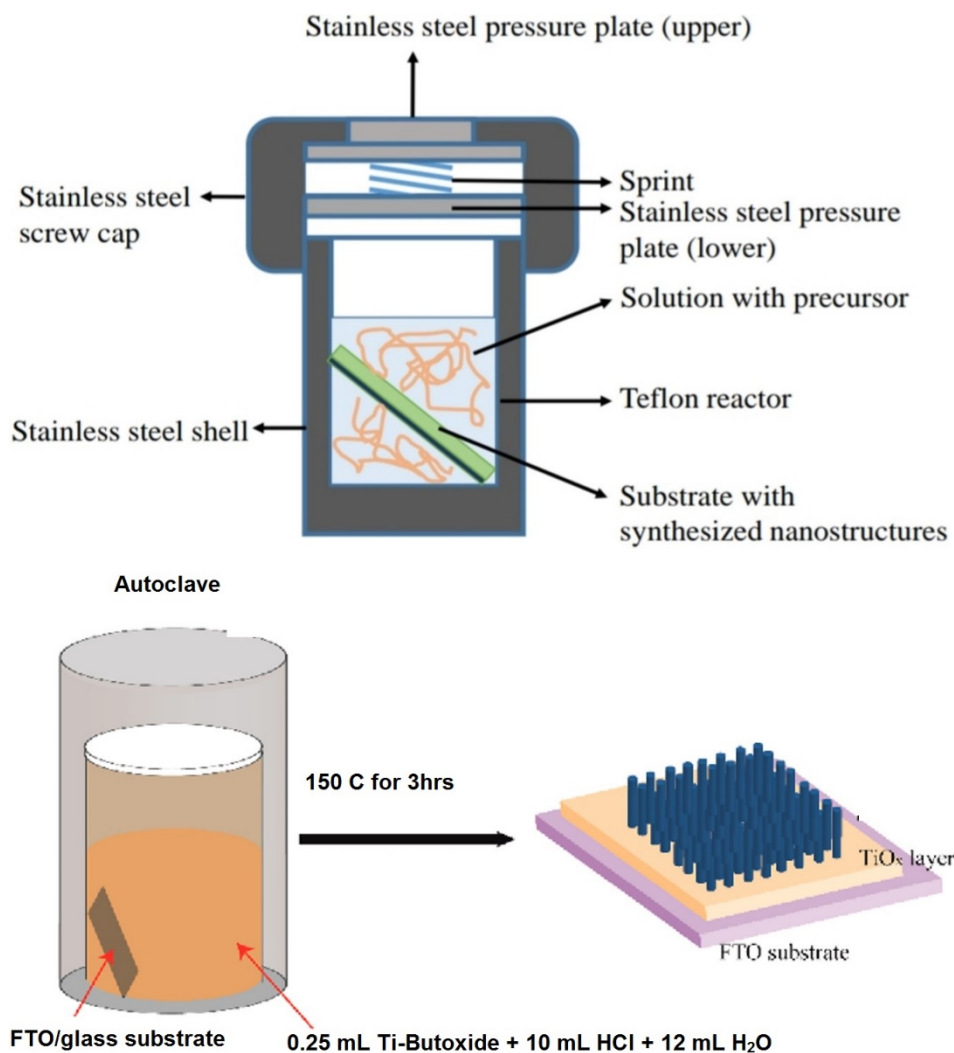


**Fig 3.4:** Schematic representation of the autoclave high-pressure vessel and the associated growth process of the TiO<sub>2</sub> nanowire array at the experimental conditions used in this study [3.16]

### 3.5.2 *TiO<sub>2</sub> Nanowire Growth*

For synthesis (see Fig. 3.4), 12 mL of deionized water was mixed with 10.5 mL of concentrated hydrochloric acid (HCL) and 0.25 mL of titanium butoxide (97% Aldrich) (TBT) to reach a total volume of 22.75 mL in a Teflon®-lined stainless-steel autoclave (125 mL volume, Parr Instrument Co.). The mixture was stirred at ambient conditions for 10 min before the addition of HLC and TBT. After stirring, pieces of FTO substrates, were placed at an FTO-side facing up on a PVC stand in the Teflon®-liner. The hydrothermal synthesis was conducted at 150 °C for 3 hours in an electric oven. After the synthesis, the autoclave was cooled to room temperature under electric fan, which took approximately 30 min. The FTO substrate was taken out, rinsed extensively with deionised water and allowed to dry with nitrogen gas cleaning. This process was repeated 8 times to produce 8 as-synthesised samples.

### 3.5.3 *Plasma Treatment*

Post-synthesis, the substrates are exposed to a radio-frequency (RF) generated N<sub>2</sub> plasma, which allows for controlled N doping of the TiO<sub>2</sub> lattice; this leads to a reduction in oxygen vacancy density and electron transport promotion through the NW array. Plasma treatment was conducted by the UWC: Physics and Astronomy department's Vacu-tech® system (see fig 3.5). Each of the as grown substrates were treated at various conditions. The scope of the N<sub>2</sub> plasma treatment conditions were separated into three series. Power series: 100W, 300W and 500W, Time series: 10 min, 30min, 1hour and Temperature series: Room Temperature, 100°C, and 300°C. The plasma treatment occurred under vacuum, with base pressures approximately at  $1 \times 10^{-5}$  mbar and deposition pressures at approximately  $1 \times 10^{-2}$  mbar. Current utilised was 1.26 A with a voltage of 5 V. Fig 3.6 (left) shows the loading chamber of the Vacu-tech® system where the substrate is placed before it is under vacuum. Fig 3.6 (right) shows the substrate being N<sub>2</sub> treated in the plasma chamber of the Vacu-tech® system with glowing N<sub>2</sub> plasma. Prior to treatment, plasma was calibrated in a N<sub>2</sub>:Ar gas mixture, with a uniform gas flow rate of 100:100 sccm. Once the plasma is successfully ignited, the Ar flow is reduced to 0 sccm, which allows for red glowing plasma (Fig 3.6 right) to interact with the specimen.





**Fig 3.5:** Image of the Plasma vapour deposition system used for N<sub>2</sub> treatment

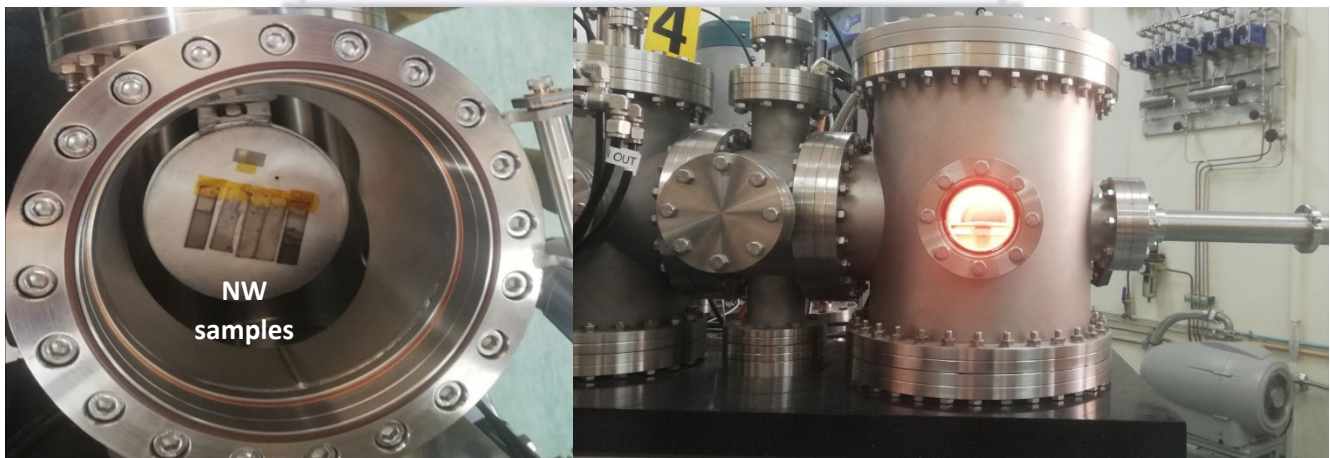


**Fig 3.6:** Images of (left) Vacu-tech loading chamber with nanowire arrays fitted onto heat-able substrate (right) red-glowing N<sub>2</sub> plasma irradiating the nanowire film



# Analytical Techniques

The study of N<sub>2</sub> plasma treated TiO<sub>2</sub> nanowires requires reliable and documented techniques. Table 2.1 shows an overview of the experimental techniques needed for the study of N-doped TiO<sub>2</sub> morphology, structure and properties.

**Table 3.1:** Analytical techniques for the study of N<sub>2</sub> plasma treated TiO<sub>2</sub> nanowires

Technique	Gathered Information
Scanning Electron Microscopy (SEM)	Morphology
Grazing – Incidence X-Ray Diffraction (GIXRD)	Degree of crystal structure and size
X-Ray Photoelectron Spectroscopy (XPS)	Chemical composition of surface and bulk
Ultraviolet-Visible Spectroscopy (UV-Vis)	Transmission of light

## 3.6 Scanning Electron Microscopy

### 3.6.1 Introduction

Modern research has found the scanning electron microscope (SEM) to be vital in various fields of study. Every field from bio-medical science, marine biology, geology and even the semiconductor industry. The images formed during SEM operation gives the characteristic three-dimensional appearance. This allows for the acquisition of relevant information of surface morphology and topography of the sample well into the nanoscale. During the operation of a SEM, thermionically emitted electrons travel from an electron gun which was generated from either cathode or field-emitter [3.19]. The electron gun sits at the top of its own optical-electron column. The emitted electrons form an electron cloud, which in turn is focused by specifically designed and situated electromagnetic lenses, coils and apertures into a fine probe that methodically scans over the specimen surface, producing an image. The generated electrons are accelerated by high voltages towards a specimen containing anode. The electron gun has two condenser lenses situated

below in which focusses the emerging electron beam into a smaller size. The more focused beam is then aligned and focused again by coils and apertures further down the column until the last lens, known as the objective lens nearby the specimen chamber. The objective lens increases demagnification of the beam into a small spot of the range 0.1-1  $\mu\text{m}$ . Intensity of the beam and focusing ability are also controlled by the objective lens. Which ultimately means control of the image brightness [3.19].

### 3.6.2 Resolution of the SEM

The resolution is also known as the resolving power, which can be defined as the closest space of two points which can be seen clearly through the microscope as separate entities. The resolution would still be limited by diffraction effect even if all the lenses of microscope were perfect and given no distortions into the image. Whenever light passes through an aperture, a diffraction happens so that a parallel beam of light is changed into a series of cones, which are seen as circles and are known as Airy rings.

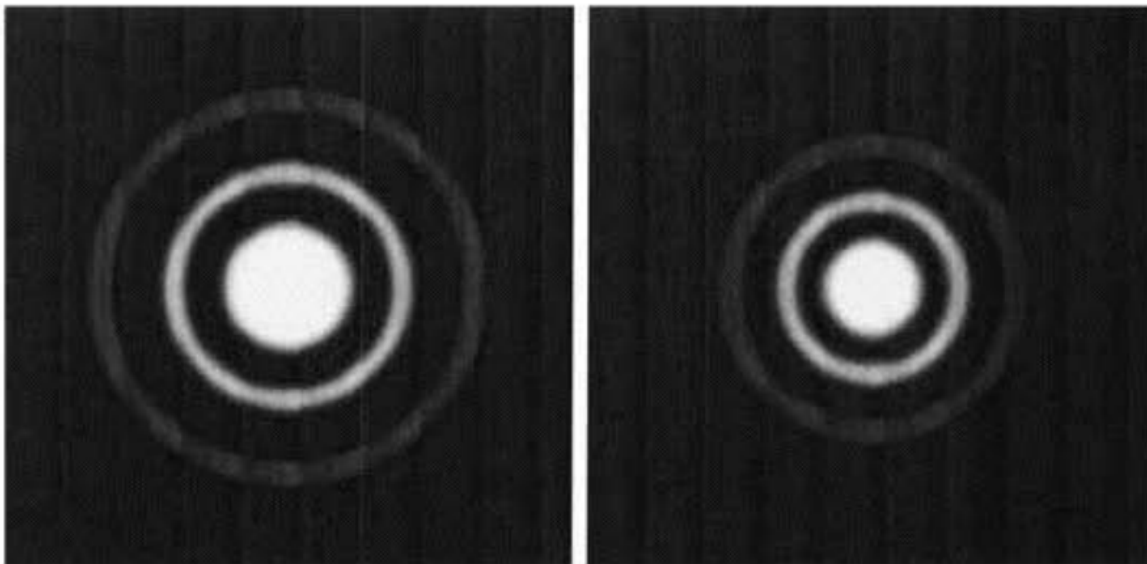


**Fig. 3.7:** Airy rings due to the diffraction of a laser beam by small pinholes left: 75  $\mu\text{m}$  and right: 100  $\mu\text{m}$  [3.19]

The diffraction effects limit the resolution of a microscope because the light from every small point in the object suffers diffraction especially by the objective aperture and even on infinitely small point becomes a small Airy disc image.

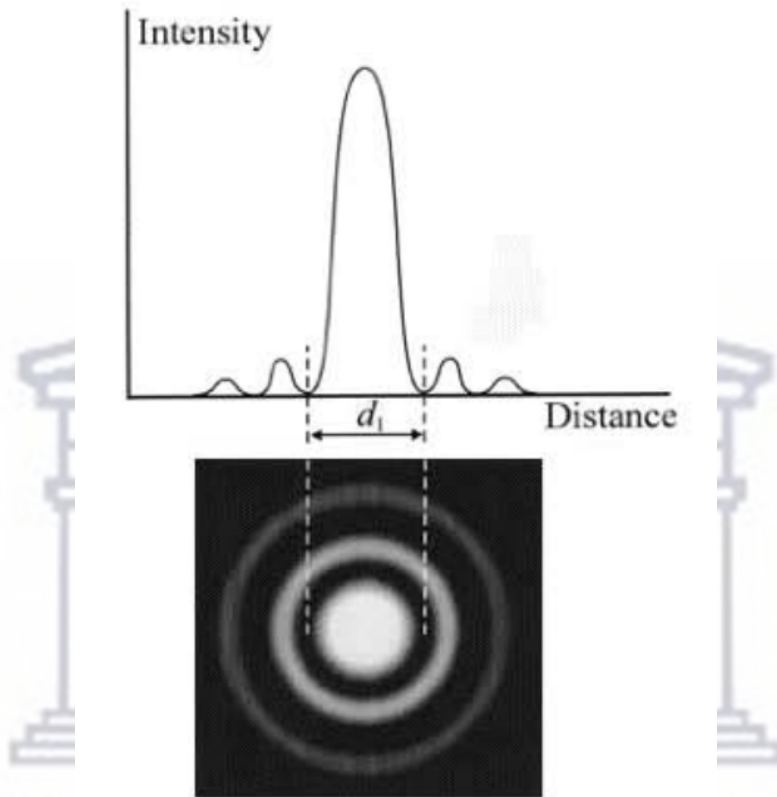


**Fig. 3.8:** Variation of light intensity across a set of Airy rings. Corresponding most intense region being  $d_1$  [3.19]

Above Fig. 3.8 shows the variation of intensity across the series of rings which makes up the disc. The centre region is much more intense than any other ring and contains almost 84% of all light intensity. The remaining rings can be discarded and we can assume that all light falls into a spot of diameter  $d_1$  where  $d_1 \propto 1 / (\text{aperture diameter})$ . Take into consideration how far apart two of these spots must be in the image before they are seen as two. This distance is the resolution.

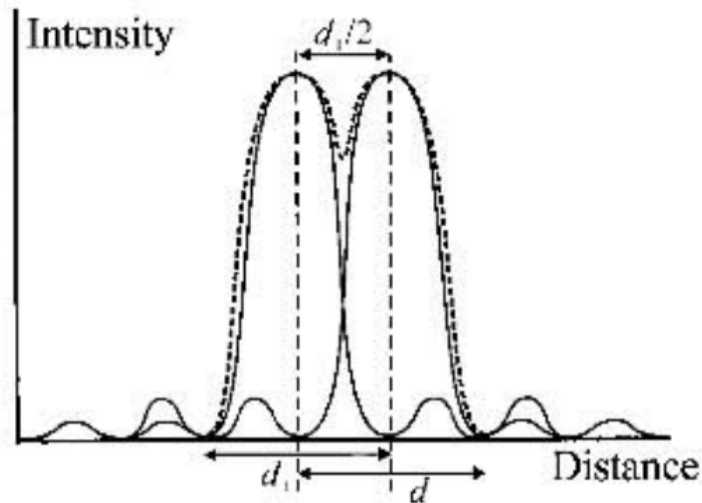


**Fig. 3.9:** Intensity of airy rings from two neighbouring pinholes. Solid lines show intensity distributions. dotted line shows combined profile [3.19]

Fig. 3.9. shows when the maximum of the intensity of an airy disc coincides with the first minimum of the resolution limit is  $d_1/2$ .

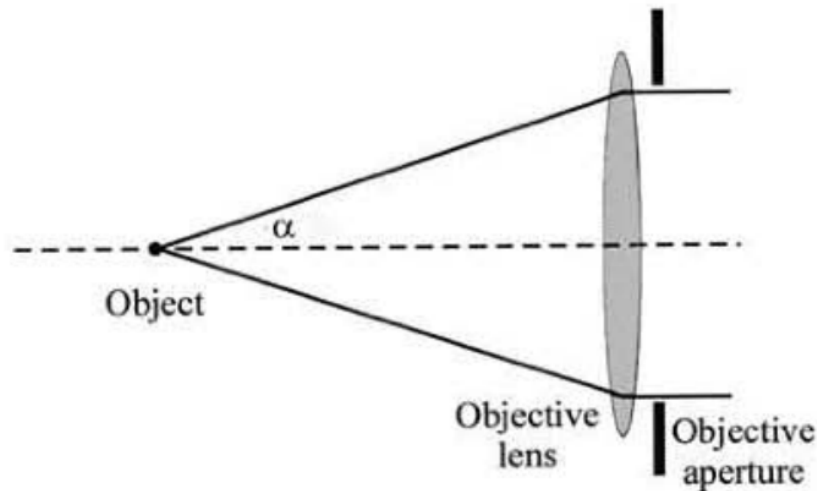


**Fig. 3.10:** Definition of half-angle alpha, subtended by an aperture, in this case the objective aperture [3.19]

Microscope apertures are referred to as semi-angle  $\alpha$  which they subtend at the specimen. It is then possible to derive from diffraction theory the relationship:

$$r_1 = \frac{d_1}{2} = \frac{0.61\lambda}{\mu \sin\alpha} \quad (3.1)$$

Where  $\lambda$  is the wavelength of the light,  $\mu$  is the refractive index of the medium between the object and the objective lens. The product seen as  $\mu \sin\alpha$  is called numerical aperture (NA). The best resolution is obtained by decreasing  $\lambda$  or increasing  $\mu$  or  $\alpha$ . The absolute resolution limit using green light is therefore about 1.50 nm [3.19].

### 3.6.3 Working Distance, Depth of Field and Depth of Focus

Images are only accurately in focus in any microscope when the object is situated in the correct plane. If part of the object being viewed lies either above or below this plane, the equivalent part of the image will be losing focus. The depth of field is therefore known as the range of positions for the object for which our eye can detect no change in the sharpness of the image. Objects must be as flat as possible to produce sharp images as in most microscopes the distance is rather small. The depth of field can be estimated from Fig. 3.11 [3.19].

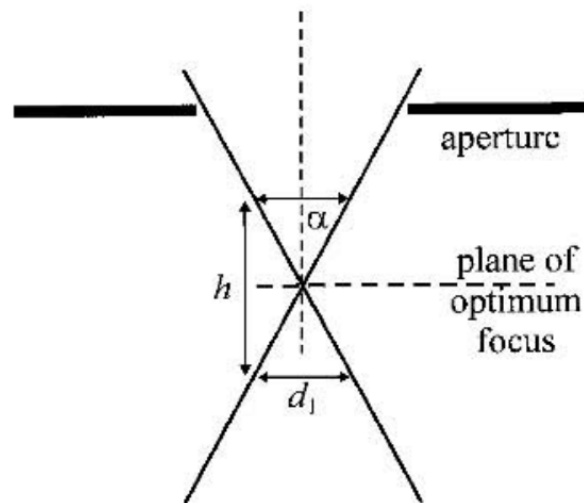


**Fig. 3.11:** Depth of field of an optical system showing both the aperture and the plane of optimum focus [3.19]



It is observed in Fig. 3.11 that for an increase the depth of field there has to be a decrease in the convergence angle controlled by the objective aperture seen in Fig. 3.10. Maximising the depth of field by observing Equation 3.1, finds the resolution deteriorating. This is why electron microscopy is preferred, as there are many associated advantages for increased resolution and depth of field. The number of positions at which images may be viewed without appearing out of focus from a fixed position of an object is known as the depth of focus.

$$\frac{dv}{du} = \frac{-v^2}{u^2} = -M^2 \quad (3.2)$$

Where  $dv$  is the effective shift in the image position and related to  $du$ , the change in position of the object by the square of the magnification. The negative sign in front of the magnification is due to shifts located in opposite directions. Therefore, if the depth of field is  $du$  the depth of focus would be equivalent by a factor  $M^2$  larger. At any reasonable magnification the depth of focus would thus be large. Similarly, at high magnifications the depth of focus would be enormous.

#### 3.6.4 Secondary Electrons and Image Formation

A measurable change in the specimen or associated radiation can be used to provide signal to modulate the CRT and give contrast in the image. Information about the specimen is obtained by distinguishing between each signal that is the product of the interaction between incident electrons and the specimen. Fig. 3.12 shows some of the regions different signals originate from the specimen that can be used in the SEM to form an image. The area into which the electrons penetrate the sample is known as the interaction volume and throughout it is the numerous radiations generated due to inelastic scattering. The generated radiation within the interaction volume is only detected if the signal escapes the specimen, which largely depends on the type of radiation and specimen. As shown in Fig. 3.13, signal origin depends on electron penetration, as secondary electrons are close to the surface, while backscattered electrons lay deeper in the sample. As well as X-rays requiring an even deeper and larger interaction volume within the sample. (3.19)

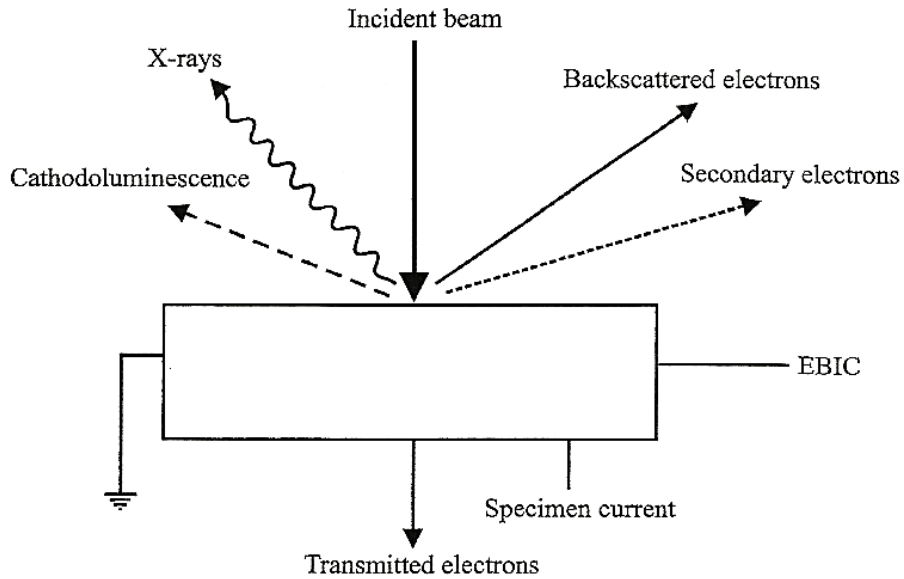


**Fig. 3.12:** Usable SEM signals that originate from the specimen as result of the incident beam and surface interaction [3.19]

Fig. 3.14 shows how backscattered electrons have a broad energy spread of which the highest energy are electrons which have been scattered the fewest amount of times and are generated near the incident beam. These backscattered electrons have the capability of giving information at high spatial resolution and crystallographic information.

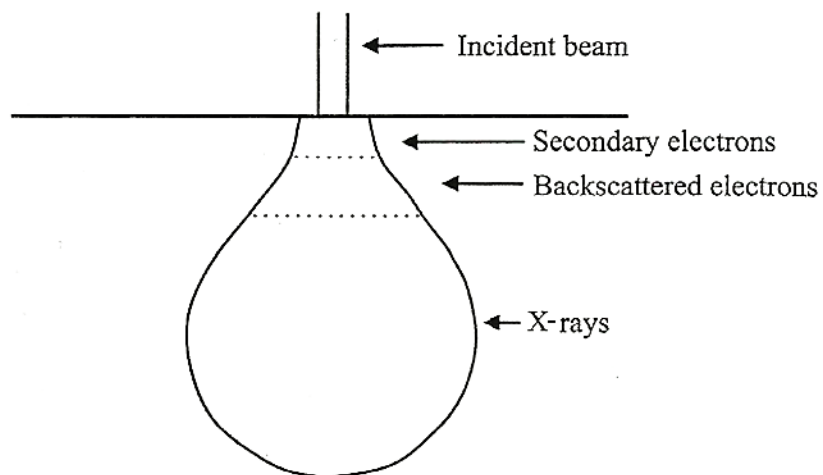


**Fig. 3.13:** Interaction volume and detection regions for secondary electrons, backscattered electrons and x-rays [3.19]

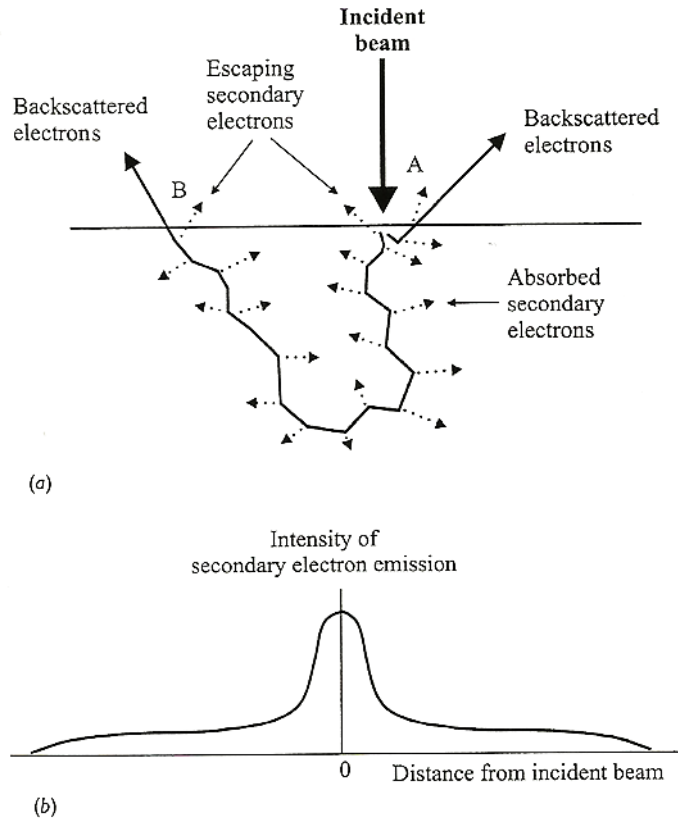


**Fig. 3.14:** (a) Secondary electron generation. (b) Secondary electron spatial distribution [3.19]

Multiple scattering will result in more energy loss for electrons and a larger interaction area within the specimen. This leads to information gathered at worse spatial resolution. Secondary electrons are generated in two ways. Firstly, by the primary electrons entering the sample and secondly escaping backscattered electrons. Primary electrons are greater in number and in turn the detection region for secondary electrons origin is larger than the incident beam, of which Fig. 3.13 shows. Smaller sampling volume is a known characteristic of secondary electrons; thus, a better spatial resolution can be expected. The amount of secondary and backscattered electrons emitted from the specimen for each incident electron are known as the secondary electron coefficient  $\delta$  and the backscattered electron coefficient  $\eta$  respectively.  $\eta$  is dependent on the atomic number of the specimen where  $\delta$  is dependent on the accelerating voltage. The total electron yield ( $\eta + \delta$ ) is a complex function of the accelerating voltage. With the maximum found in-between 1-5 keV.

Precise control of the accelerating voltage is needed to produce an electron yield of unity, to overcome any charging that may occur [3.19].

### 3.6.5 *The Scattering of Electrons by Atoms*

Image formation in most electron microscopes are when primary electrons enter the specimen and the same or different electrons leave the specimen and are measured by the detector located in the microscope. The interaction between the atoms of the specimen and the high energy electrons allow for interpretations of the diffraction pattern or the analytical spectrum which each type of electron microscope produces. The probability that a specific electron will be scattered is described in two ways. The first is a cross-section,  $\sigma$ , and the second is a mean free path,  $\lambda$ . Defining the mean free path for scattering, leads to equation 3.3 [3.19].

$$\lambda = 1/N\sigma \quad (3.3)$$

Where  $\lambda$  has the dimension length and is the average distance at which an electron may travel before scattering. And  $N$  is the number of particles per unit volume of the specimen and cross-section for a specific scattering event. Electrons under normal circumstances are scattered only once or not scattered when interacting with a relatively thin specimen. Numerous scattering events are expected when incident electrons pass through a relatively thick specimen. Events of scattering have a probability of an incident electron suffering  $n$  scattering events while traveling distance  $x$  is given by Poisson equation: [3.23]

$$p(n) = \left(\frac{1}{n!}\right) \left(\frac{x}{\lambda}\right)^n \exp\left(\frac{-x}{\lambda}\right) \quad (3.4)$$

### 3.6.6 *The Preparation of Specimen for Examination in the SEM*

Bulk specimens are generally used to study surface morphology in most cases. An advantage of the SEM is there is no lenses below the specimen, resulting in more space available in the vacuum chamber within the microscopy. Which in turn allows for many mechanical adjustments for manipulating the working distance from the probe. Effective viewing and image formation of a specimen in the SEM requires the surface of the said specimen to be electrically conducting. This is due to the statistics of electron yield. In an operating SEM, high energy electrons bombard a specimen. From section 3.7.4, there is a yield of  $\eta$ , backscattered electrons and  $\delta$  secondary electrons. At unity, the cross-over voltages are in the range of 1-5 kV, which is far lower than the normal accelerating voltage of the electron microscope. Due to this difference there is a build-up of electrons on the surface of the specimen. The specimen surface becomes negatively charged up to the point of the incident beam of electrons are repelled from their expected path. Resulting in a distorted image being formed. Clean metal specimens do not have this problem, provided they are earthed correctly. Non-conducting specimens may need to be coated with a thin conducting layer (<10 nm) of carbon or gold usually through sputter coating. Precautionary measures must be taken to ensure that conductive coatings mask detail in higher resolution or interfering with signals from other interaction regions. Degradation by beam heating, damage from radiation and specimen volatility in a high vacuum can lead can influence specimen integrity [3.19].

During this study, the TiO<sub>2</sub> nanowire samples were analysed using a Zeiss Auriga field-emission scanning electron microscope (FEG-SEM) operated at an accelerating voltage of 5kV, using an in-lens secondary electron detector. All samples were analysed without prior coating by carbon or metal. Instead, the as-prepared nanowire surfaces were cleaned for 1 minute in the microscope chamber by means of nitrogen plasma using a Xei Scientific Evactron 25 surface decontaminator, followed by flushing of the system by nitrogen gas for 30 seconds; the plasma cleaning ensures effective removal of hydrocarbons from the sample surface, thereby enhancing the image quality during analysis.



## 3.7 X-Ray Diffraction

### 3.7.1 Introduction

X-rays are electromagnetic radiation with a shorter wavelength as compared to visible light. This type of electromagnetic radiation is produced when a speeding electron is slowed down significantly. When traveling wave interfere with a structure with a repeated distance that is the same as the incident wavelength a phenomenon known as diffraction occurs. During this interaction, incoming wave-fronts from the said structure produce constructive and destructive interference patterns. X-rays have about the wave-length range of inter-atomic spacing found in 3-dimensional crystal structure that serves as a scattering centre for the incoming wave fronts. This scattering by each atom in the crystalline structure is known as the x-ray diffraction (XRD) phenomenon. Which is used for the study of the atomic crystalline structure of specimens. In this study, XRD will be used to investigate the inter-layer spacing in TiO<sub>2</sub> NWs, the identification of the various phases in the deposited material and the degree of crystallinity and impurities.

### 3.7.2 Crystal Structure and Bravais Lattices

Materials can be differentiated structurally by the arrangement of atoms. Amorphous materials have atoms that are randomly distributed, while crystalline materials have atoms arranged in a periodic manner in three dimensions. Fig. 3.15 shows the atomic arrangement within a crystal, with the atoms imaged as points within a fixed relation to space and each having identical neighbours.

Three vectors can be drawn from a lattice point to generate a point lattice unit cell. These vectors can be described in terms of lengths:  $a$ ,  $b$  and  $c$ , and the angles between them:  $\alpha$ ,  $\beta$ ,  $\gamma$ . The lengths and angles are known collectively as the lattice constants and are shown in Fig. 3.18. The vectors are also known as crystallographic axes and define the point lattice through repeated vector generation. Fourteen different point lattices can be generated from the relation between the different lattice parameters, which are known as the Bravais lattices and shown in Table 3.2

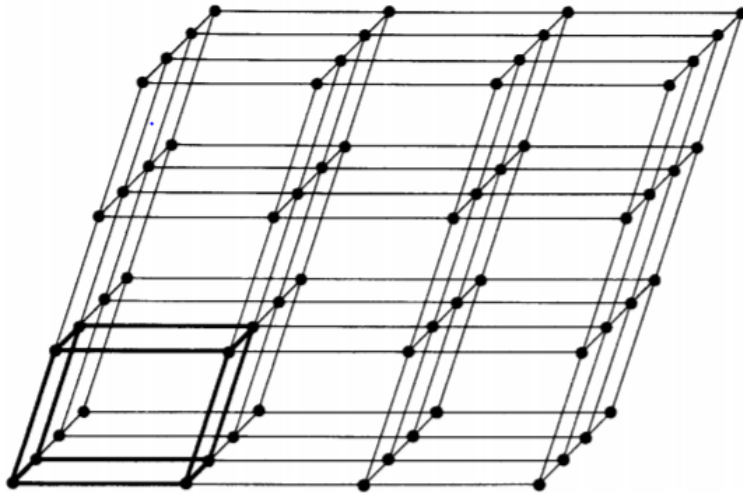


**Fig 3.15:** Simple schematic of a point lattice in 3 dimensions [3.20]

The direction of a vector within the Bravais lattice is given as a linear combination of three crystallographic axes as:

$$x = u\vec{a} + v\vec{b} + w\vec{c} \quad (3.5)$$

where  $\vec{a}$ ,  $\vec{b}$ ,  $\vec{c}$  are any vector in the Bravais lattice. And  $u$ ,  $v$ ,  $w$  are coordinates of any point on the vector. Equation (3.5) can be written as  $[u \ v \ w]$  as shown in Fig. 3.16. Directions related by symmetry are represented by angular brackets. An example of this would be the four body diagonals of a cube  $[111]$ ,  $[-111]$ ,  $[1-11]$  and  $[11-1]$  which are represented by  $\langle 111 \rangle$  where negative directions are included. This collective of vectors form the reciprocal space of the lattice. A lattice plane is defined as any plane containing at least three non-colinear lattice points for any Bravais lattice. A set of parallel planes is also known as a family of lattice planes and together contain all the points of the 3d Bravais lattice. Cubic systems have an intrinsic relationship between the family of lattice planes and the vectors of the reciprocal lattice. This relation allows for easier identification of the orientation of the lattice planes in space.

**Table 3.2:** Simplified description of the fourteen Bravais lattices [3.20]

System	Axial lengths and angles	TiO <sub>2</sub> 100W	TiO <sub>2</sub> 300W
Cubic	Three equal axes at right angles $a = b = c, \alpha = \beta = \gamma = 90^\circ$	Simple	P
		Body-centred	I
		Face-centred	F
Tetragonal	Three equal axes at right angles, two angles equal $a = b \neq c, \alpha = \beta = \gamma = 90^\circ$	Simple Body-centred	P I
Orthorhombic	Three unequal axes at right angles $a \neq b \neq c, \alpha = \beta = \gamma = 90^\circ$	Simple	P
		Body-centred	I
		Base-centred	C
		Face-centred	F
Rhombohedral	Three equal axes, equally inclined $a = b = c, \alpha = \beta = \gamma \neq 90^\circ$	Simple	R
Hexagonal	Two equal co-planar axes at $120^\circ$ , third axes at right angles $a = b \neq c, \alpha = \beta = 90^\circ, \gamma = 120^\circ$	Simple	P
Monolithic	Three unequal axes, one pair not at right angles $a \neq b \neq c, \alpha = \gamma = 90^\circ \neq \beta$	Simple	P
		Base-centred	C
Triclinic	Three unequal axes, unequally inclined and none at right angles $a \neq b \neq c, \alpha \neq \beta \neq \gamma \neq 90^\circ$	Simple	P

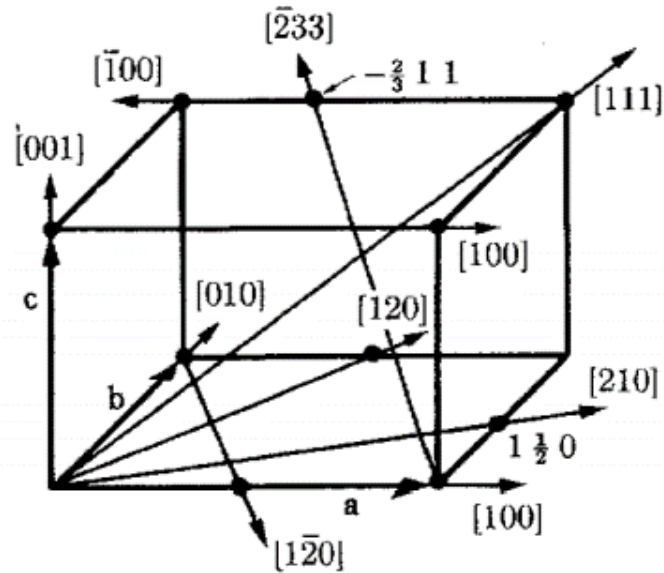


**Fig. 3.16:** Indices for directions of a general unit cell, with the diagonal indices included [3.20]

For generalised cubic systems, Miller indices,  $h k l$ , contained in round brackets  $(h k l)$  denote the orientation of a plane, given by the vector normal to it. Lattice planes are similar to lattice vectors in that through symmetry, planes of a form are denoted by  $\{h k l\}$ .

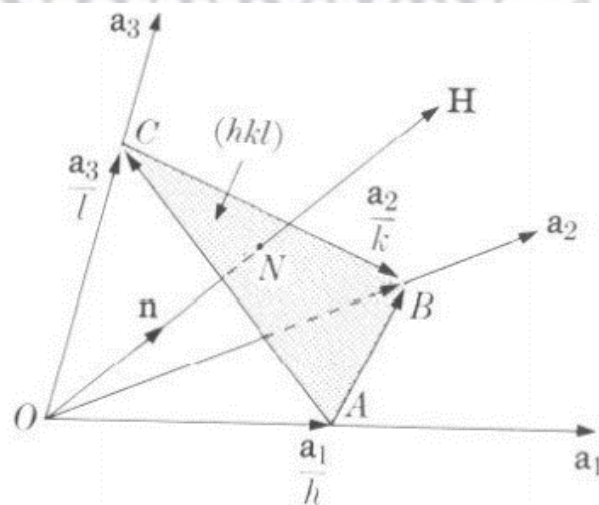


**Fig. 3.17:** Relationship between the reciprocal lattice vector and the crystal plane  $(hkl)$  [3.20]

### 3.7.3 Bragg's Law for Diffraction

Fig. 3.18 shows a monochromatic beam of x-rays parallel to each other, denoted as O and O'. These two parallel beams strike a stack of planes (h k l) spaced a distance d away from each other at an angle  $\theta$ . Each plane is able to scatter the incident radiation and consist of equally spaced atoms. Resulting from the incident interaction beam with the atoms of the parallel planes are scattered rays P and P'. These scattered rays will re-combine to form a diffracted beam if their path difference is an integer multiple of wavelengths, therefore:

$$CA + AD = d\sin\theta + d\sin\theta = n\lambda$$

Which then can be simplified into:

$$2d\sin\theta = n\lambda \quad (3.6)$$

Where n = the integer multiple (order of diffraction),  $\lambda$  = wavelength of radiation, d = interplanar spacing and  $\theta$  is the incident angle (Bragg angle). Equation (3.6) is known as Bragg's law and gives the angle  $\theta$  for the set of planes (h k l) of spacing d, reflects x-rays of the wavelength  $\lambda$  for the n<sup>th</sup> order.

UNIVERSITY of the  
WESTERN CAPE



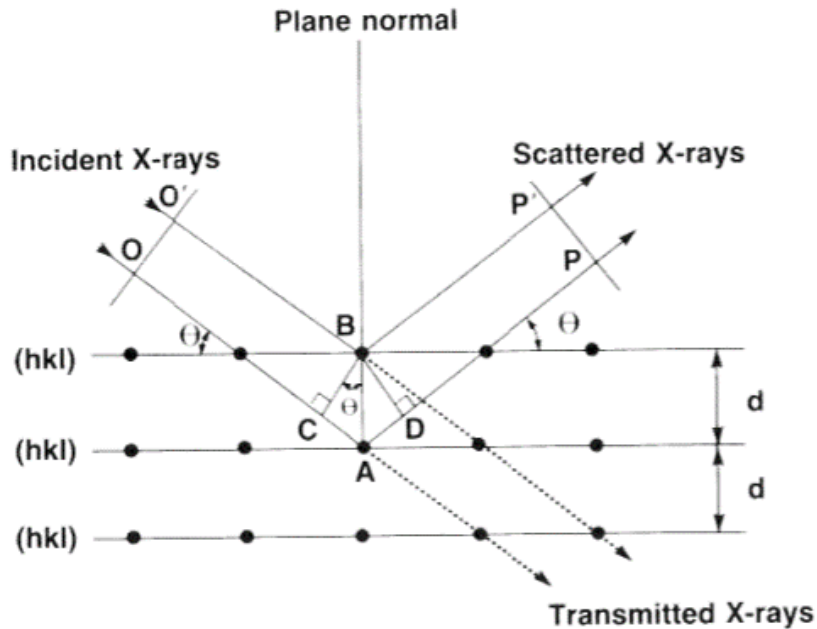


**Fig. 3.18:** Conditions for Bragg's Law shown for the interaction of x-rays with the normal plane [3.20]

### 3.7.4 Instrumentation

An x-ray diffractometer shown in Fig. 3.20 consists of three fundamental parts. An x-ray source, the diffractometer circle and a detector system. X-rays diverge from the source at S and are diffracted by the specimen at C to form a convergent diffracted beam, which focuses at the slit F before entering the detector at G. The carriage at G is locked in a  $\theta$  to  $2\theta$  relation. A and B are special slits that define and collimate the incident and diffracted beams. A filter is placed in the diffracted beam-path to suppress the  $K_{\beta}$  radiation and then to decrease the background radiation, radiating off the specimen.

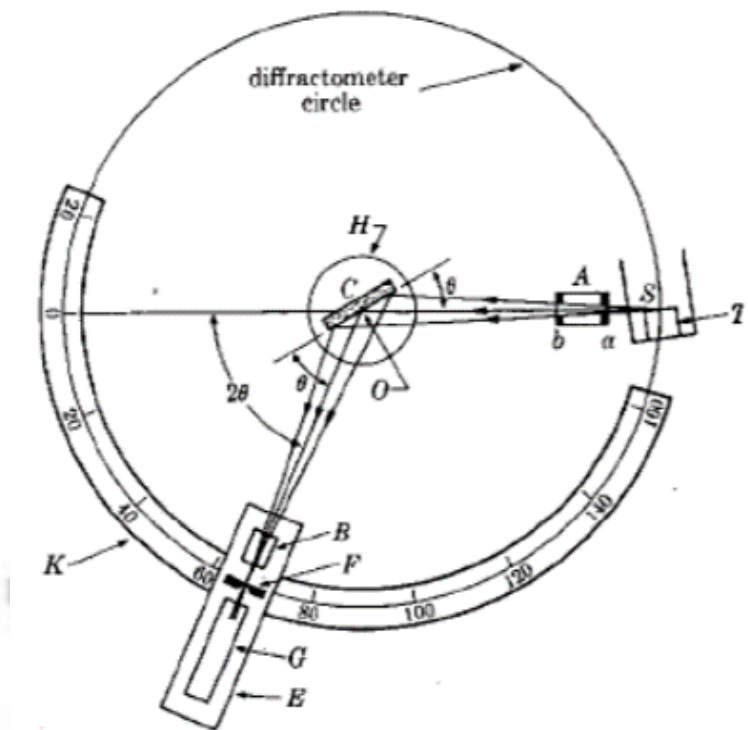


**Fig. 3.19:** Schematic of a conventional X-ray diffractometer [3.20]

### 3.7.5 Grazing-Incidence X-ray Diffraction

Conventional symmetrical Bragg configurations of  $\theta$  to  $2\theta$  range generally produce weak signals from the film/nanowire array itself and strong signals from the substrate. Depth of analysis also varies greatly during the  $\theta$  to  $2\theta$  range. For this case, usage of the technique of X-ray diffraction at a grazing incidence to minimize the contribution related to the substrate is preferred. For this geometry, the incidence angle is fixed at a small angle and the angle between the incident beam and diffracted beam is varied. Therefore, the incident beam interacts with the surface of interest to strengthen the resulting diffraction pattern, while the signal from the substrate is greatly reduced to the angle of incidence. Under these conditions, the depth of analysis for a small incidence angle is not dependent on the  $2\theta$  angle. Which in turn means that the depth of analysis is controlled by the angle of incidence and does not vary during the symmetrical sweeping. With grazing incidence, crystal planes inclined to the surface of the specimen are observed.

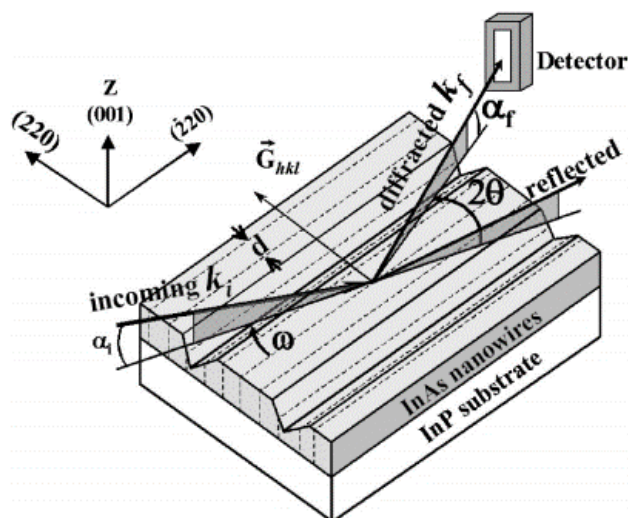


**Fig. 3.20:** Schematic of GIXRD geometry on InAs nanowires grown on an InP substrate [3.21]

### 3.7.6 Characterisation

GIXRD is a technique used to obtain information on the interlayer spacing in TiO<sub>2</sub> NWs and the impurities of N-Doped TiO<sub>2</sub> NWs. Crystallite size, lattice constants and lattice strain can also be determined. Fig. 3.21 shows a typical GIXRD spectrum of hydrothermally grown TiO<sub>2</sub> NWs. The characteristic peaks can easily identify impurities. A measure of the interlayer spacing of the NWs can be obtained from the peak's position and using Bragg's Law.

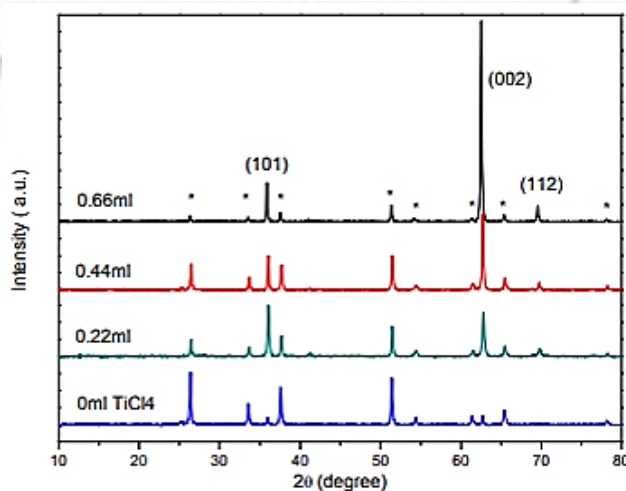


**Fig. 3.21:** XRD spectra of TiO<sub>2</sub> NWs grown at different concentrations [3.22]

During analysis, GIXRD data were recorded with a PAN-alytical Empyrean diffractometer using  $\text{CuK}_\alpha$  radiation ( $\lambda=1.5406 \text{ \AA}$ ) as X-ray source. The instrument was operated at a source voltage and current of 45 kV and 40 mA, respectively, while the incident X-ray beam was kept at 0.4 degrees with respect to the substrate, scanning a Bragg angle ( $2\theta$ ) range from 10 to 90 degrees (0.02 degrees step size at 2 s per step). The incident beam optics consist of a parabolic mirror, 4 mm mask, 1/16 divergence and 0.04 rad Soller slit, whereas the diffracted beam optics consist of a parallel plate collimator slit, 0.04 Soller collected by a PIXcel3D 55  $\mu\text{m}^2$  (256 $\times$ 256 pixels) X-ray detector. Instrument broadening and peak position calibration were corrected using a large area lanthanum hexaboride ( $\text{LaB}_6$ ) standard.

## 3.8 X-Ray Photoelectron Spectroscopy

### 3.8.1 Introduction

Monochromatic x-rays or ultraviolet light are mostly used for the excitation of photo-electrons whose energy characteristically has information regarding the binding energy within its originating atom. This binding energy gives information of the nature of the atom in the specimen. Characteristic kinetic energy is given off by the energy of the x-ray photon by the photoelectron. Resulting in the complete absorption during the process, with the characteristic binding energy being subtracted of the electron, as it is emitted. This technique is known as X-ray photo-electron spectroscopy. These photoelectrons carry specific information that corresponds to the top atomic layers. This is due to photoelectrons only escaping from the near specimen surface.

### 3.8.2 Principles of XPS

XPS uses monoenergetic soft x-rays to analyse the energy of detected electrons for surface analysis.  $\text{Mg K}_\alpha$  (1253.6 eV) x-rays are commonly used. With limited penetrating power, these photons only interact with atoms of the surface region, resulting in electrons to be emitted by the photoelectric effect. With the emitted electrons defined with kinetic energies of:

$$KE = h\nu - BE - \phi_s \quad (3.7)$$

Where  $h\nu$  is the energy of the photon,  $BE$  is the binding energy of the atomic orbital from which the electron originates, and  $\phi_s$  is the spectrometer work function. The energy difference between the initial and final states after the photoelectron is emitted is defined as the binding energy. The final states of the ions from each type of atom may vary, which in turn can lead to varying kinetic energies for the emitted electrons. Relative binding energies and ionisation cross-sections for an atom are shown in Fig. 3.22. With the Fermi level corresponding to zero binding energy and the depth below the Fermi level in the figure indicates the binding energy after the electron is emitted.

The line lengths indicate relative probabilities of the various ionisation processes. The p, d and f levels become split upon this ionisation, leading to vacancies in the  $p_{1/2}$ ,  $p_{3/2}$ ,  $d_{3/2}$ ,  $d_{5/2}$ ,  $f_{5/2}$ ,  $f_{7/2}$ . Due to each element having characteristic binding energies, XPS can be used for identification and determination of the concentration of elements in the surface. Varying of elemental binding energies or chemical shifts result from the relative differences in the chemical potential and polarisability of compounds. Chemical shifts of this nature can be used to characterise the chemical state of the analysed material. Auger electrons may be emitted along with photoelectrons due to the relaxation of the excited atoms remaining after photoemission.

For the Auger process, an outer electron falls into the inner orbital vacancy, with a second electron then simultaneously emitted. This emitted electron carries off the excess energy. Kinetic energy equal to the difference between the energy of the initial ion and the double-charged final ion is possessed by the Auger electron. Which in turn is independent of the mode of initial ionisation. Leading to the two emitted electrons. The probability of electron interaction with material is far greater than those of photons. Which is seen by the path length of photons being on the order of micro-meters ( $\mu\text{m}$ ) and the path length of electrons being on the order of angstroms ( $\text{\AA}$ ). Ionisation therefore, occurs to a specimen depth of a few  $\mu\text{m}$ , only electron which origin is that of angstroms below the surface of the specimen can be emitted from the surface without energy loss. Inelastic electron loss processes in turn produce the peaks in the spectra and are the used to gather information about the specimen.



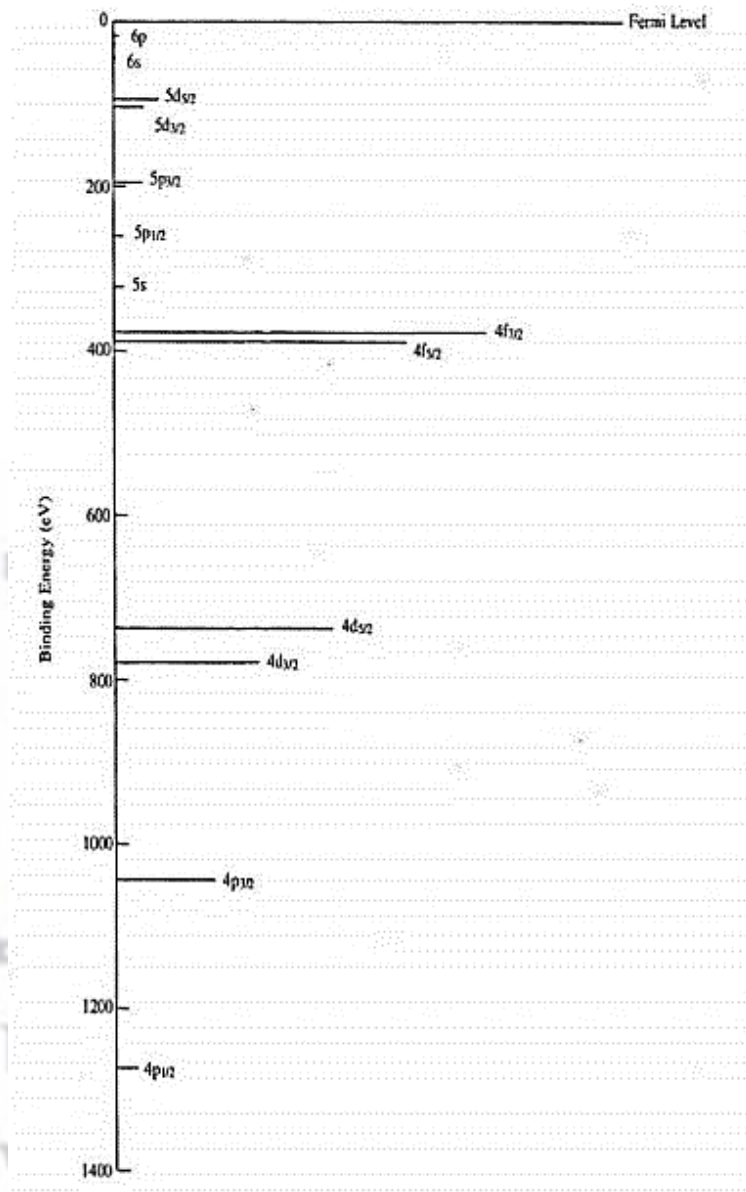


**Fig. 3.22:** Relative binding energies for an atom [3.23]

Electrons leaving the specimen are detected through their kinetic energy. The analyser for detection is conventionally operated as a fixed energy window to maintain a constant energy resolution and to only have those electrons with energy within the specific window's range. Detected electrons are modified to the pass energy before entering the analyser, with the retardation voltage being varied as it may be needed within the range of zero to the photon energy.

Each electron detected is a discrete event, with the number, time and energy for each electron measured separately.

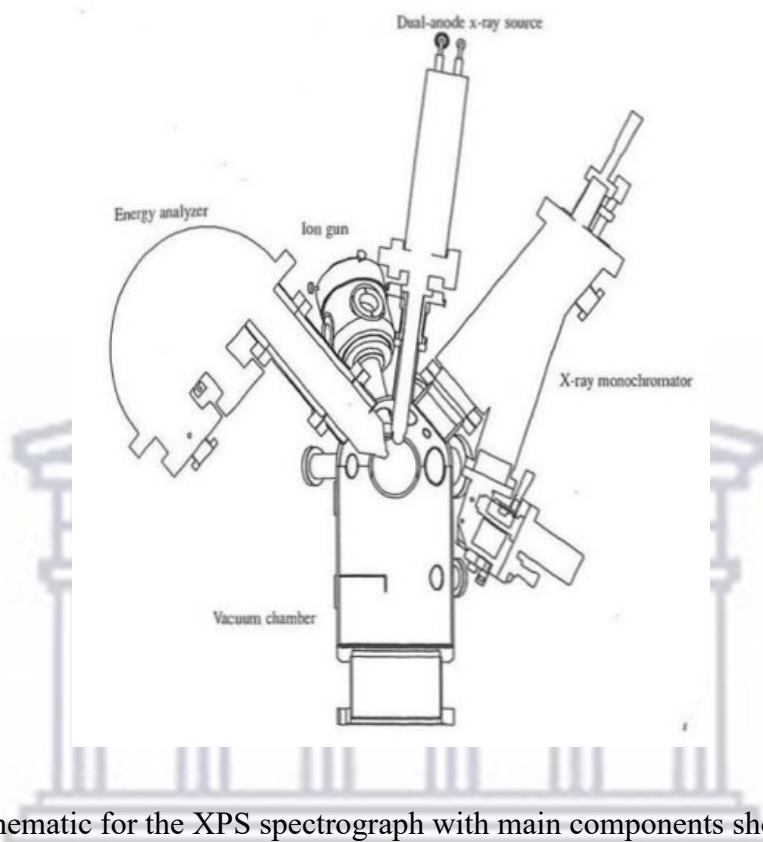


**Fig 3.23:** Schematic for the XPS spectrograph with main components shown [3.23]

### 3.8.3 Preparing and Mounting Samples

Modern XPS system applications have trivial sample preparation and mounting and therefore are not critical. Mechanical attachment to the mounting block is straightforward and analysis is started with the sample unchanged. Further sample preparation may change the surface composition and is thus not recommended. In certain circumstances where sample preparation is needed, volatile material is then removed from the sample in a vacuum system or by cleaning with a suited solvent. Care is to be taken in using distilled solvents to avoid any contamination with impurities.

### 3.8.4 Experimental Setup

Fig 3.23 shows the relation of the major components of the XPS system. This includes the electron energy analyser, the x-ray source and the ion gun used. The monochromatic x-ray source is perpendicular to the analyser and the standardised x-ray source is located at  $54.7^\circ$  relative to the analyser axis. XPS spectrums are displayed as a plot of the number of electrons versus electron binding energy in a fixed energy interval. Most noise in the spectrum is not due to the instrumentation but as a consequence of the collection of single electrons as counts randomly spaced in time. Various types of peaks are observed in XPS spectra. Fundamental peaks that are always observed persist throughout the use of the XPS technique. Instrumental effects can induce spectral features within the spectra. Commonly present lines in the XPS spectrum are usually the first to be identified, such as Carbon (C) and Oxygen (O). After that the major lines and the associated weaker lines are identified. Most modern XPS systems have software that have peak identification and poor signal-to-noise of data may require manual identification for some peaks.

The accuracy of line energies determines the identification of chemical states. To determine these line energies the voltage scale of instrument must be calibrated correctly. Importantly, the ability of the XPS technique to extract information of the chemical states of the changes in the binding energy of the photoelectron lines. XPS standards are used to calculate the chemical shifts and binding energies. The XPS technique also studies the relative concentrations of the various constituents of the specimen. Developed methods use peak area sensitivity factors which is known to be more accurate. This is useful for obtaining accurate qualitative data. In this study XPS were used to study the electronic structure of the Ti 2p, O 1s and N 1s line-shapes of the as-synthesised and plasma exposed TiO<sub>2</sub> nanowire arrays. The spectra were collected with a Thermo ESCAlab250Xi spectrometer. Monochromatic aluminium K<sub>α</sub> X-rays (1486.7 eV) of a probe spot size of 900 μm and high-resolution spectral energy resolution of 20 eV were used as source.

### 3.9 Ultraviolet-Visible Spectroscopy for Transmission

#### 3.9.1 Introduction

The analysis of light can be used for characterisation and quantitative determination of substances. UV-Vis spectroscopy is a known technique that originates from the absorption of light by specimens. Samples are illuminated with varied wavelengths in the visible, lower infrared and ultraviolet regions of the electromagnetic spectrum. The amount of light absorbed depends on the material of the specimen. What light remains is measured as a function of wavelength by the detector and known as transmitted light. Due to each different material absorbing light in a different way, a UV-Vis spectrum reveals fundamental properties for identification of quantification.

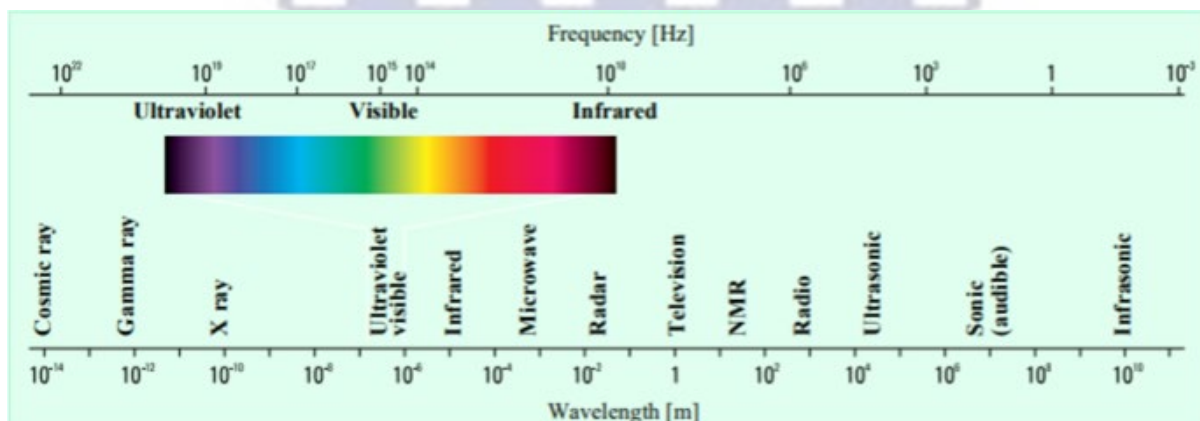


Fig. 3.24: Illustration for the electromagnetic spectrum [3.24]

#### 3.9.2 Principles of UV-Vis Spectroscopy

Incident radiation ( $I_0$ ) refers to light entering the sample, transmitted radiation ( $I$ ) is the amount of light that leaves the sample. The amount of light absorbed is the difference between the transmitted and incident radiation. Light may also be partially reflected from the sample. The amount of light absorbed is measured as either absorbance or transmittance. Transmittance is generally defined as a percentage or a fraction of 1.

$$\%T = \left(\frac{I}{I_0}\right) \times 100 \quad \text{or} \quad T = I/I_0 \quad (3.8)$$

Absorbance is then defined as:

$$A = -\log T \quad (3.9)$$

### 3.9.3 Experimental Setup

A spectrophotometer is an instrument for measuring the transmittance or absorbance of a sample as a function of the wavelength of electromagnetic radiation. The main components are: A source for generation of electromagnetic radiation, A dispersion device that selects from the broadband radiation for a specific wavelength, the specimen or specimen area, at least one detector for the measurement of the intensity of radiation. As seen in Fig. 3.25, a basic schematic shows the general components of most modern spectrophotometers.

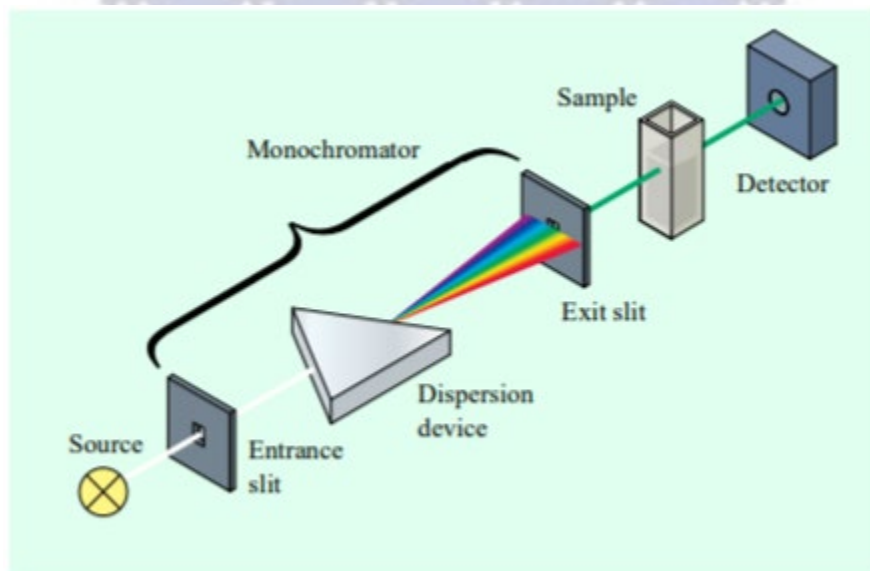


**Fig. 3.25:** Schematic of a conventional spectrophotometer system [3.24]

### 3.9.4 Characterisation

Characterisation of bulk specimens for transmission spectra show the amount of light passing through the sample that is not absorbed, reflected or scattered within the sample. Important



information that can be derived from these spectra can be used qualitatively to determine what optical properties the sample might have. Furthermore, investigations into the controlled growth and changes to the absorbance and transmission spectra for active layers for photovoltaics can be verified. Fig. 3.26 shows an example of the transmission spectra for the 200–900 nm wavelength range for the undoped TiO<sub>2</sub> thin films grown at different Ar/O<sub>2</sub> ratios.

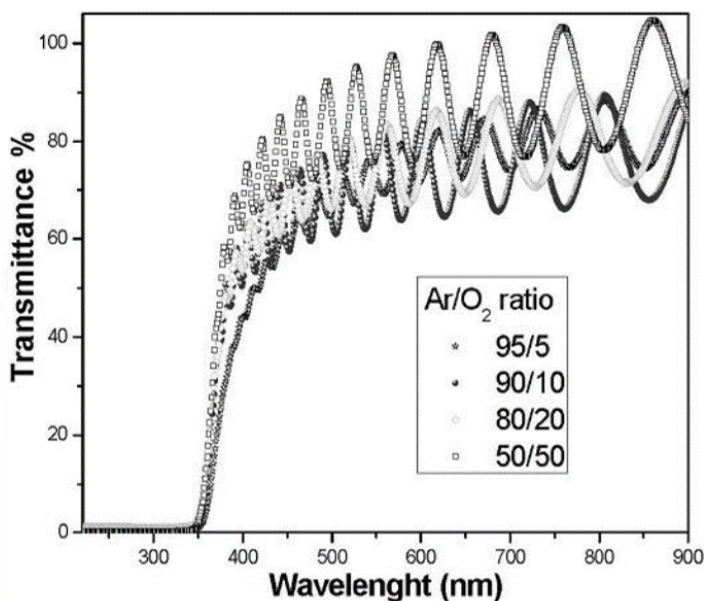


**Fig 3.26:** Transmission spectra for TiO<sub>2</sub> thin films grown at different Ar/O<sub>2</sub> ratios [3.25]

In this study UV-Vis spectra were used to study the amount of transmittance of light through as-synthesised and plasma exposed TiO<sub>2</sub> nanowire arrays. The spectra were collected with a Semiconsoft MProbe Thin Film measurement spectrometer. With a fibre optic probe of size of 3 mm, Two spectrometer channels/ detectors (F4 Si 3600 pixels CCD and InGaAs 512)/ ADC - 16-bit, Deuterium/ Tungsten-Halogen light source for UV and visible signals. A thickness range of 1 nm to 200  $\mu$ m.

## References

- [3.1] K. Byrappa, M. Yoshimura “*Handbook of hydrothermal technology a technology for crystal growth and materials processing*”, William-Andrew Publishing, New Jersey, (2001) 1-3
- [3.2] E. Poniatowski, H. Rodriguez-Talavera, R. Heredia, M.de la C, O. Canocorona, R. Arroyo-Murillo, “*Crystallisation of nanosized titania particles prepared by the sol-gel process*”, J. Mat. Res. 9 (1994) 2101
- [3.3] W. Lee, Y. Gao, K. Dwight, A. Wold, “*Preparation and characterisation of titanium (IV) oxide photocatalysts*”, Mat. Res. Bull. 27 (1992) 685
- [3.4] Q. Chen, Y. Qian, Z. Chen, G. Zhou, Y. Zhang, “*Preparation of TiO<sub>2</sub> powders with different morphologies by an oxidation hydrothermal combination method*”, Mater. Letts. 22 (1995) 77
- [3.5] Y. Qian, Q. Chen, Z. Chen, C. Fan, G. Zhou, “*Preparation of ultrafine powders of TiO<sub>2</sub> by hydrothermal H<sub>2</sub>O<sub>2</sub> oxidation starting from metallic Ti*”, J. Mat. Chem. 3 (1993) 203
- [3.6] Z. Zhang, C. Wang, R. Zakaria, J. Ying, “*Role of particle size in nanocrystalline TiO<sub>2</sub>-based photocatalysts*”, J. Phys. Chem. 102 (1998) 10871
- [3.7] W. Li, C. Ni, H. Lin, C. Huang, S. Shah, “*Size dependence of thermal stability of TiO<sub>2</sub> nanoparticles*”, J Appl. Phys. 96 (2004) 6663
- [3.8] D. Bavykin, V. Parmon, A. Lapkin, F. Walsh, “*The effect of hydrothermal conditions on the mesoporous structure of TiO<sub>2</sub> nanotubes*”, J. Mat. Chem. 14 (2004) 3370
- [3.9] Y. Suzuki, S. Yoshikawa, “*Synthesis and thermal analyses of TiO<sub>2</sub>-derived nanotubes prepared by the hydrothermal method*”, J. Mat. Res. 19 (2004) 982
- [3.10] H. Cheng, J. Ma, Z. Zhao, L. Qi, “*Hydrothermal preparation of uniform nanosize rutile and anatase particles*”, Chem. Mat. 7 (1995) 663
- [3.11] R. Yoshida, Y. Suzuki, S. Yoshikawa, “*Syntheses of TiO<sub>2</sub> (B) nanowires and TiO<sub>2</sub> anatase nanowires by hydrothermal and post-heat treatments*”, J. Solid State Chem. 178 (2005) 2179
- [3.12] Y. Zhang, G. Li, Y. Jin, Y. Zhang, J. Zhang, L. Zhang, “*Hydrothermal synthesis and photoluminescence of TiO<sub>2</sub> nanowires*”, Chem. Phys. Lett. 365 (2002) 300

- [3.13] X. Feng, K. Shankar, O. Varghese, M. Paulose, T. Latempa and C. Grimes, “*Vertically aligned single crystal TiO<sub>2</sub> nanowire arrays grown directly on transparent conducting oxide coated glass: synthesis details and applications*”, *Nano Lett.* 8 (2008) 3781
- [3.14] B. Liu, E. Aydil, “*Growth of oriented single-crystalline rutile TiO<sub>2</sub> nanorods on transparent conducting substrates for dye-sensitised solar cells*”, *J. Am. Chem. Soc.* 131 (2009) 3985
- [3.15] X. Feng, J. Zhai, L. Jiang, “*The fabrication and switchable superhydrophobicity of TiO<sub>2</sub> nanorod films*”, *Ang. Chem. Int. Edit.* 44 (2005) 5115
- [3.16] E. Liston, “*Plasma treatment for improved bonding: a review*”, *J. Adhesion* 30 (1989) 199
- [3.17] A. Ghicov, J. Macak, H. Tsuchiya, J. Kunze, V. Haeublein, L. Frey, P. Schmuki, “*Ion implantation and annealing for an efficient N-doping of TiO<sub>2</sub> nanotubes*” *Nano. Lett.* 6 (2006) 1080
- [3.18] C. Chen, H. Bai, S. Chang, C. Chang, W. Den, “*Preparation of n-doped TiO<sub>2</sub> photocatalyst by atmospheric pressure plasma process for VOCs decomposition under UV and visible light sources*” *J. Nano. Res.* 9 (2007) 365
- [3.19] P. Goodhew “*Electron microscopy and analysis*”, Taylor and Francis, London 3 (2001) 8-14, 24, 29-30, 122-127, 135, 162-164
- [3.20] B. Cullity, “*Elements of X-ray diffraction*”, Addison-Wesley Publishing Company, Reading 2 (1978) 33-36, 42-43, 84-87
- [3.21] R. Magalhães-Paniago, H. Gutiérrez, R. Bortoleto, M. Cotta Cita, “*Three-dimensional mapping of the strain anisotropy in self-assembled quantum-wires by grazing incidence x-ray diffraction*”, *Appl. Phys. Lett.* 85 (2004) 3581
- [3.22] S. Jinzhan, G. Leijin, “*High aspect ratio TiO<sub>2</sub> nanowires tailored in concentrated HCl hydrothermal condition for photoelectrochemical water splitting*”, *RSC Adv.* 5 (2015) 53012
- [3.27] J. Moulder, W. Stickle, P. Sobol, K. Bomben, “*Handbook of X-ray photoelectron spectroscopy*”, Perkin-Elmer Corporation, Prairie 1 (1992) 9-10, 15
- [3.28] T. Owen, “*Fundamentals of UV-visible spectroscopy*”, Agilent Technologies, Germany 1 (2000) 10, 14, 38, 45

- [3.29] A. Franco, G. Zambrano, M. Gómez, E. Camps, L. Escobar-Alarcón, “*Photocatalytic activity of nitrogen-doped and undoped titanium dioxide sputtered thin films*”, *Superf. Vacío*. 25 (2012) 161



## Chapter 4: Results and Discussion

---

This chapter summarises the morphological, structural, chemical bonding and doping characteristics, as well as the optical behaviour of the plasma-irradiated TiO<sub>2</sub> nanowire arrays synthesised under the experimental conditions discussed in Chapter 3. The data and analyses are done by means of SEM, GIXRD, XPS and UV-Vis spectroscopy.

### 4.1 Hydrothermal Growth of TiO<sub>2</sub> Nanowires on an FTO Substrate

Fig. 4.1 shows the side-view SEM micrograph of an as-synthesised, non-plasma exposed TiO<sub>2</sub> NW array on an FTO substrate. From the insets of Fig. 4.1 individual “nano-fingers” comprising individual nanowires can be observed, as well as the nanowire coverage on the substrate. A nanowire length of 690 nm and diameter of 67.9 nm are obtained after 3 hours of growth at the conditions discussed in Chapter 3.

The nanowires can be grown directly on the FTO substrates due to the compatible nature of the SnO<sub>2</sub> and TiO<sub>2</sub> crystal lattices, both being tetragonal in nature and having a very small lattice mismatch. The growth of TiO<sub>2</sub> nanowires is discussed by Wisnet *et al* [4.1], who states that individual nano-fingers are formed by V-shaped defect cascades, which originate from the nanowire bottom, run along the [001] growth direction and terminate into the finger-like sub-wires at the tip of the structure. These bunched nano-fingers, which are compacted into the block-like nanowire structure, can be seen in the inset SEM micrograph of Fig. 4.1.



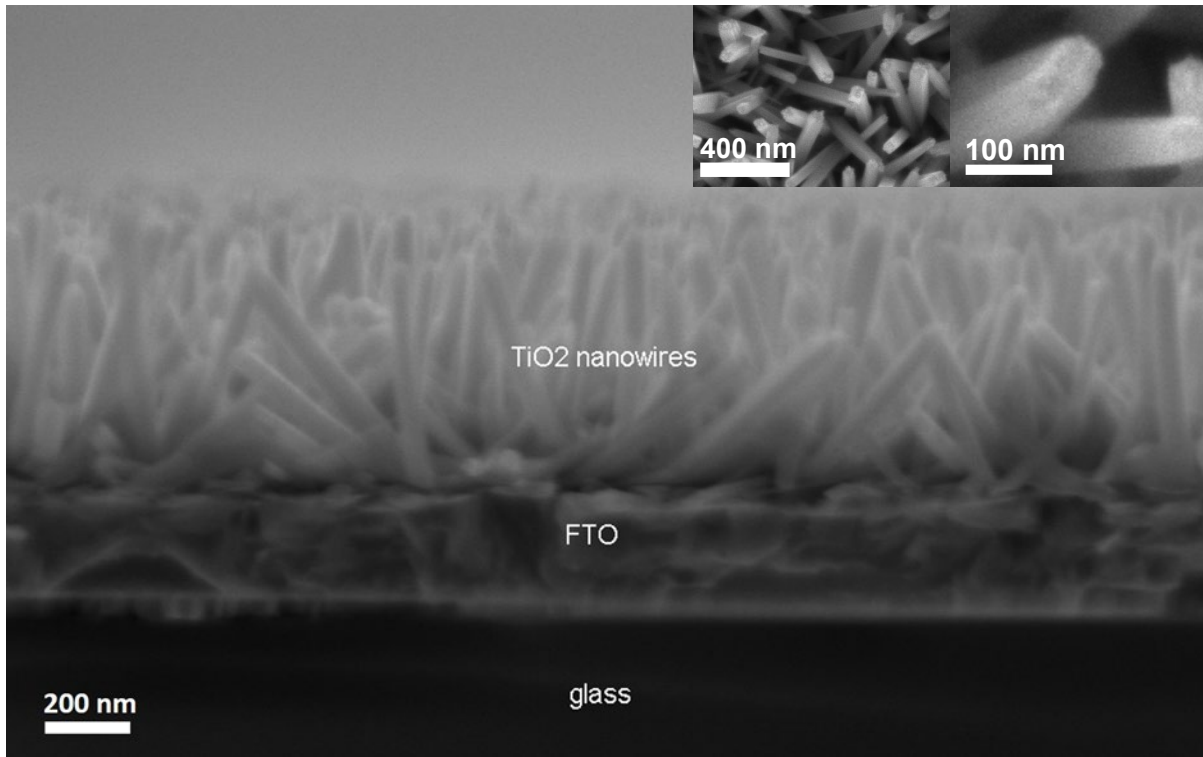


**Fig. 4.1:** SEM micrograph of the as-synthesised nanowire array on the FTO substrate. The inset in the top-right corner shows the top-view and a high-resolution micrograph of the nanowire structure, in which individual nano-fingers, as discussed by Wisnet et al [4.1], can be observed

The TEM micrograph of Fig. 4.2 shows an individual, as-synthesised nanowire, with the inset once more highlighting the individual fingers comprising a single nanowire. As shown, one finger is approximately 10 nm in diameter and span the entire length of the nanowire. The high-resolution micrograph in the top-right hand of Fig. 4.2 shows that the nano-fingers grow along the [101] direction along the length of the nanowire, in accordance with the proposed growth model.

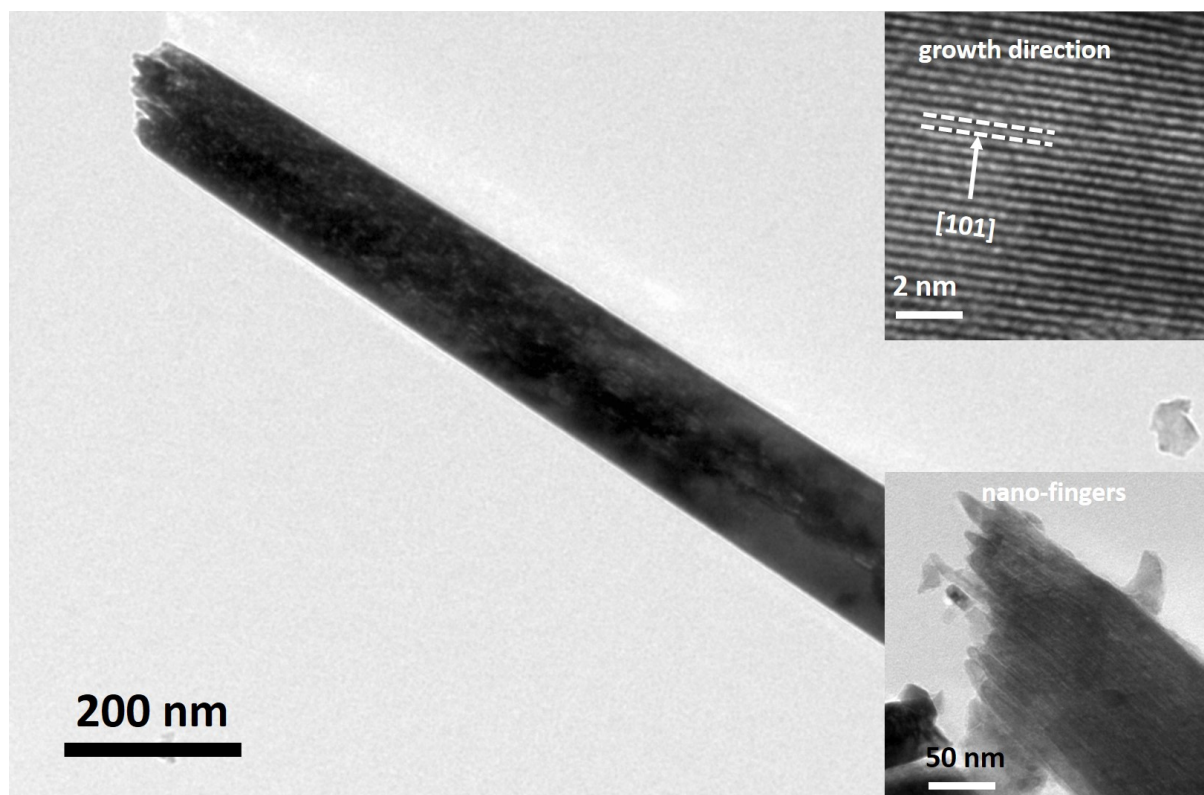


**Fig. 4.2:** TEM micrograph of an individual TiO<sub>2</sub> nanowire grown for 3 hours at 150 °C in a hydrothermal solution consisting of 2 ml HCL, 10 ml of H<sub>2</sub>O and 0.25 ml TBT (top-right) high-resolution micrograph indicating the growth direction of an individual nanowire; (bottom-right) zoomed-in micrograph highlighting the nano-fingers

#### 4.2. Effect of Nitrogen Plasma Power on the Morphological, Structural and Optical Properties of Individual TiO<sub>2</sub> Nanowires

The effects increasing the plasma power during irradiation on the above-mentioned properties are investigated in this section. For all samples, the time of exposure and substrate temperature are kept constant at 10 mins and room temperature, respectively. During a typical experiment, a base pressure of  $1.2 \times 10^{-5}$  mbar is maintained, prior to feeding an Ar and N<sub>2</sub> gas mixture into the chamber at a flow-rate of 100 sccm each, ultimately reaching a desired chamber vacuum of  $5.0 \times 10^{-2}$  mbar. At this point, the plasma is ignited and slowly ramped to the desired value. As soon as

the power is stabilised at the desired value, the Ar flow-rate is reduced to 0 sccm. This point signals the start of the irradiation process; plasma powers of 100, 300 and 500W are compared.

#### 4.2.1 *TiO<sub>2</sub> Nanowire Morphology*

Fig. 4.3 compares micrographs of the top-view and cross-sectional view of the as-grown nanowire array to that of plasma-exposed NWs at various plasma power. The top-row of Fig. 4.3 shows micrographs (a) before and (a') after exposure to 100W N<sub>2</sub> plasma for 10 minutes at room temperature; (a'') shows cross-section of the nanowires post-exposure in which it can be observed that the vertical-alignment of the nanowires become distorted. Similarly, the second row compares the nanowires (b) before and (b') after exposure to 300 W plasma with (b'') again demonstrating the effect on the alignment of the nanowire array. The bottom row compares the nanowires (c) before and (c') after exposure to 500 W of radiation. Interestingly, at this exposure the distortion in the nanowire alignment is much more pronounced compared to the 100 W irradiated sample. This increasingly obvious distortion of the of the nanowire array alignment is ascribed to the weakening of the weak Van Der Waals electrostatic force, responsible for the alignment of the nanowires [4.2]. The initial exposure of the nanowire array to the Ar plasma (prior to the ignition of the N<sub>2</sub> plasma) is known to etch the surface of the nanowires, and may well be the primary plasma species responsible distortion observed in Fig. 4.3.

The TiO<sub>2</sub> NWs are tetragonal in nature, having square top facets, which follows the known growth model for tetragonal TiO<sub>2</sub> crystal structures [4.3], with the untreated sample at 100W being relatively thin wires, with an average diameter of 62.7 nm. As shown in Fig. 4.3 (a') and from Table 4.1, relatively thicker wires can be observed post-plasma treatment, with the wires observed in Fig 4.3 (a') having an average diameter of 123.81 nm. The average nanowire length exceeds 1 μm, as measured from Fig 4.3 (a''). Similar trends of increasing nanowire diameter sizes are seen for the 300W treatment and the 500W treatment, and are summarised in Table 4.1. A point of note must be made to include the error in measurement in the establishment of the perpendicular component in the SEM micrographs as well as any three-dimensional non-alignment that occurs towards the FTO substrate. The increasing diameter trend may be due to plasma exposure, whereas a decrease in the areal density (i.e. number of NWs per unit area) as seen in the plan-view SEM

images. This is as a result of the dissociation of the electrostatic Van der Waals forces bundling apices of nanowires, as previously discussed. The non-aligned NW arrays post N<sub>2</sub> treatment may be advantageous and can improve the electron–hole dissociation interface during device operation of organic-photovoltaics [4.3, 4.4].

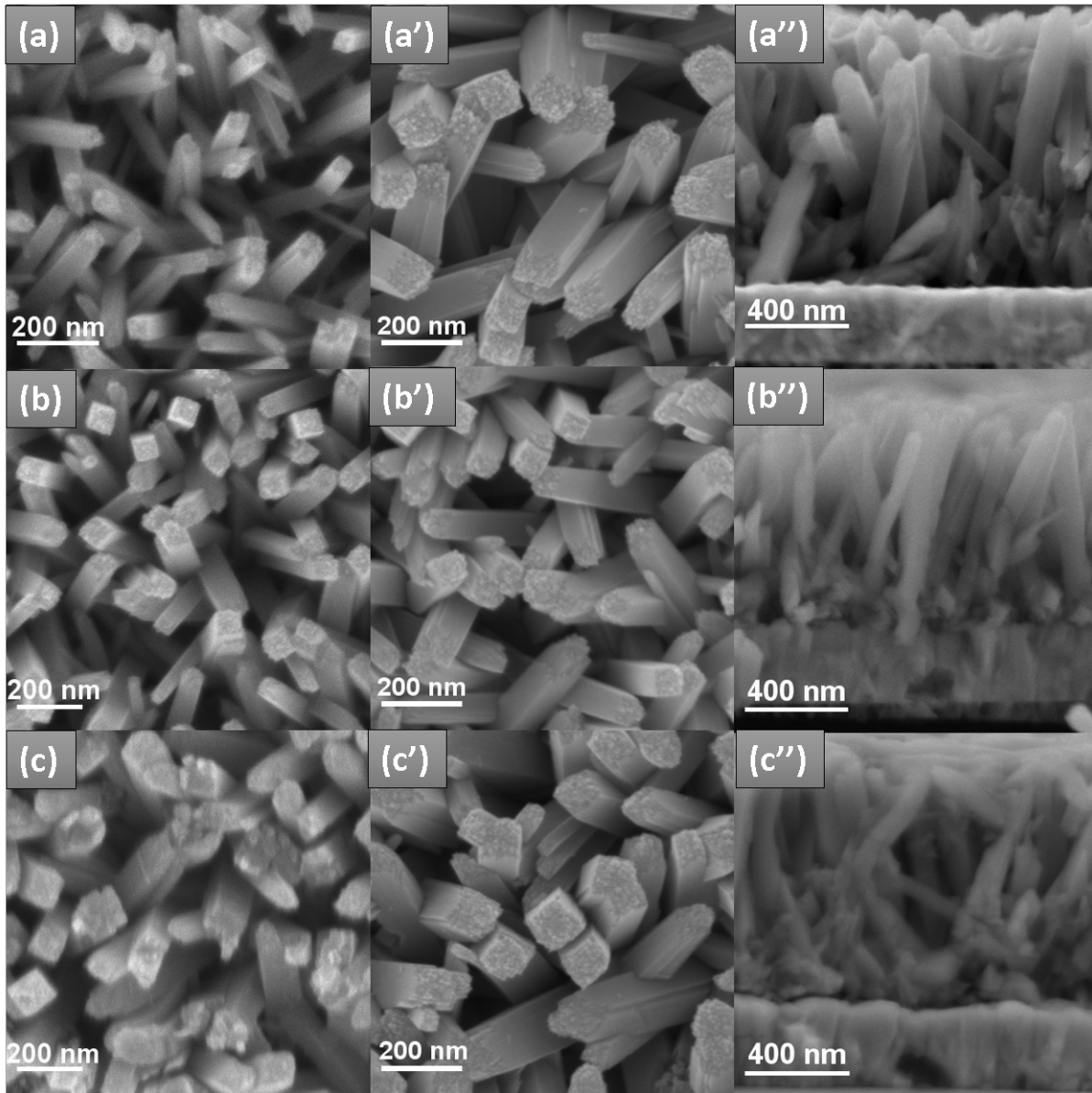


**Fig. 4.3:** *Top Row:* 100 W plasma treatment: (a) untreated, (a') treated, (a'') cross-section; *Middle Row:* 300 W plasma treatment: (b) untreated, (b') treated, (b'') cross-section. *Bottom Row:* 500 W plasma treatment: (c) untreated, (c') treated, (c'')



cross-section. For all irradiated samples, the time of exposure and substrate temperature are fixed at 10 mins and room temperature, respectively.

Youseff *et al* [4.6] observed that increasing the plasma power from 64 W to 100 W increases the growth rate of N-TiO<sub>2</sub>. Additionally, the group showed that the growth rate was slowed by the doping process, especially on Ni supports. In particular, when introducing NH<sub>3</sub> gas into the plasma phase, it was found that reactive-species reactions were favoured into the plasma gaseous volume more than on substrate surface. This leads to a competition between species-species (volume) collisions and species-solid (substrate) interactions [4.5], subsequently leading to the observed lower growth rate. These structural differences directly relate to the plasma power in the preparation of the films and have a direct impact on the material's photo-electrochemical behaviour [4.5]. Relating these findings to this study, the increase in nanowire diameter with increasing plasma power may well be due to domination by the species-species collisions, subsequently increasing the growth rate. A study of the growth model proposed by Wisnet *et al* [4.1], shows that the competition in growth rates of the different nanowire facets ultimately controls the observed nanowire diameter. As such, the bigger nanowire diameters measured post irradiation in Fig. 4.3 is ascribed to an increase in the {111} crystal faces, which are responsible for the nanowire diameter [4.1].

**Table 4.1:** Summary of the diameter and length of the nanowire arrays before and after plasma irradiation at increasing plasma power.

	TiO <sub>2</sub>	TiO <sub>2</sub> 100 W	TiO <sub>2</sub> 300 W	TiO <sub>2</sub> 500 W
<b>Diameter (nm)</b>	62.7 ± 5.7	62.7 ± 9.6	94.6 ± 7.7	122.4 ± 17.9
<b>Length (nm)</b>	1089 ± 30	1018 ± 57	807 ± 35	897 ± 25

#### 4.2.2 Crystallinity and Structural Properties

Characterisation of the nitrogen treated TiO<sub>2</sub> samples with GIXRD are analysed and discussed. An exploration into the structural composition of the particle size at the grain boundary, lattice



constants  $a$  and  $c$  with the lattice strain of the intersecting nitrogen treated TiO<sub>2</sub> NW and pure TiO<sub>2</sub> are analysed. This is calculated using the Williamson-Hall method [4.7] and software packages Xpert Highscore™ and Microcal Origin™. The GIXRD patterns were collected to study the incorporation of the nitrogen in the metal-oxide lattices, the results of which are shown in Fig. 4.4. Diffraction patterns show that the TiO<sub>2</sub> NWs grow in the tetragonal rutile phase. It is important to consider the geometry of the incident x-ray beam, with the beam being parallel to the FTO/glass substrate and therefore perpendicular to the nanowire growth. It can be then observed that the TiO<sub>2</sub> nanowires grow mainly along rutile (101); this agrees with the TEM results of Fig. 4.2. The diffraction pattern show that the as-grown TiO<sub>2</sub> nanowire array has lattice constants  $a = 0.459$  nm and  $c = 0.295$  nm, which remain largely unchanged post N<sub>2</sub> plasma exposure.

Using the Williamson-Hall (W-H) transformation [4.7] of the GIXRD data the average crystalline grain-size decreases from 34 nm for the 100W TiO<sub>2</sub> NWs to 33.1 nm for the 300W TiO<sub>2</sub> NWs and then 28.2 nm for the 500W TiO<sub>2</sub> NWs. At the incident x-ray beam angle of 0.4°, these grain sizes are comparable to the nanowire diameter, which was determined to be in the range of 100 nm from the SEM results of Fig. 4.3. An increase in nanowire diameter post-N<sub>2</sub> plasma treatment can cause an increase in the lattice strain. It is observed by the W-H data of Table 4.2 that there is a trend for increasing lattice strain for increasing N<sub>2</sub> plasma power. The increase is caused by the passivation of the dangling of Ti bonds deep in the TiO<sub>2</sub> matrix, due to reactive nitrogen species of the plasma during doping; further quantification with XPS will be discussed below.

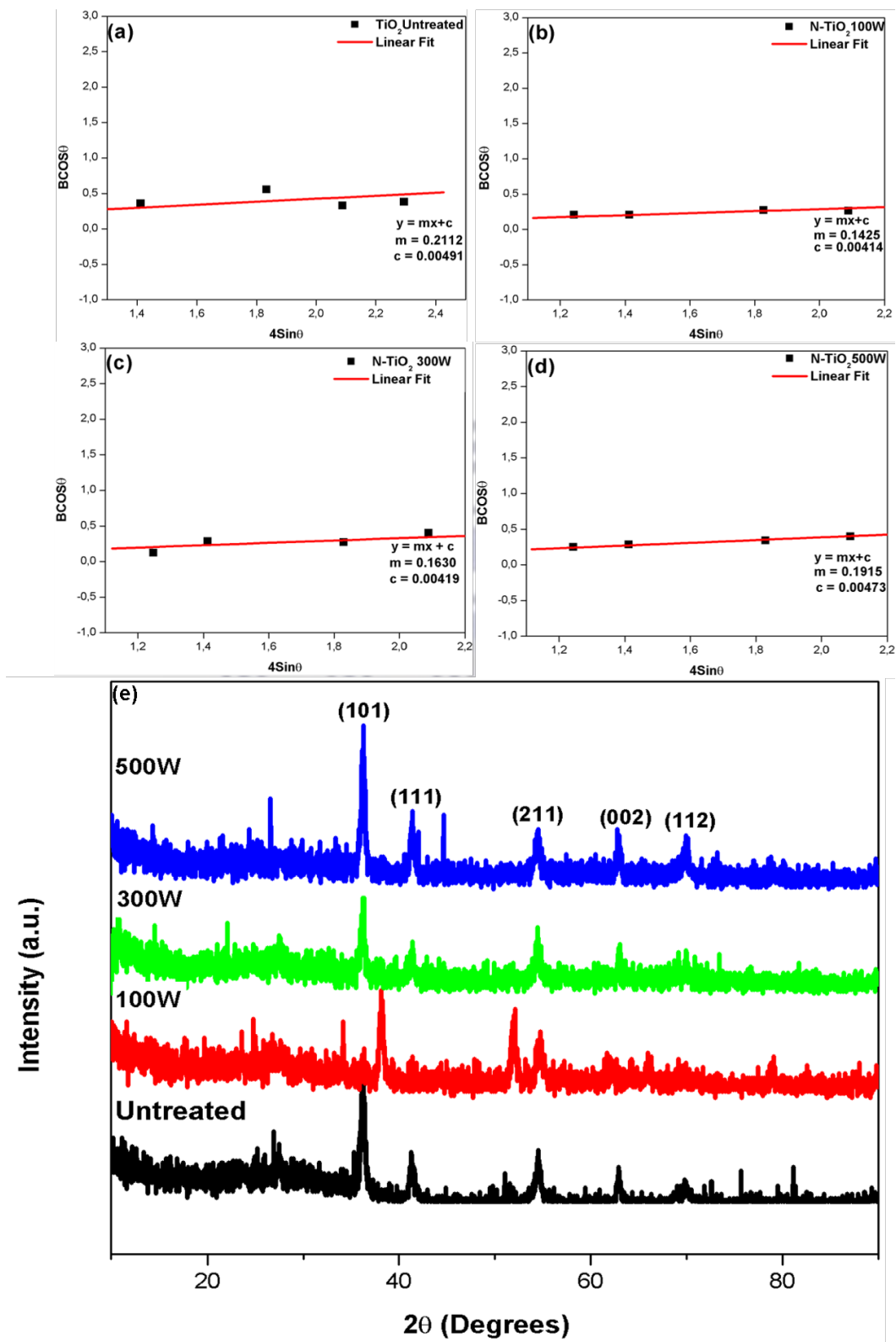


**Fig. 4.4:** W-H plots: (a) untreated  $TiO_2$ , (b) 100 W, (c) 300W, (d) 500W. (e) Stacked raw GIXRD patterns

**Table 4.2:** Calculated Structural properties for the effect of power series treated TiO<sub>2</sub>

Parameter	TiO <sub>2</sub>	TiO <sub>2</sub> 100W	TiO <sub>2</sub> 300W	TiO <sub>2</sub> 500W
Lattice Constants (a; c in nm)	0.461;0.294	0.459; 0.295	0.464; 0.292	0.460; 0.295
Aspect Ratio (a/c)	1.57	1.55	1.59	1.56
Volume (x 10 <sup>-1</sup> nm <sup>3</sup> )	0.98	0.96	1.00	0,97
Crystallite Size (nm)	28.24	33.49	33.09	28.18
Strain (x 10 <sup>-3</sup> )	212.1	142.5	163.0	191.5

#### 4.2.3 Chemical Bonding

An exploration into the chemical composition and bonding of the nitrogen treated and pure TiO<sub>2</sub> nanowires are discussed by studying the three major electronic line-shapes of TiO<sub>2</sub> and N, namely the titanium 2p (Ti-2p), oxygen 1s (O-1s) and nitrogen 1s (N-1s). In particular, the section will discuss the effects an increase in plasma power has on the relative composition of these energy levels, to elucidate the effective nitrogen doping profile at the different experimental conditions.

##### (a) Ti-2p Line-Shape

Fig. 4.5 compares the Ti 2p line-shapes of the TiO<sub>2</sub> nanowire arrays exposed to 100, 300 and 500 W nitrogen plasma to that of an untreated array. In all experiments, the time of exposure and substrate temperature were kept fixed at 10 minutes and room temperature, respectively. For the untreated sample it can be seen that the 2p<sub>3/2</sub> to 2p<sub>1/2</sub> states are in a relative ratio of 44.89% to 55.11%. This varies from the expected 1:1 ratio for TiO<sub>2</sub> as a result of the presence of oxygen vacancies throughout the TiO<sub>2</sub> lattice. When exposed to the nitrogen plasma at increasing power it can further be observed that the 2p<sub>3/2</sub> density of state decreases as a result of the formation of a Ti-N bond. At an exposed plasma power of 100W 6.06% of the Ti 2p<sub>3/2</sub> state is observed, which increases to 10.64 and ultimately 12.71% when increasing the power to 300 and 500 W, respectively. This clearly indicates that there is a direct relation between increasing N<sub>2</sub> plasma power and increasing N implantation into the nanowire array.

Fundamentally, the higher plasma power is highly energetic with greater kinetic energy. With high kinetic energy, the N<sub>2</sub> plasma has a greater probability of dislodging an oxygen atom from the Ti-O bond. Replacing the oxygen with nitrogen forming a Ti-N bond, this substitutional doping with N<sub>2</sub> has been extensively studied by Morikawa *et al* [4.8]. The higher kinetic energy of the N<sub>2</sub> plasma has an additional probability of implantation deep in the surface of the nanowire array. The Ti 2p<sub>1/2</sub> state is observed to increase from 55.11% in the pure sample to 59.47% for the 100W. Further increases are additionally observed when increasing the power to 300W at 62.14%. Increasing the plasma power to 500W, it is observed that the 2p<sub>1/2</sub> density of state decreased to 56.10%. Fig. 4.5 (a), (b), (c) and (d) all have satellite peaks located at 472.2 eV. As described by Frandon *et al* [4.9], these peaks are due to two unique physical processes. The first of which is charge transfer or shake-up excitations and energy, or may be described as a Ti 3p excitation of the type 3p<sup>6</sup> 3d<sup>0</sup> → 3p<sup>5</sup> 3d<sup>1</sup> and a likely contribution of 3p<sup>6</sup>3d<sup>0</sup>→ 3p<sup>6</sup> 3d<sup>0</sup> ed<sup>1</sup>, where ed is a continuous state [4.10].



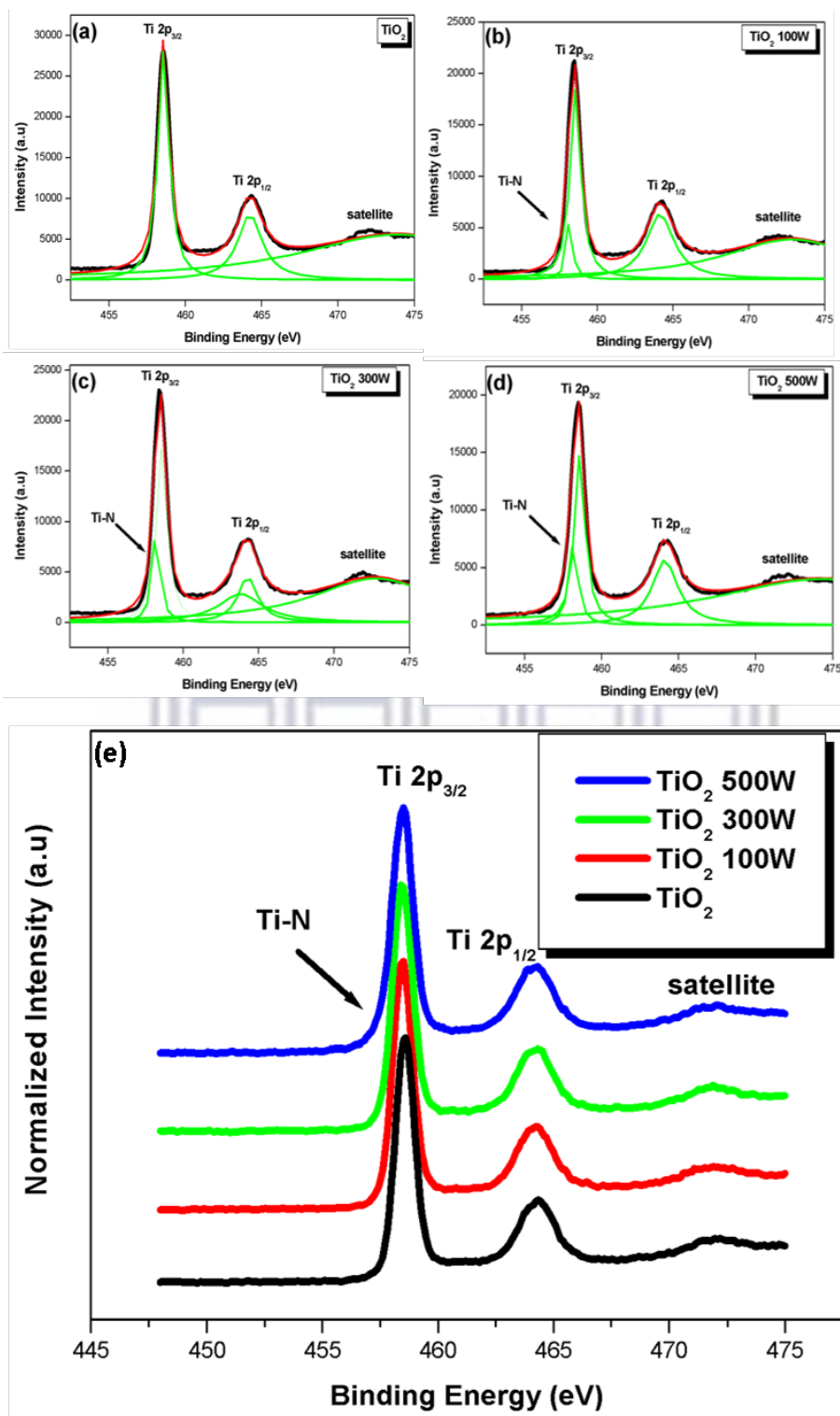


**Fig. 4.5:** Ti-2p plots showing the deconvolution of the peak profiles for (a) untreated, (b) 100 W (c) 300 W and (d) 500 W irradiated TiO<sub>2</sub> nanowire arrays; (e) Stacked plot directly comparing the changes in line-shapes. For all irradiated samples, the time



of exposure and substrate temperature are fixed at 10 mins and room temperature, respectively

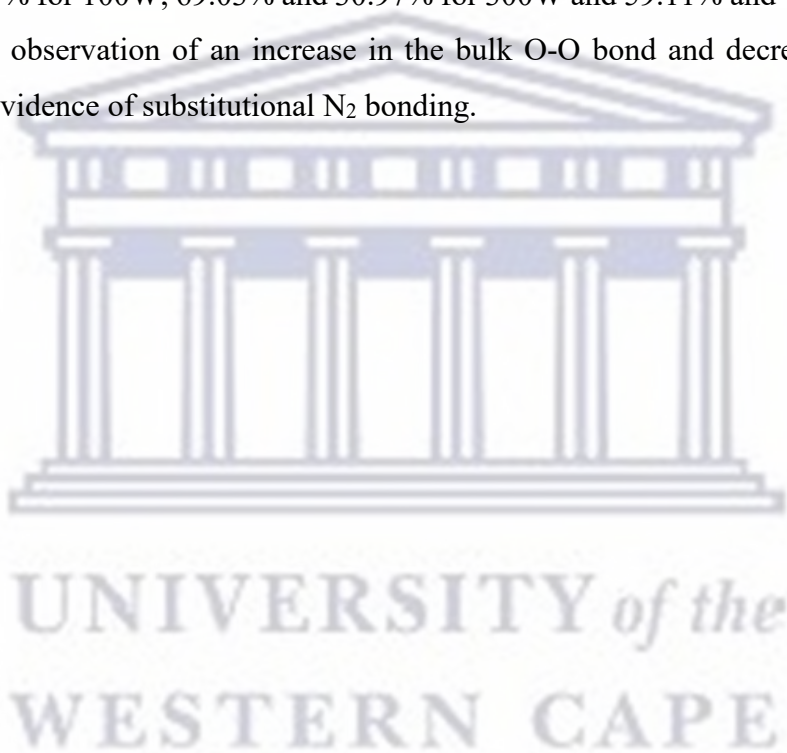
**Table 4.3:** Relative quantum efficiencies of the de-convoluted Ti-2p

	TiO <sub>2</sub>	TiO <sub>2</sub> 100W	TiO <sub>2</sub> 300W	TiO <sub>2</sub> 500W
Ti 2p <sub>3/2</sub> (f <sub>1</sub> )	5,22	5,22	5,22	5,22
Ti 2p <sub>1/2</sub> (f <sub>2</sub> )	2,68	2,68	2,68	2,68
Ti-N (f <sub>3</sub> )	5,22	5,22	5,22	5,22
Ti 2p <sub>3</sub> Area (A)	39298	24781	23029	19619
Ti 2p <sub>1</sub> Area (B)	24770	21951	26991	18117
Ti-N (C)	0	4357,1	9002,9	7994
(A/f <sub>1</sub> )	7528,35	4747,32	4411,69	3758,43
(B/f <sub>2</sub> )	9242,54	8190,67	10071,27	6760,07
(C/f <sub>3</sub> )	0,00	834,69	1724,69	1531,42
(A/f <sub>1</sub> +B/f <sub>2</sub> + C/f <sub>3</sub> )	16770,89	13772,68	16207,65	12049,92
<b>Ti 2p<sub>3/2</sub> (%)</b>	<b>44,89</b>	<b>34,47</b>	<b>27,22</b>	<b>31,19</b>
<b>Ti 2p<sub>1/2</sub> (%)</b>	<b>55,11</b>	<b>59,47</b>	<b>62,14</b>	<b>56,10</b>
<b>Ti-N (%)</b>	<b>0,00</b>	<b>6,06</b>	<b>10,64</b>	<b>12,71</b>
<b>Total</b>	<b>100,00</b>	<b>100,00</b>	<b>100,00</b>	<b>100,00</b>

*(b) O-1s Line-Shape*

Fig. 4.6 compares the O-1s peaks of the pure and irradiated NWs. For the untreated sample, a clean TiO<sub>2</sub> surface will normally terminate anions due to being readily polarised by cations, allowing for the surface potential to be reduced. Exposure to any environment allows the surface to quickly react with any moisture, forming a hydroxylated surface as pathway of manufacturing optimal neutralisation of charge. According to Pauling's rule of electronegativity, acidic sites, OH groups

and basic sites are all formed in addition to Ti-OH, which forms due to H<sub>2</sub>O chemisorption, and are present on the TiO<sub>2</sub> surfaces [4.11]. In Fig 4.6 these states are all denoted as “surface” states, whereas the “bulk” states refer to the oxygen bonded to the Ti atoms in the lattice, or so-called lattice oxides. A study of the relative ratio of bulk to surface states can give an indication of the possible vacant states present in the sample, and or further indication of doping. For the untreated TiO<sub>2</sub>, Fig 4.6 (a) shows that the bulk to surface states are in a relative ratio of 57.51 to 42.49; this varies from the expected 1:1 ratio for TiO<sub>2</sub> as a result of the presence of oxygen vacancies throughout the TiO<sub>2</sub> lattice. After increasing the power, the bulk to surface ratio has changed to 64.76% and 35.24% for 100W; 69.03% and 30.97% for 300W and 59.11% and 40.89% for 500W, respectively. This observation of an increase in the bulk O-O bond and decrease in the Ti-OH surface bonds is evidence of substitutional N<sub>2</sub> bonding.



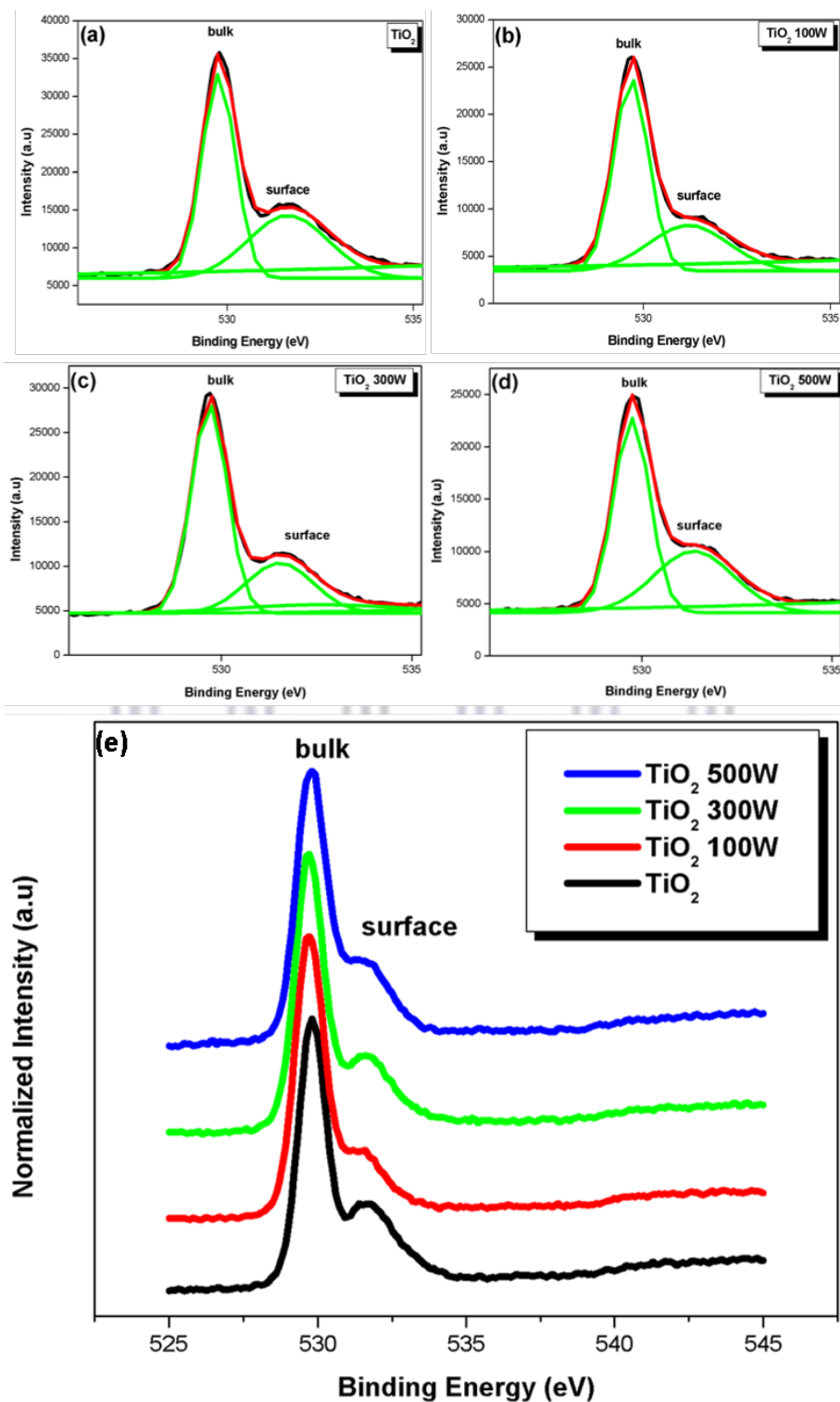


**Fig. 4.6:** O-1s plots showing the deconvolution of the peak profiles for (a) untreated, (b) 100 W (c) 300 W and (d) 500 W irradiated TiO<sub>2</sub> nanowire arrays; (e) Stacked plot directly comparing the changes in line-shapes

**Table 4.4:** Relative quantum efficiencies of the de-convoluted O-1s peaks

	TiO <sub>2</sub>	TiO <sub>2</sub> 100W	TiO <sub>2</sub> 300W	TiO <sub>2</sub> 500W
Bulk (O-O)	2,93	2,93	2,93	2,93
Surface (Ti-OH)	2,93	2,93	2,93	2,93
Bulk (O-O) area	30375	23707	27739	22173
Surface (Ti-OH) area	22441	12901	12443	15340
(A/f <sub>1</sub> )	10366,89	8091,13	9467,24	7567,58
(B/f <sub>2</sub> )	7659,04	4403,07	4246,76	5235,49
(A/f <sub>1</sub> +B/f <sub>2</sub> )	18025,94	12494,20	13713,99	12803,07
<b>Bulk (O-O) %</b>	<b>57,51</b>	<b>64,76</b>	<b>69,03</b>	<b>59,11</b>
<b>Surface (Ti-OH) %</b>	<b>42,49</b>	<b>35,24</b>	<b>30,97</b>	<b>40,89</b>
<b>Total</b>	<b>100,00</b>	<b>100,00</b>	<b>100,00</b>	<b>100,00</b>

*(c) N-1s Line-Shape*

Fig. 4.7 (a)-(c) all show a single N-1s organic peak at 400 eV, whereas in Fig. 4.6 (d) a peak at 396.25 eV is observed, which is assigned to the formation of a Ti-N bond. The organic N to TiN states is in a relative ratio of 61.57% to 38.43%, as shown in Table 4.5. Cheng *et al* [4.12] reported on N-1s peaks in a similar study and states that these peaks emanate from the introduction of the doping species during the synthesis method and indicated three different types of N states. The main peak at binding energy of 399.5eV was attributed to the N atom in the environment of the N-Ti-O [4.13, 4.14] while another two small peaks at 397.4 and 401.7 eV were assigned to substitutional nitrogen in the Ti-N structure and the presence of interstitial N state as the characteristic of NO/NO<sub>2</sub> in the N doped TiO<sub>2</sub> sample [4.15-4.17], respectively. Therefore, a conclusion that the chemical states of the nitrogen doped into TiO<sub>2</sub> may be various and coexist in the form of substitutional N-Ti-O and Ti-N, also as interstitial NO/ NO<sub>2</sub> can be made.

These multi-type nitrogen doping can induce the formation of new energy level in the forbidden band of TiO<sub>2</sub> and relate to the enhancement of photo-catalytic activity in the visible range [4.18]. Literature also shows that substitutionally-doped nitrogen exhibits a peak at around 396 eV while the interstitially doped nitrogen exhibits a peak at 400 eV. Many of the substitutional-doped samples reported also show a small peak at 400 eV, indicating that they may contain some interstitial nitrogen as well and therefore it is not entirely reliable for evidence of a correlation between photocatalytic properties and either of the doping arrangements [4.19]. As such, it can be concluded that the exposure of the nanowires to the more kinetic plasma species at 500 W, clearly results in both substitutional and interstitial nitrogen doping in the TiO<sub>2</sub> lattice.

#### 4.2.4 *Optical Properties*

The light transmission properties of the as-synthesised and plasma irradiated TiO<sub>2</sub> NWs using light from a Semiconsoft© spectrometer using both Deuterium (UV) and Halogen (Vis) as illumination sources are reported. The samples were illuminated from the glass-side, simulating the conditions of a photovoltaic device, with the light waves first travelling through the glass layer, then FTO and finally the NW layer. The resultant transmission curves are plotted for the three series of experimental conditions as reported in previous sections of this chapter.

UNIVERSITY of the  
WESTERN CAPE



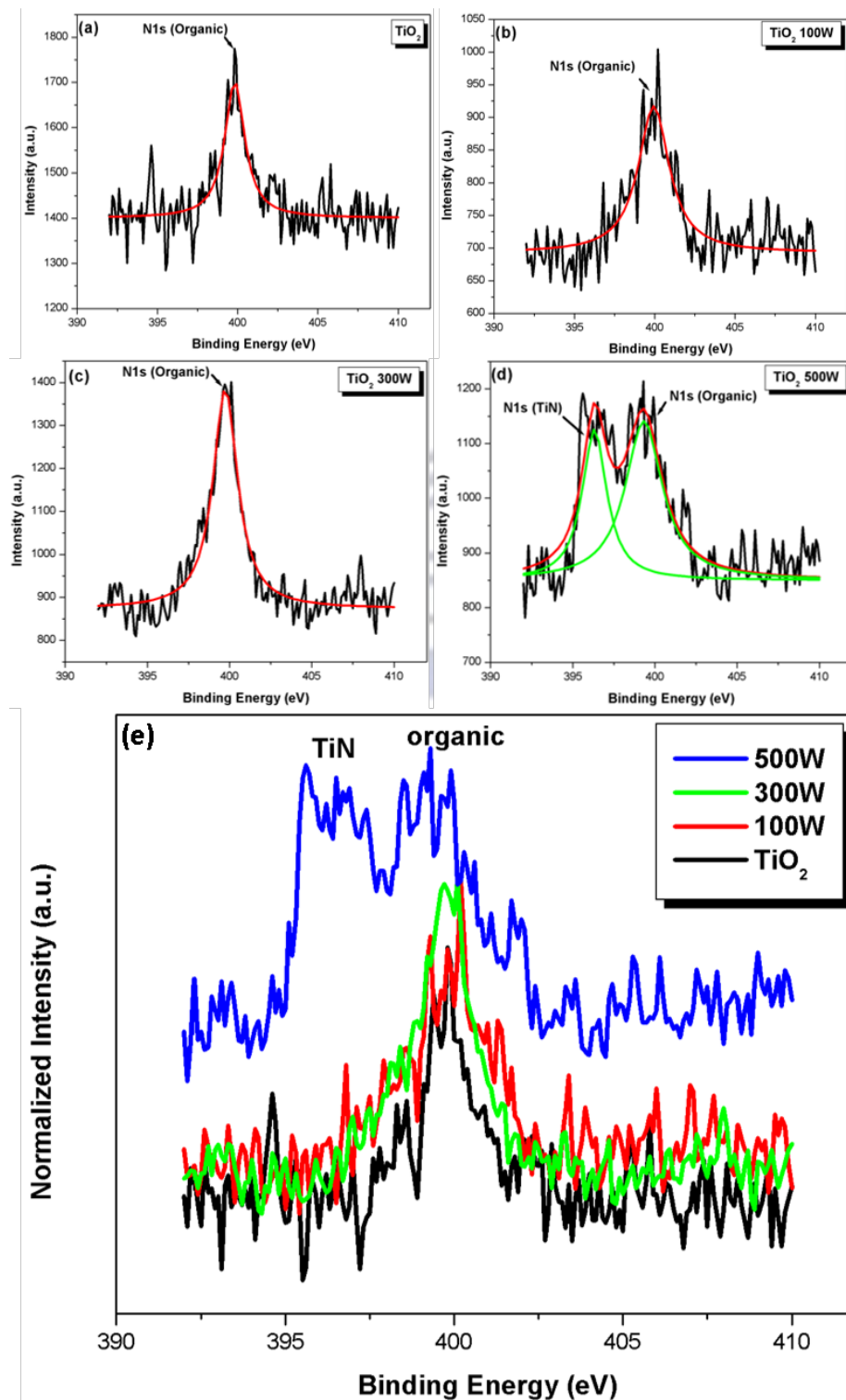


**Fig. 4.7:** N-1s plots showing the deconvolution of the peak profiles for (a) untreated, (b) 100 W (c) 300 W and (d) 500 W irradiated TiO<sub>2</sub> nanowire arrays; (e) Stacked plot directly comparing the changes in line-shapes

**Table 4.5:** Relative quantum efficiencies of the de-convoluted N-1s peaks

	TiO <sub>2</sub>	TiO <sub>2</sub> 100W	TiO <sub>2</sub> 100W	TiO <sub>2</sub> 500W
N1s (Organic)	1,8	1,8	1,8	1,8
N1s (TiN)	1,8	1,8	1,8	1,8
N1s (Organic)	709,63475	825,9667	1458,095	1257,065
N1s (TiN)	0	0	0	784,5
(A/f <sub>1</sub> )	394,24	458,87	810,05	698,37
(B/f <sub>2</sub> )	0,00	0,00	0,00	435,83
(A/f <sub>1</sub> +B/f <sub>2</sub> )	394,24	458,87	810,05	1134,20
<b>N1s (Organic)%</b>	<b>100,00</b>	<b>100,00</b>	<b>100,00</b>	<b>61,57</b>
<b>N1s (TiN)%</b>	<b>0,00</b>	<b>0,00</b>	<b>0,00</b>	<b>38,43</b>
<b>Total</b>	<b>100,00</b>	<b>100,00</b>	<b>100,00</b>	<b>100,00</b>

Fig. 4.8 shows the optical transmission spectra in the 350 – 900nm wavelength range for the nanowires exposed to increasing plasma power as indicated in the figure. The results show transmission of the arrays occurring in the visible range (400-700 nm) and the near-infrared range (700 -900 nm). Not all nanowire arrays are highly transparent, as seen in Fig. 4.8 samples have above 29 % transmittance and present a sharp cut-off at approximately 400 nm for the untreated sample and 468 nm for the treated samples. Individually, the transmittance for each sample stabilises around 900 nm at: 68.4 % for untreated TiO<sub>2</sub>, 40.5 % for 100W, 52.9 % for 300W and 29.5 % for 500W. The transmission variance is directly attributed to the structure of the nanowires. In particular, the alignment of the nanowires plays a major role during light guidance through the array. As was shown in Fig. 4.2, greater alignment is seen in the 300W SEM micrograph, compared to the 100W and 500W samples, resulting in greater light transmission in the 300W sample. The nanowire diameter may also play a role during light scattering and ultimately transmission; however, this is a small compared to the orthogonal alignment of the nanowires to the FTO substrate.

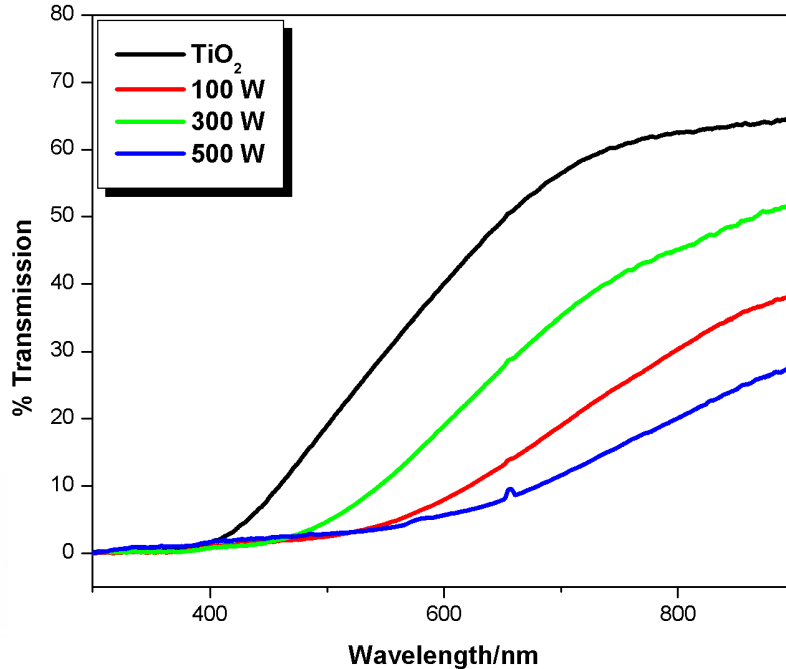


**Fig. 4.8:** UV-Vis transmission spectra of the N<sub>2</sub> plasma treated nanowire array on the FTO substrate. With the stacked raw patterns: (black) untreated TiO<sub>2</sub>, (red) 100 W, (green) 300W, (blue) 500W

Observed in Section 4.2.1, the 300W sample has a smaller average nanowire diameter compared to 500W sample. Relating these findings to this study, it can be said that the increase in alignment in TiO<sub>2</sub> nanowire arrays yields greater transmittance in both the visible and infrared regions of the electromagnetic spectrum. Thus, for controlled fabrication of nanowires, greater alignment enhances any potential device fabrication. A further observation is the clear shift in transmission towards longer wavelengths, as shown in Fig. 4.8. This red-shift is directly assigned the onset of the absorption curve at lower energy levels, which in turn, can be related to the increase in nitrogen doping at higher plasma power irradiation; nitrogen doping is well-known to decrease the optical bandgap of TiO<sub>2</sub>. Franco *et al* [4.21] found similar results where undoped TiO<sub>2</sub> thin films had an estimated bandgap of 3.2 eV. After N<sub>2</sub> doping, the optical bandgap of the N-doped TiO<sub>2</sub> films were decreased to 2.1 eV.

Research by Dhar *et al* [4.22] also showed a decrease in bandgap of N-doped TiO<sub>2</sub> NWs compared to that of undoped NWs. After nitrogen doping, the bandgap shifted from 3.51 eV to 3.0 eV. This was suggested to result from the transition from the N<sub>2p</sub> trap sites of the material to the conduction band. A further transition at 2.1 eV suggests that the TiO<sub>2</sub> lattice may be modified by substitution of O atoms with N atoms as the Nitrogen exposure was increased. With the aforementioned results demonstrating the doping with nitrogen may cause a narrowing of the bandgap of TiO<sub>2</sub>, implying activity in the visible light range.

### 4.3 Effect of Extended Exposure Time on the Morphological, Structural and Optical Properties of Individual TiO<sub>2</sub> Nanowires

The effects increasing the exposure time during irradiation on the above-mentioned properties are investigated in this section. For all samples, the plasma power and substrate temperature are kept constant at 100 W and room temperature, respectively. During a typical experiment, a base pressure of  $1.2 \times 10^{-5}$  mbar is maintained, prior to feeding an Ar and N<sub>2</sub> gas mixture into the chamber at a flow-rate of 100 sccm each, ultimately reaching a desired chamber vacuum of  $5.0 \times 10^{-2}$  mbar. At this point, the plasma is ignited and slowly ramped to 100 W. As soon as the power is stabilised, the Ar flow-rate is reduced to 0 sccm. This point signals the start of the irradiation process with exposure periods of 10, 30 and 60 minutes investigated.

#### 4.3.1 TiO<sub>2</sub> Nanowire Morphology

The morphologies of the nanowires exposed for 10, 30 and 60 mins to the nitrogen plasma, at 100 W, are depicted in the SEM micrographs of Fig. 4.9. As was the case in Fig. 4.3, the images show that the surface of the FTO substrates is covered densely and uniformly with vertically oriented nanowires. The top-row shows the morphologies before and after 10 mins exposure, in which it is found that the nanowires have an average diameter of 86.1 nm, pre-irradiation, with small increase observed post-treatment. From Fig. 4.9 (a') an average diameter of 94.2 nm is recorded and an average length of 868.1 nm measured from Fig. 4.8 (a'').

Conversely, a trend of decreasing nanowire diameters and lengths are seen for the 30 mins (middle row) and 60 min (bottom row) treatments. Fig. 4.9 (b), (b'), and (b'') show the decreasing diameter and length as 93.1nm, 87.2 nm and length 329.4 nm respectively, whereas Fig. 4.9 (c), (c'), and (c'') show the decreasing diameter and length as, 71.3 nm, 126.0 nm and length 946.2 nm respectively. Similar to the power series results of Fig. 4.3, a decrease in the areal density is seen the plain-view SEM images with the cross-sectional SEM micrographs once more showing the nanowire orientation greatly distorted post N<sub>2</sub> treatment.

Huang *et al* [4.18] reported increasing the N<sub>2</sub> plasma treatment time of TiO<sub>2</sub> nanotubes, resulted in the decreasing surface area, and in turn length and increasing the pore diameter, attributing to the growth of TiO<sub>2</sub> crystallinities during thermal annealing. Barakat *et al* [4.19] conversely, conducted similar plasma treatment experiments of TiO<sub>2</sub>, but resulted in no profound changes of surface area between the raw and treated samples at 400 °C for 60 min. Additionally, research by Ishihara *et al* [4.20] curiously found that N<sub>2</sub> plasma surface-treatment was directly related to better photocurrent density of TiO<sub>2</sub> nanotube arrays for treated samples between 10 to 60 min.

Exposure to the plasma for 10 mins was postulated to be too short for N-doping in crystallite TiO<sub>2</sub> structures, whereas 60 min of N-doping was found to be too long and harmful to the TiO<sub>2</sub> structure, causing induced surface defects. The group found that 20 min exposure to be optimal. Consequently, it can be concluded that the prolonged exposure of the nanowires to the plasma at 100 W in study may cause enhanced surface defects and etching of the nanowires, causing the reduced nanowire diameter observed in Fig. 4.8. Similarly, increasing the exposure time also allows the plasma radicals to significantly distort the Van Der Waals electrostatic forces and as such the orientation of the nanowires to the FTO substrate. To investigate the structural properties, W-H and GIXRD are conducted and will be discussed in the next section.



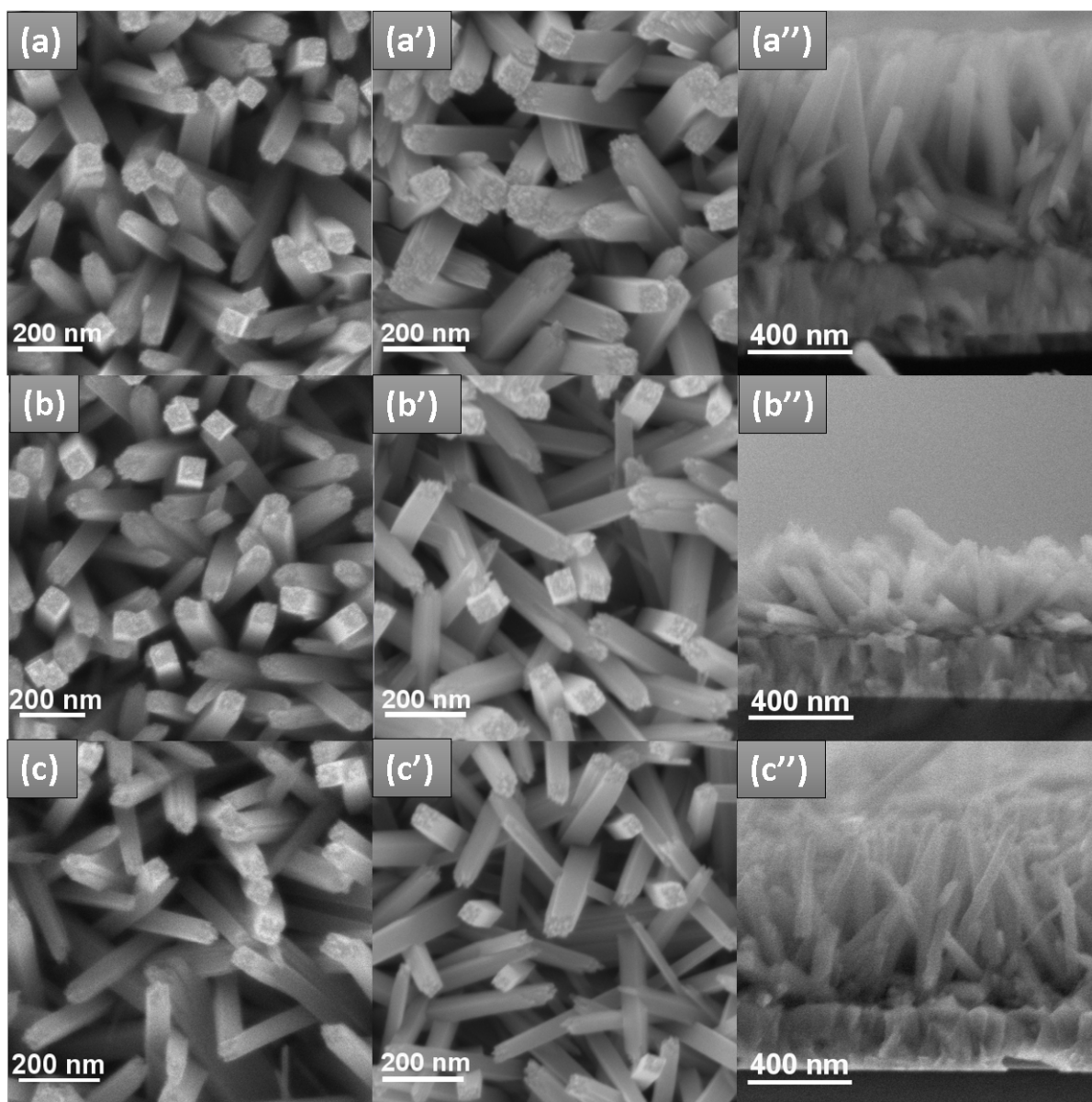


**Fig. 4.9:** *Top Row:* 10 mins plasma treatment: (a) untreated, (a') treated, (a'') cross-section; *Middle Row:* 30 min plasma treatment: (b) untreated, (b') treated, (b'') cross-section. *Bottom Row:* 60 min plasma treatment: (c) untreated, (c') treated, (c'') cross-section. For all irradiated samples, the plasma power and substrate temperature are fixed at 100W and room temperature, respectively

**Table 4.6:** Summary of the diameter and length of the nanowire arrays before and after plasma irradiation at increasing exposure time.

	TiO <sub>2</sub>	TiO <sub>2</sub> 10 min	TiO <sub>2</sub> 30 min	TiO <sub>2</sub> 60 min
<b>Diameter (nm)</b>	62.7 ± 5.7	94.2 ± 6.7	87.2 ± 9.8	64.2 ± 7.9
<b>Length (nm)</b>	1089 ± 30	367 ± 43	424 ± 54	676 ± 25

#### 4.3.2 Crystallinity and Structural Properties

The diffraction patterns of Fig. 4.10 show once more that the TiO<sub>2</sub> NWs grow in the tetragonal rutile phase, with the (101) orientation preferable. The as-grown, non-exposed sample has lattice constants  $a = 0.464$  nm and  $c = 0.292$  nm. Using the W-H transformation, shown in Fig. 4.9 (a)-(d) and Table 4.8, the average crystalline grain-size decreases from 33.1 nm for the 10 min TiO<sub>2</sub> NWs to 30 nm for the 30 min TiO<sub>2</sub> NWs. No GIXRD data could be collected for the 60 min sample, as the distorted sample surface resulted in domination of the FTO substrate, with no tangible diffraction peaks from the nanowire array observed. As shown in Table 4.8, the lattice strain increases with extended exposure time to the plasma. As was the case when increasing the power of the plasma, this increase may well be caused by the passivation of the dangling of Ti bonds deep in the TiO<sub>2</sub> matrix by reactive nitrogen species.

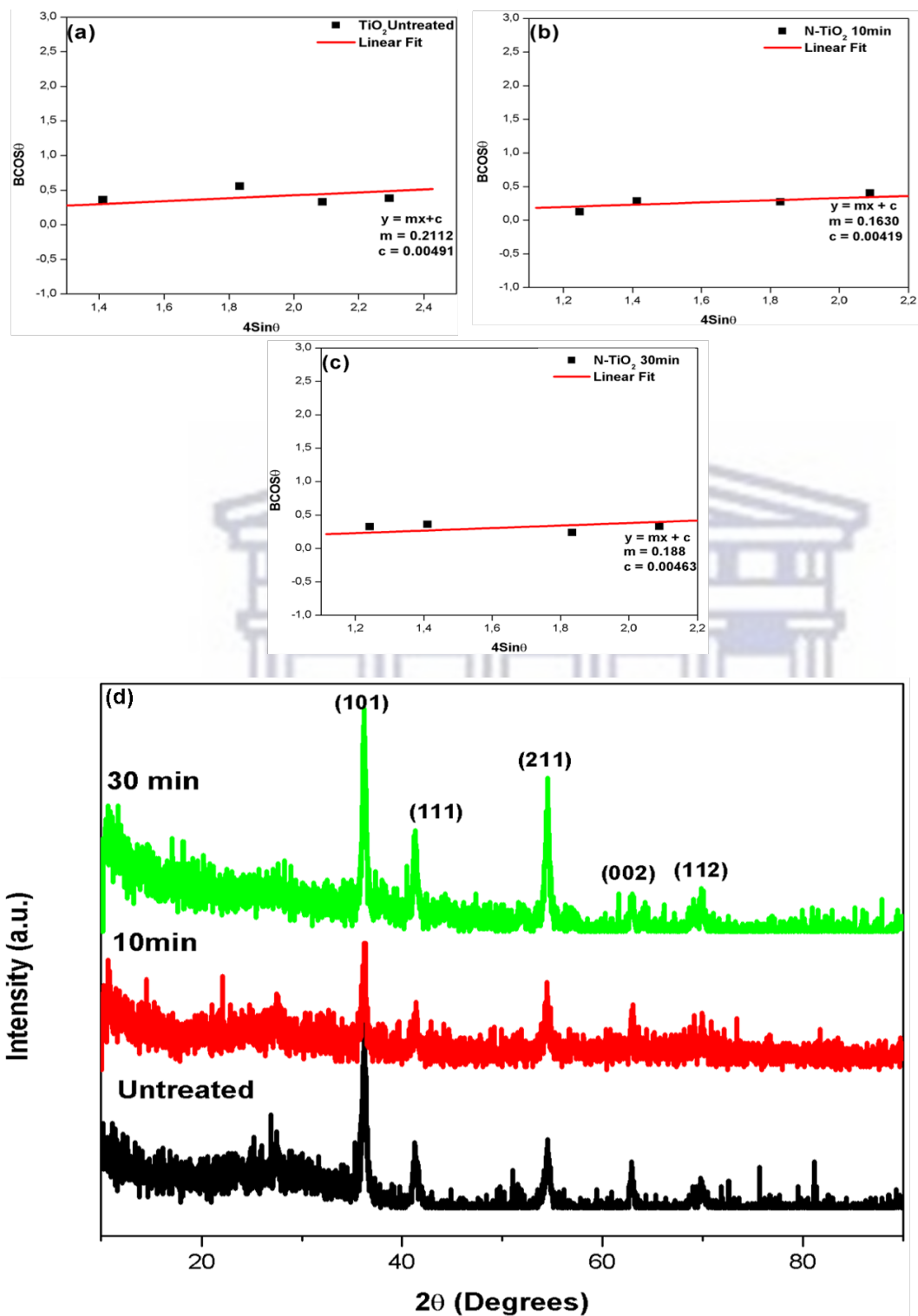


**Fig. 4.10:** Williamson-Hall plot for: (a) untreated  $\text{TiO}_2$ , (b) Nitrogen treated  $\text{TiO}_2$  NWs for 10 mins and (c) Nitrogen treated  $\text{TiO}_2$  NWs 30 mins at 100 W and the substrate at room temperature. (d) Stacked raw GIXRD data for (hkl) planes of the time series

**Table 4.7:** Calculated structural properties of the as-synthesised TiO<sub>2</sub> versus 10- and 30-min plasma exposure time

Parameter	TiO <sub>2</sub>	TiO <sub>2</sub> 10 min	TiO <sub>2</sub> 30 min
Lattice Constants (a; c in nm)	0.461;0.294	0.464; 0.292	0.460; 0.295
Aspect Ratio (a/c)	1.57	1.59	1.56
Volume (x 10 <sup>-1</sup> nm <sup>3</sup> )	0.98	1.00	0.97
Crystallite Size (nm)	28.24	33.09	29.95
Strain (x 10 <sup>-3</sup> )	212.1	163.0	188.0

### 4.3.3 Chemical Bonding

#### (a) Ti-2p Line-Shape

Fig. 4.11 compares the Ti-2p core-loss spectra. It can be observed that the untreated sample in Fig. 4.11 (a) has a 2p<sub>3/2</sub> to 2p<sub>1/2</sub> state ratio of 44.89 to 55.11, which varies from the expected 1:1 ratio for TiO<sub>2</sub> as a result of the presence of oxygen vacancies throughout the TiO<sub>2</sub> lattice. When exposed to the nitrogen plasma at increasing time periods it can further be observed that the 2p<sub>3/2</sub> density of state decreases as a result of the formation of a Ti-N bond. At an exposed plasma elapsed time of 10 mins 6.06% of the Ti 2p<sub>3/2</sub> state is observed, which increases to 11.51 and ultimately 13.21% when increasing the time to 30 and 60 mins, respectively. Fundamentally, the greater the elapsed time the greater the probability for collision between the N<sub>2</sub> plasma and the nanowire array. Which in turn results in greater doping of the sample.

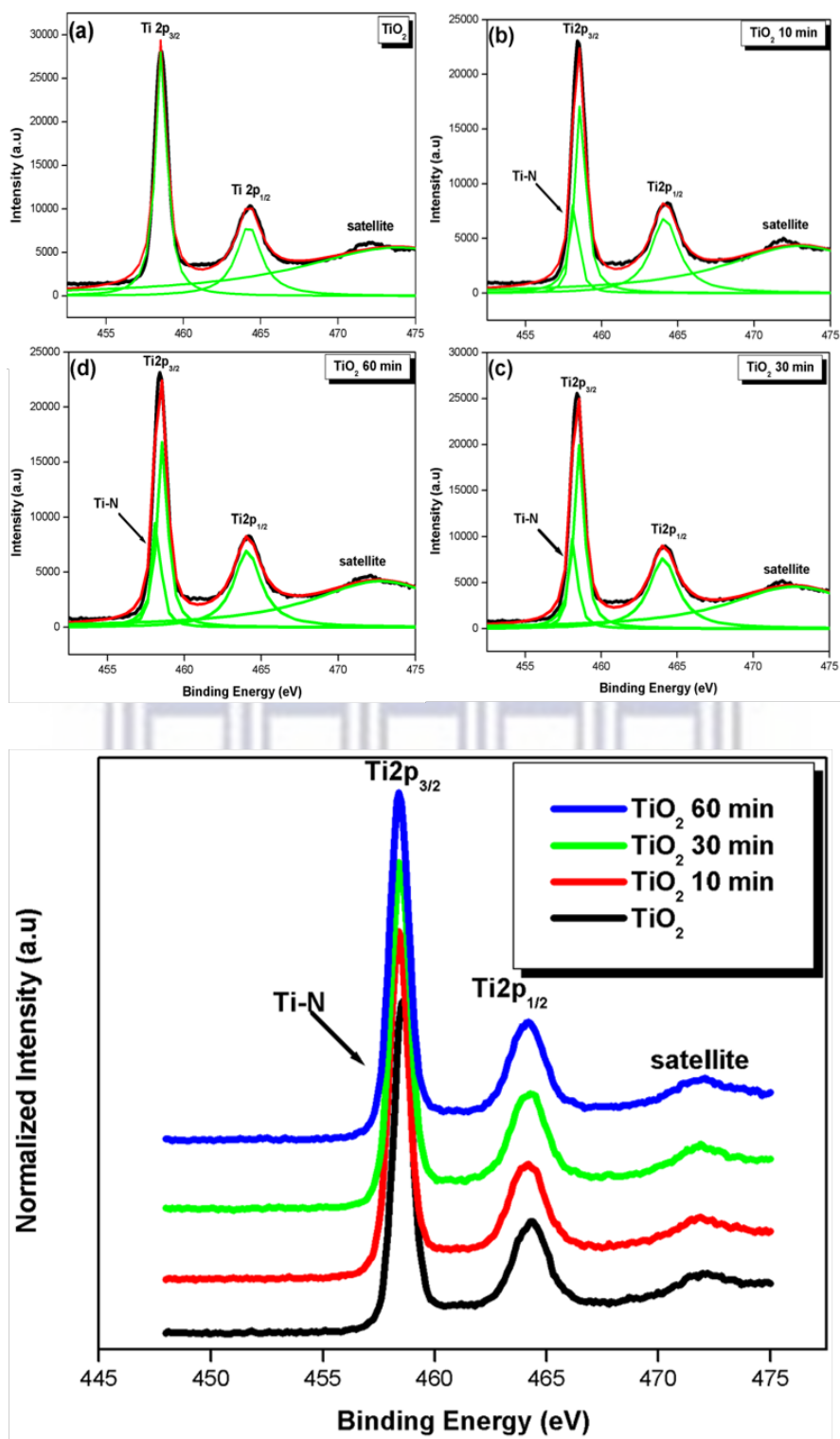


**Fig. 4.11:** Ti-2p plots showing the deconvolution of the peak profiles for (a) as-synthesised, (b) 10- (c) 30- and (d) 60-min exposed  $\text{TiO}_2$  nanowire arrays; (e) Stacked plot directly comparing the changes in line-shapes. For all irradiated samples, the



plasma power and substrate temperature are fixed at 100W and room temperature, respectively

**Table 4.8:** Relative quantum efficiencies of the de-convoluted Ti-2p

	TiO <sub>2</sub>	TiO <sub>2</sub> 10min	TiO <sub>2</sub> 30min	TiO <sub>2</sub> 60min
Ti 2p <sub>3/2</sub> (f <sub>1</sub> )	5,22	5,22	5,22	5,22
Ti 2p <sub>1/2</sub> (f <sub>2</sub> )	2,68	2,68	2,68	2,68
Ti-N (f <sub>3</sub> )	5,22	5,22	5,22	5,22
Ti 2p <sub>3</sub> Area (A)	39298	24781	25071	21263
Ti 2p <sub>1</sub> Area (B)	24770	21951	27198	23666
Ti-N (C)	0	4357,1	10150	10253
(A/f <sub>1</sub> )	7528,35	4747,32	4802,87	4073,37
(B/f <sub>2</sub> )	9242,54	8190,67	10148,51	8830,60
(C/f <sub>3</sub> )	0,00	834,69	1944,44	1964,18
(A/f <sub>1</sub> +B/f <sub>2</sub> + C/f <sub>3</sub> )	16770,89	13772,68	16895,83	14868,14
<b>Ti 2p<sub>3/2</sub> (%)</b>	<b>44,89</b>	<b>34,47</b>	<b>28,43</b>	<b>27,40</b>
<b>Ti 2p<sub>1/2</sub> (%)</b>	<b>55,11</b>	<b>59,47</b>	<b>60,07</b>	<b>59,39</b>
<b>Ti-N (%)</b>	<b>0,00</b>	<b>6,06</b>	<b>11,51</b>	<b>13,21</b>
<b>Total</b>	<b>100,00</b>	<b>100,00</b>	<b>100,00</b>	<b>100,00</b>

(b) *O-1s Line-Shape*

Fig. 4.12 compares the O-1s core-loss spectra of the TiO<sub>2</sub> nanowire arrays modified at the different conditions. As shown, after increasing the time of exposure, the bulk- to- surface ratio changes to 69.03% and 30.97% for 10 mins; 64.01% and 35.99% for 30 mins and 62.16% and 37.84% for 60 mins, respectfully. This general decrease in the bulk O-O bond and increase in the Ti-OH surface bonds is evidence of substitutional N<sub>2</sub> bonding, as previously discussed.

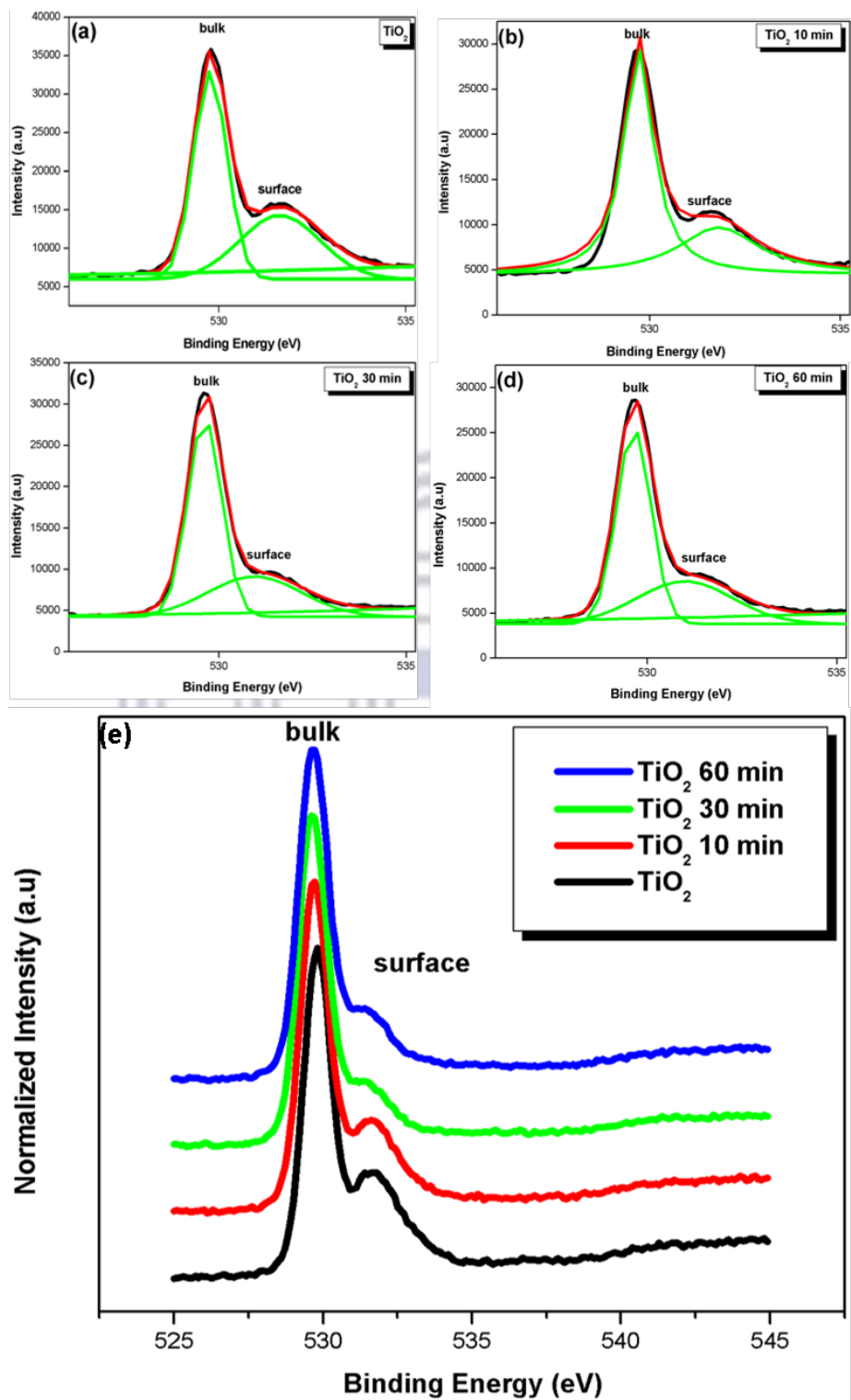


**Fig. 4.12:** O-1s plots showing the deconvolution of the peak profiles for (a) as-synthesised, (b) 10- (c) 30- and (d) 60-min exposed TiO<sub>2</sub> nanowire arrays; (e) Stacked plot directly comparing the changes in line-shapes

**Table 4.9:** Relative quantum efficiencies of the de-convoluted O-1s

	TiO <sub>2</sub>	TiO <sub>2</sub> 10 min	TiO <sub>2</sub> 30 min	TiO <sub>2</sub> 60 min
Bulk (O-O)	2,93	2,93	2,93	2,93
Surface (Ti-OH)	2,93	2,93	2,93	2,93
Bulk (O-O) area	30375	27739	27312	24690
Surface (Ti-OH) area	22441	12443	15359	15030
(A/f <sub>1</sub> )	10366,89	9467,24	9321,50	8426,62
(B/f <sub>2</sub> )	7659,04	4246,76	5241,98	5129,69
(A/f <sub>1</sub> +B/f <sub>2</sub> )	18025,94	13713,99	14563,48	13556,31
<b>Bulk (O-O) %</b>	<b>57,51</b>	<b>69,03</b>	<b>64,01</b>	<b>62,16</b>
<b>Surface (Ti-OH) %</b>	<b>42,49</b>	<b>30,97</b>	<b>35,99</b>	<b>37,84</b>
<b>Total</b>	<b>100,00</b>	<b>100,00</b>	<b>100,00</b>	<b>100,00</b>

*(c) N-1s Line-Shape*

Fig. 4.13 compares the deconvoluted N-1s core-loss spectra. In all plots a single N-1s organic peak at 400 eV is observed. In the 30- and 60-mins exposed samples of Fig. 4.6 (c) and (d), however, TiN peak at 396.25 eV is also observed. At 30 mins of exposure (Fig. 4.13 (c)) the organic N and TiN are in a relative ratio of 67.18% to 32.12%, which increases to 82.21% to 17.79% when increasing the exposure to 60-min, as shown in Fig. 4.13 (d).

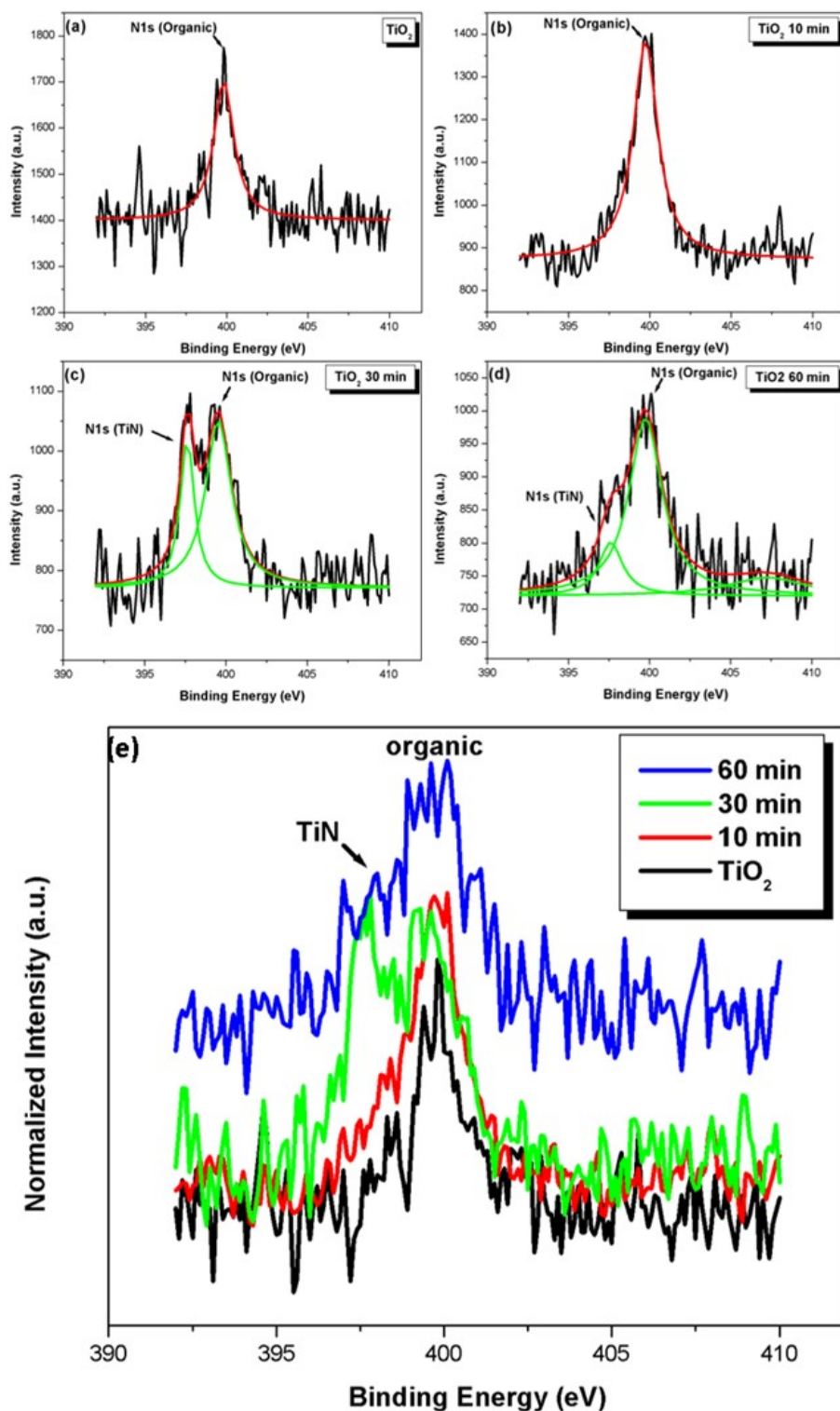


**Fig. 4.13:** N-1s plots showing the deconvolution of the peak profiles for (a) as-synthesised, (b) 10- (c) 30- and (d) 60-min exposed TiO<sub>2</sub> nanowire arrays; (e) Stacked plot directly comparing the changes in line-shapes

**Table 4.10:** Relative Quantum efficiencies of the de-convoluted N1s

	TiO <sub>2</sub>	TiO <sub>2</sub> 10 min	TiO <sub>2</sub> 30 min	TiO <sub>2</sub> 60 min
N1s (Organic)	1,8	1,8	1,8	1,8
N1s (TiN)	1,8	1,8	1,8	1,8
N1s (Organic)	709,6348	1458,095	850,4	1042,2
N1s (TiN)	0	0	415,52	225,49
(A/f <sub>1</sub> )	394,24	810,05	472,44	579,00
(B/f <sub>2</sub> )	0,00	0,00	230,84	125,27
(A/f <sub>1</sub> +B/f <sub>2</sub> )	394,24	810,05	703,29	704,27
<b>N1s (Organic)%</b>	<b>100,00</b>	<b>100,00</b>	<b>67,18</b>	<b>82,21</b>
<b>N1s (TiN)%</b>	<b>0,00</b>	<b>0,00</b>	<b>32,82</b>	<b>17,79</b>
<b>Total</b>	<b>100,00</b>	<b>100,00</b>	<b>100,00</b>	<b>100,00</b>

From the Fig 4.13 a general trend is observed as the O-O bonds in the bulk of the sample decrease with increasing Nitrogen plasma exposure time. This decrease in O-O bonds coincide with the increase of the surface Ti-OH bonds. This may be due to increased substitutional N-Ti-O and Ti-N as the O bonds are decreasing. As was the case when increasing the plasma power, and results reported by Cheng *et al* [4.12] on N-1s peaks in a similar study, again leads to the conclusion that the chemical states of the nitrogen doped into TiO<sub>2</sub> coexist in the form of substitutional N-Ti-O and Ti-N, as well as possible interstitial NO/ NO<sub>2</sub> can be made. These multi-type nitrogen doping can induce the formation of new energy level in the forbidden band of TiO<sub>2</sub> and relate to the enhancement of photo-catalytic activity in the visible range [4.17]. Many of the substitutional-doped samples reported also show a small peak at 400 eV, indicating that they may contain some interstitial nitrogen as well and therefore it is not entirely reliable for evidence of a correlation between photocatalytic properties and either of the doping arrangements [4.18].



#### 4.3.4 Optical Properties

Fig. 4.14 shows once more that the nanowire arrays are moderately transparent, with all samples having >50 % transmission and present a sharp cut-off at approximately 400 nm and at 324 nm for the 30 min sample. Individually, the transmittance for each sample stabilises around 900 nm at: 64.8 % for untreated TiO<sub>2</sub>, 52.5 % for 10 min, 60.3 % for 30 min and 54.9 % for 60 min. A possibly reason for the transmittance varying may be due to the structure of the nanowires. As per the discussion in the previous section, the alignment and change in nanowire diameter play roles in the observed optical behaviour of the arrays. As was shown in Fig. 4.9, similar alignment is seen in 10 min, 30 min and 60 min samples, which corresponds to the trend seen in Fig. 4.14 above of closely aligned transmission.

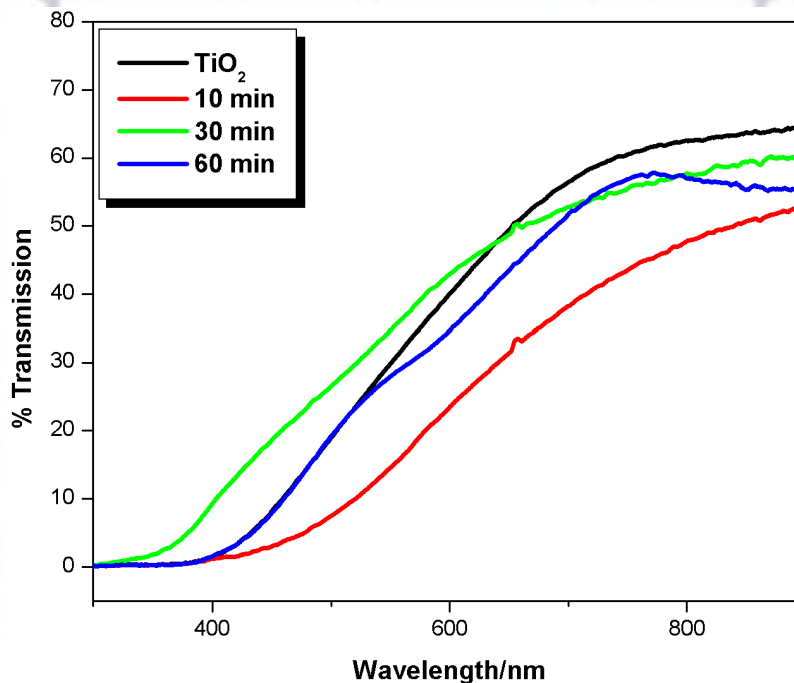


**Fig. 4.14:** UV-Vis transmission spectra of the N<sub>2</sub> plasma treated nanowire array on the FTO substrate. With the stacked raw patterns: (black) untreated TiO<sub>2</sub>, (red) 10 min, (green) 30 min, (blue) 60 min

Revisiting the results of Table 4.7, however, it is found that the much shorter nanowire length of the 30 min sample may influence the transmission of light through the individual nanowires. The observed transmission onset shows that the 10-minute exposed sample (red curve) yields the

biggest red-shift, whereas the 30- and 60-minute exposed samples, yield arbitrarily shifting onsets. This non-uniform shift may be ascribed to inhomogeneous doping of the TiO<sub>2</sub> surface; the samples presented in this series, are all exposed to a plasma power of 100 W, which as shown in the previous sections, may not generate nitrogen radicals with sufficient kinetic energy allowing for deep-level doping in the TiO<sub>2</sub> lattice.

#### **4.4 Effect of FTO Substrate Temperature on the Morphological, Structural and Optical Properties of Individual TiO<sub>2</sub> Nanowires**

The effects of annealing the FTO substrate during plasma irradiation on the above-mentioned properties are investigated in this section. For all samples, the plasma power and time of exposure are kept constant at 100 W and 10 mins, respectively. During a typical experiment, the substrate temperature is ramped from room temperature to the desired temperature at a ramp rate of 10 degrees per minute at a base vacuum of  $1.2 \times 10^{-5}$  mbar. Once the desired temperature is reached, Ar gas is fed into the chamber at a flow-rate of 100 sccm. Upon reaching a desired chamber vacuum of  $5.0 \times 10^{-2}$  mbar, N<sub>2</sub> is fed into the system at 100 sccm; the system is once again allowed to stabilise at a pressure of  $5.0 \times 10^{-2}$  mbar. At this point, the plasma is ignited and the power stabilised at 100 W. The Ar flow-rate is reduced to 0 sccm as soon as a stable plasma is achieved; this point signals the start of the irradiation process. Substrate temperatures of 100 and 300 °C are compared to a substrate kept at room temperature during irradiation.

##### *4.4.1 TiO<sub>2</sub> Nanowire Morphology*

The top-row of Fig. 4.15 compares top- and side-viewed SEM micrographs of the nanowires before and after irradiation, without heating of the FTO substrate. The middle row compares the nanowire morphology before and after irradiation, with the substrate heated at 100 °C; the bottom row compares the nanowire structure before and after irradiation at as substrate temperature of 300 °C. Table 4.12 summarises the diameters and lengths as measured from the SEM micrographs of Fig. 4.15. As was the case in the previous two series of investigations, a clear distortion in the nanowire alignment is observed post-irradiation. At this point, this effect is well-established and

attributable to the effects of the highly kinetic plasma species present in both nitrogen and argon plasmas. One interesting feature observed in Fig. 4.15 (c'), though, is the definite increase in the nanowire diameter post irradiation at a substrate annealing temperature of 300 °C. For these much thicker nanowires, the distortion in alignment by the plasma is clearly less pronounced. Wang *et al* [4.23] reported similar results of increasing diameter for TiO<sub>2</sub> films with an increase of temperature. In their research, TiO<sub>2</sub> films were annealed at 623 K for 1-hour, rounded particles of about 10 nm are then observed. Furthermore, larger particles, measuring from 25 - 55 nm, are also found when the TiO<sub>2</sub> thin films were further annealed at 823 K for 1 hour.

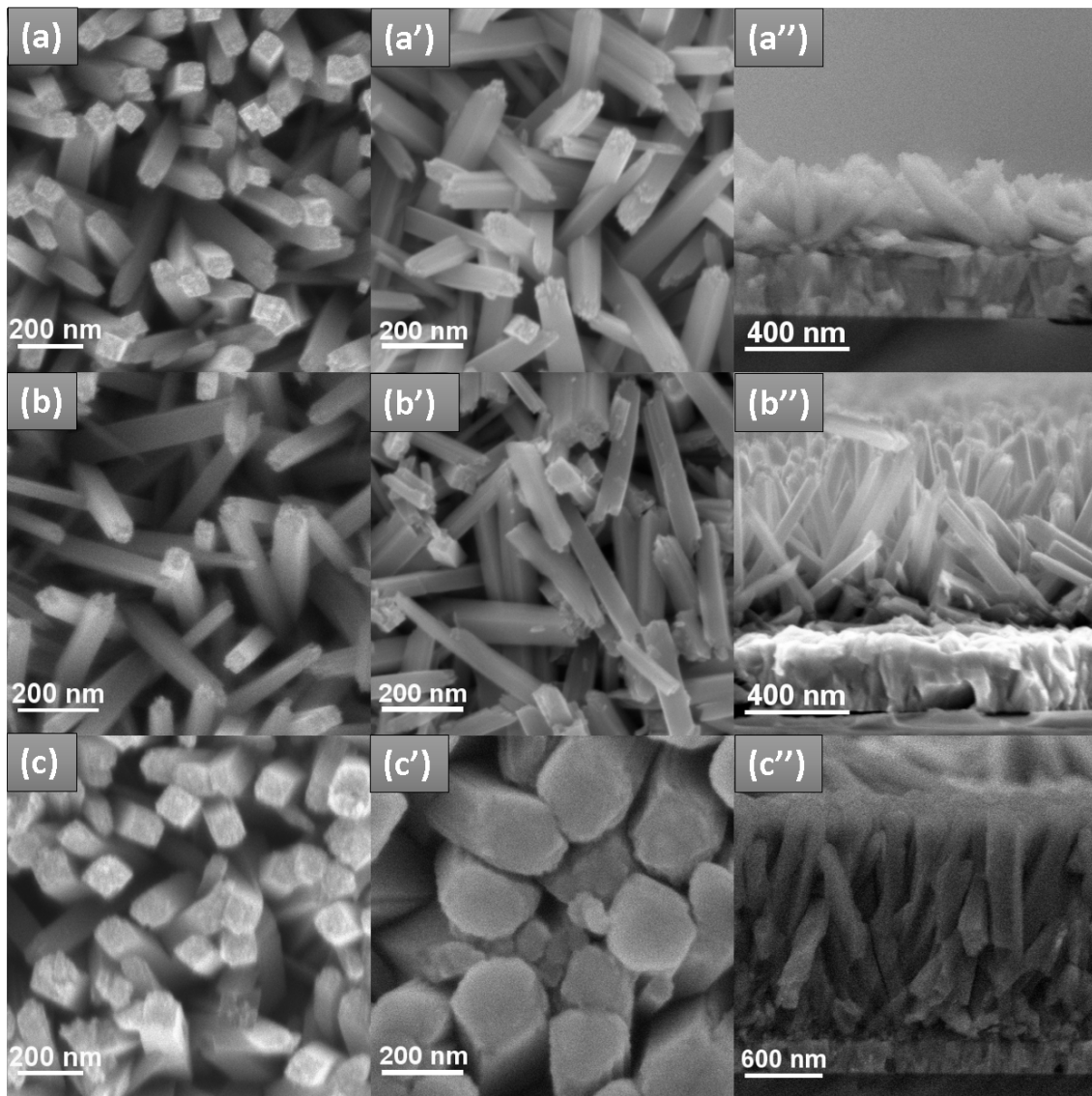


**Fig. 4.15:** *Top Row:* Room temperature irradiation: (a) untreated, (a') treated, (a'') cross-section; *Middle Row:* 100 °C irradiation: (b) untreated, (b') treated, (b'') cross-section. *Bottom Row:* 300 °C irradiation: (c) untreated, (c') treated, (c'') cross-section. For all irradiated samples, the time of exposure and plasma power are fixed at 10 mins and 100 W, respectively

During investigation of the power and time parameters, a decrease in the areal density of the nanowires was observed which is advantageous and can improve the electron-hole dissociation interface during photovoltaic device operation [4.3, 4.4]. Literature investigating the annealing of TiO<sub>2</sub> nanotubes/films at the optimal temperature in the N<sub>2</sub> and O<sub>2</sub> atmospheres is also of vital significance in order to impart high-electron conductivities which in turn leads to high photocurrent densities during operation. Several studies [4.24] have shown that an annealing temperature between 400–500 °C is optimal in transforming the amorphous phase of TiO<sub>2</sub> to crystalline anatase with a minimum amount in the rutile form. At higher temperatures increasing polycrystalline structure forms with greater amounts of rutile. These results show that nitrogen introduced in the TiO<sub>2</sub> lattice has a direct relation on both the crystallinity and electronic properties of the material. Which in turn will influence the optical properties. Similarly, it may be expected that the minimal morphological changes of the TiO<sub>2</sub> NWs post N<sub>2</sub> plasma treatment, will affect the optical properties of the material.

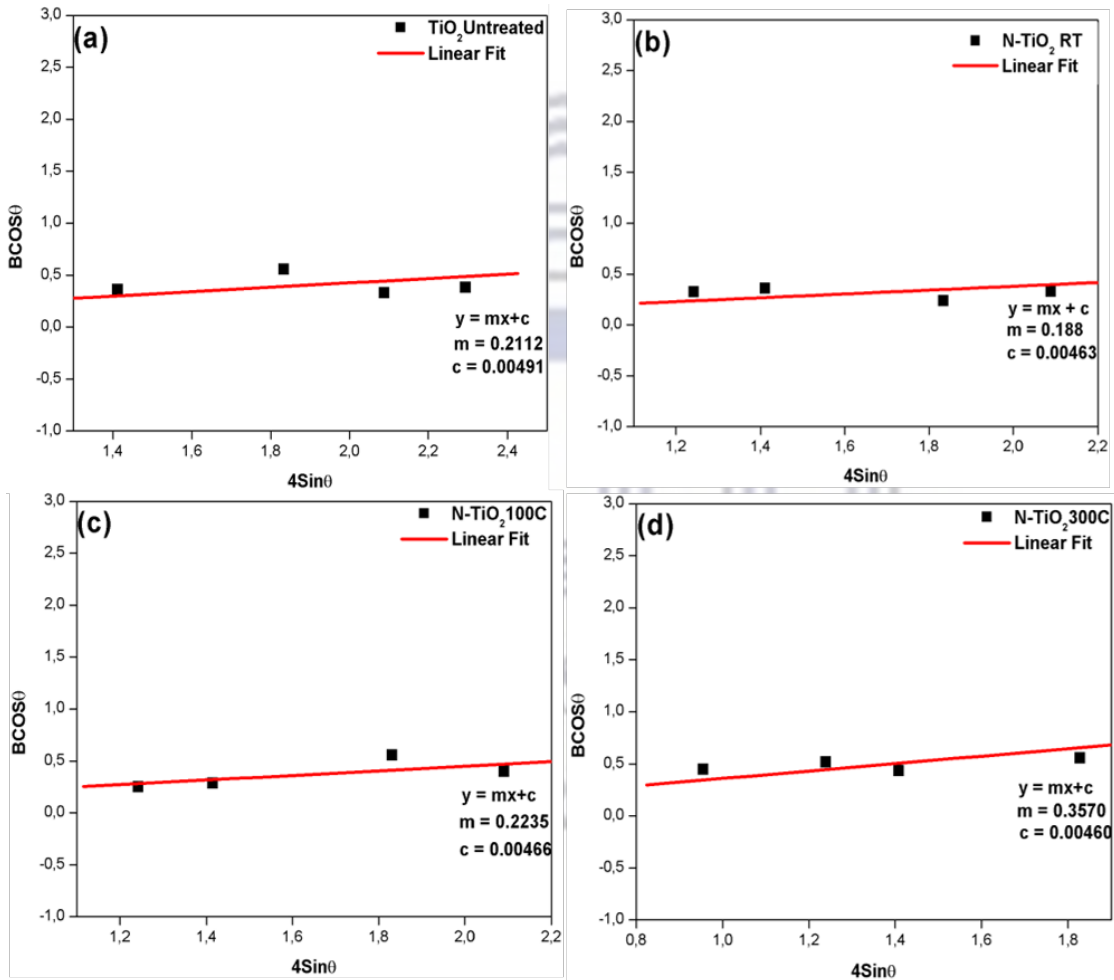
**Table 4.11:** Summary of the diameter and length of the nanowire arrays before and after plasma irradiation at increasing substrate annealing temperature

	TiO <sub>2</sub>	TiO <sub>2</sub> RT	TiO <sub>2</sub> 100 °C	TiO <sub>2</sub> 300 °C
<b>Diameter (nm)</b>	62.7 ± 5.7	88.6 ± 10.6	72.8 ± 5.6	272.4 ± 14.4
<b>Length (nm)</b>	1089 ± 30	363 ± 42	723 ± 34	1738 ± 28

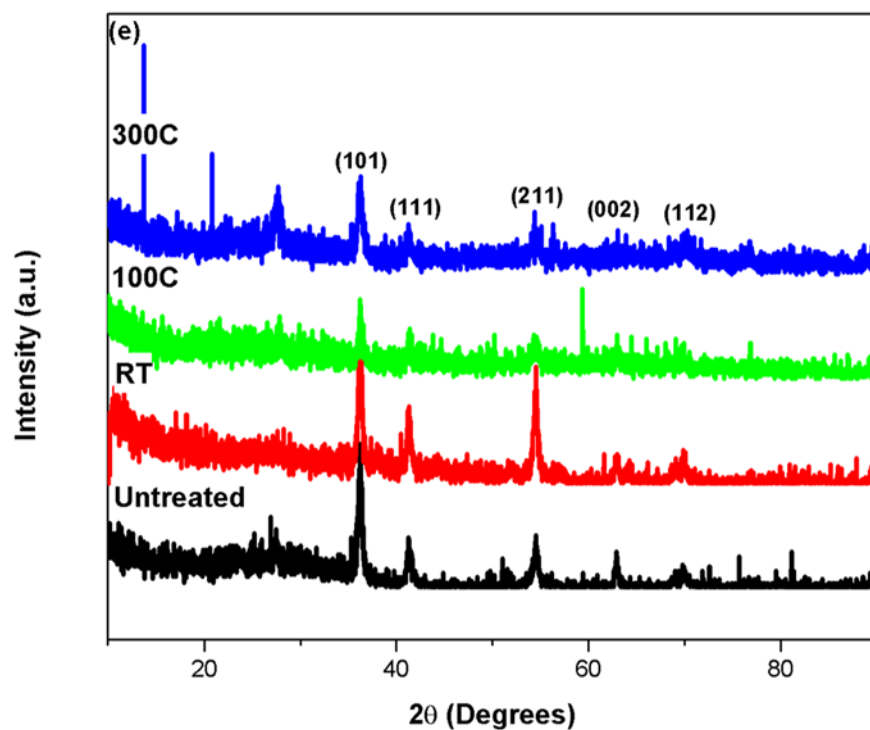
#### 4.4.2 Crystallinity and Structural Properties

Fig. 4.16 (a)-(d) and table 4.13 shows that the average crystalline grain-size decreases from 30 nm for substrate kept at room temperature, which remains largely unchanged at 29.8 nm and 30.1 nm

at annealing temperatures of 100 and 300°C, respectively. An increase in nanowire diameter post-N<sub>2</sub> plasma treatment can cause an increase in the lattice strain. It is observed by the W-H data of Fig. 4.16 (a)-(d) and table 4.13 that there is a trend for increasing lattice strain for an increasing N<sub>2</sub> plasma power. The increase is caused by the passivation of the dangling of Ti bonds deep in the TiO<sub>2</sub> matrix, due to reactive nitrogen species of the plasma during doping.







**Fig. 4.16** Williamson-Hall plot for: (a) untreated TiO<sub>2</sub>, (b) Nitrogen treated TiO<sub>2</sub> NWs at RT. (c) Nitrogen treated TiO<sub>2</sub> NWs at 100°C and (d) Nitrogen treated TiO<sub>2</sub> NWs 300°C. (3) Stacked raw GIXRD data for (hkl) planes of the temperature series

**Table 4.12:** Calculated Structural properties for the effect of temperature for treated TiO<sub>2</sub>

Parameter	TiO <sub>2</sub>	TiO <sub>2</sub> RT	TiO <sub>2</sub> 100°C	TiO <sub>2</sub> 300°C
Lattice Constants (a; c in nm)	0.461; 0.294	0.460; 0.295	0.455; 0.296	0.461; 0.296
Aspect Ratio (a/c)	1.57	1.56	1.54	1.56
Volume (x 10 <sup>-1</sup> nm <sup>3</sup> )	0.98	0.97	0.94	0.98
Crystallite Size (nm)	28.24	29.95	29.75	30.14
Strain (x 10 <sup>-3</sup> )	212.1	188.0	223.5	357

### 4.4.3 Chemical Bonding

Characterisation of the nitrogen treated TiO<sub>2</sub> samples with XPS are analysed and discussed. An exploration into the chemical composition of the surface bonding at the boundary of the intersecting nitrogen treated TiO<sub>2</sub> NW and pure TiO<sub>2</sub>, via high powered radio frequency process. Further analysis for comparison, the effects of the nitrogen doping were carried out for series of N<sub>2</sub> plasma temperature: Room temperature, 100°C and 300°C.

#### (a) Ti-2p Line-Shape

Fig. 4.17 compares the Ti 2p XPS plots of the TiO<sub>2</sub> nanowire arrays exposed to nitrogen plasma at substrate temperatures of room temperature, 100°C and 300°C to that of an untreated nanowire array. In all experiments, the power of exposure and exposure time were kept fixed at 300W and 30 mins, respectively. For the untreated sample of Fig. 4.17 (a) it can be seen that the 2p<sub>3/2</sub> to 2p<sub>1/2</sub> states are in a relative ratio of 44.89 to 55.11. This varies from the expected 1:1 ratio for TiO<sub>2</sub> as a result of the presence of oxygen vacancies throughout the TiO<sub>2</sub> lattice. When exposed to the nitrogen plasma at increasing power it can further be observed that the 2p<sub>3/2</sub> density of state decreases as a result of the formation of a Ti-N bond. At a substrate temperature of RT, 11.51% of the Ti-N state is observed. While, 28.43% of the 2p<sub>3/2</sub> state is observed and 60.07% of the 2p<sub>1/2</sub> state respectively. The Ti-N state decreases to 8.75% when increasing the substrate temperature to 100°C, with the 2p<sub>3/2</sub> and 2p<sub>1/2</sub> states at 31.55% and 59.72% respectively. At 300°C substrate temperature an increased for T-N% to 15.86%, while the Ti 2p<sub>3/2</sub> state decreases to 25.57% and 2p<sub>1/2</sub> state decreased to 58.57%. Fundamentally, the greater substrate temperature the greater the kinetic energy causing the Ti and O atoms to vibrate [4.8]. This increased vibration weakens the Ti-O bond, allowing for O atoms to be replaced with N atoms from the plasma.

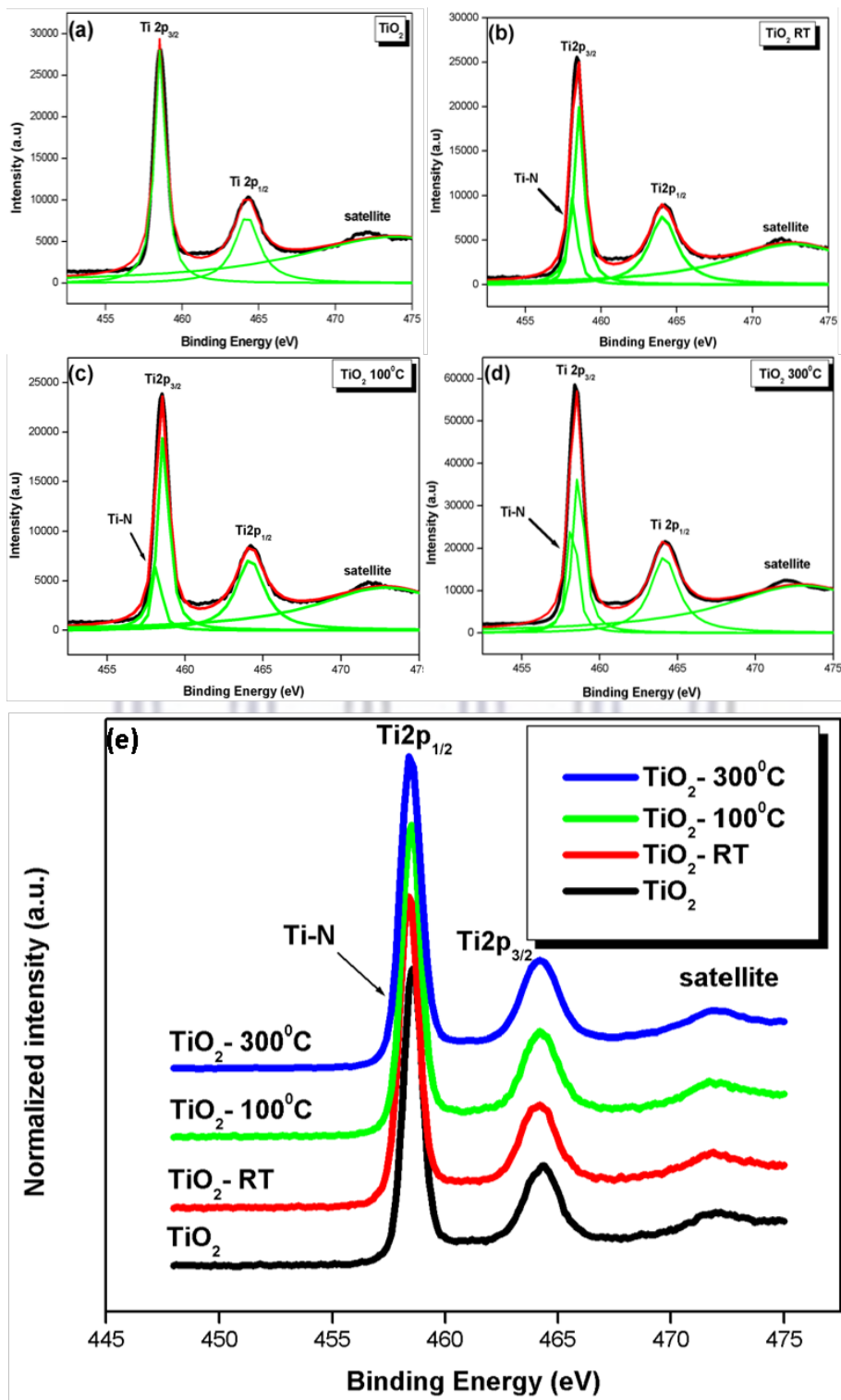


**Fig. 4.17**

Ti2p Xps plots for the deconvoluted treated TiO<sub>2</sub> NWs for the effect of temperature (a)-(d). Stacked xps plot for the effect of temperature (e)

**Table 4.13:** Relative quantum efficiencies of the de-convoluted Ti-2p

	TiO <sub>2</sub>	TiO <sub>2</sub> RT	TiO <sub>2</sub> 100°C	TiO <sub>2</sub> 300°C
Ti 2p <sub>3/2</sub> (f <sub>1</sub> )	5,22	5,22	5,22	5,22
Ti 2p <sub>1/2</sub> (f <sub>2</sub> )	2,68	2,68	2,68	2,68
Ti-N (f <sub>3</sub> )	5,22	5,22	5,22	5,22
Ti 2p <sub>3</sub> Area (A)	39298	25071	25544	51845
Ti 2p <sub>1</sub> Area (B)	24770	27198	24826	60976
Ti-N (C)	0	10150	7069,8	32153
(A/f <sub>1</sub> )	7528,35	4802,87	4893,49	9931,99
(B/f <sub>2</sub> )	9242,54	10148,51	9263,43	22752,24
(C/f <sub>3</sub> )	0,00	1944,44	1354,37	6159,58
(A/f <sub>1</sub> +B/f <sub>2</sub> + C/f <sub>3</sub> )	16770,89	16895,83	15511,29	38843,81
<b>Ti 2p<sub>3/2</sub> (%)</b>	<b>44,89</b>	<b>28,43</b>	<b>31,55</b>	<b>25,57</b>
<b>Ti 2p<sub>1/2</sub> (%)</b>	<b>55,11</b>	<b>60,07</b>	<b>59,72</b>	<b>58,57</b>
<b>Ti-N (%)</b>	<b>0,00</b>	<b>11,51</b>	<b>8,73</b>	<b>15,86</b>
<b>Total</b>	<b>100,00</b>	<b>100,00</b>	<b>100,00</b>	<b>100,00</b>

*(b) O-1s Line-Shape*

Fig. 4.18 compares the O1s XPS plots of the TiO<sub>2</sub> nanowire arrays substrate temperature heated at room temperature, 100°C and 300°C to that of an untreated nanowire array. In all experiments, the plasma power of 300W and elapsed time were kept fixed at 30 mins, respectively. After increasing the power, the bulk to surface ratio has changed to 64.01% and 35.99% for room temperature; 65.18% and 34.82% for 100°C and 61.81% and 38.19% for 300°C, respectfully. This observation of general increase in the bulk O-O bond and decrease in the Ti-OH surface bonds is evidence of substitutional N<sub>2</sub> bonding.

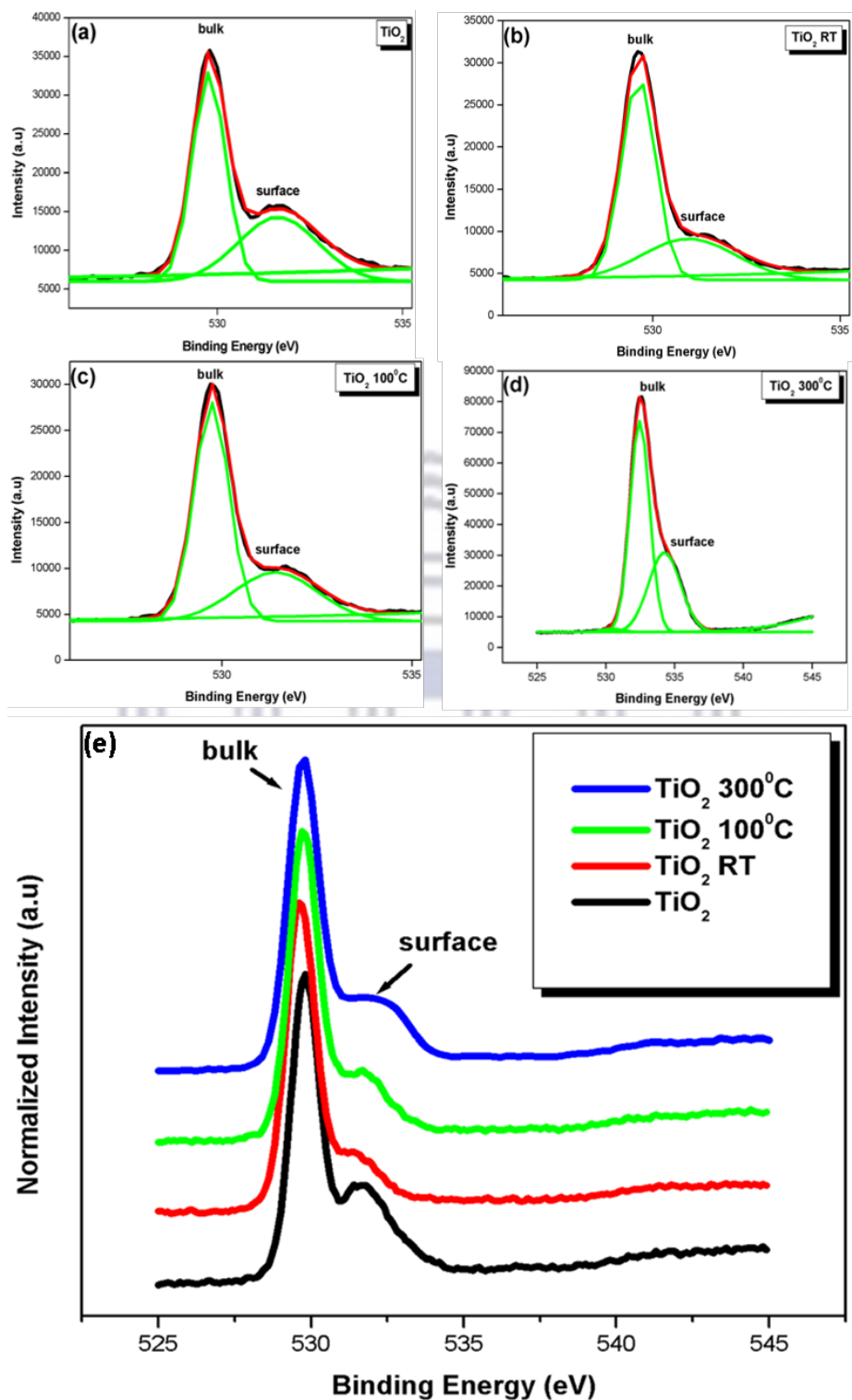


**Fig 4.18**

O1s XPS plots for the deconvoluted treated TiO<sub>2</sub> NWs for the effect of temperature (a)-(d). Stacked XPS plot for the effect of temperature (e)



**Table 4.14:** Relative quantum efficiencies of the de-convoluted O-1s

	TiO <sub>2</sub>	TiO <sub>2</sub> 10min	TiO <sub>2</sub> 30min	TiO <sub>2</sub> 60 min
Bulk (O-O)	2,93	2,93	2,93	2,93
Surface (Ti-OH)	2,93	2,93	2,93	2,93
Bulk (O-O) area	30375	27312	27465	74228,73
Surface (Ti-OH) area	22441	15359	14674	46424
(A/f <sub>1</sub> )	10366,89	9321,50	9373,72	25334,04
(B/f <sub>2</sub> )	7659,04	5241,98	5008,19	15844,37
(A/f <sub>1</sub> +B/f <sub>2</sub> )	18025,94	14563,48	14381,91	41178,41
<b>Bulk (O-O) %</b>	<b>57,51</b>	<b>64,01</b>	<b>65,18</b>	<b>61,52</b>
<b>Surface (Ti-OH) %</b>	<b>42,49</b>	<b>35,99</b>	<b>34,82</b>	<b>38,48</b>
<b>Total</b>	<b>100,00</b>	<b>100,00</b>	<b>100,00</b>	<b>100,00</b>

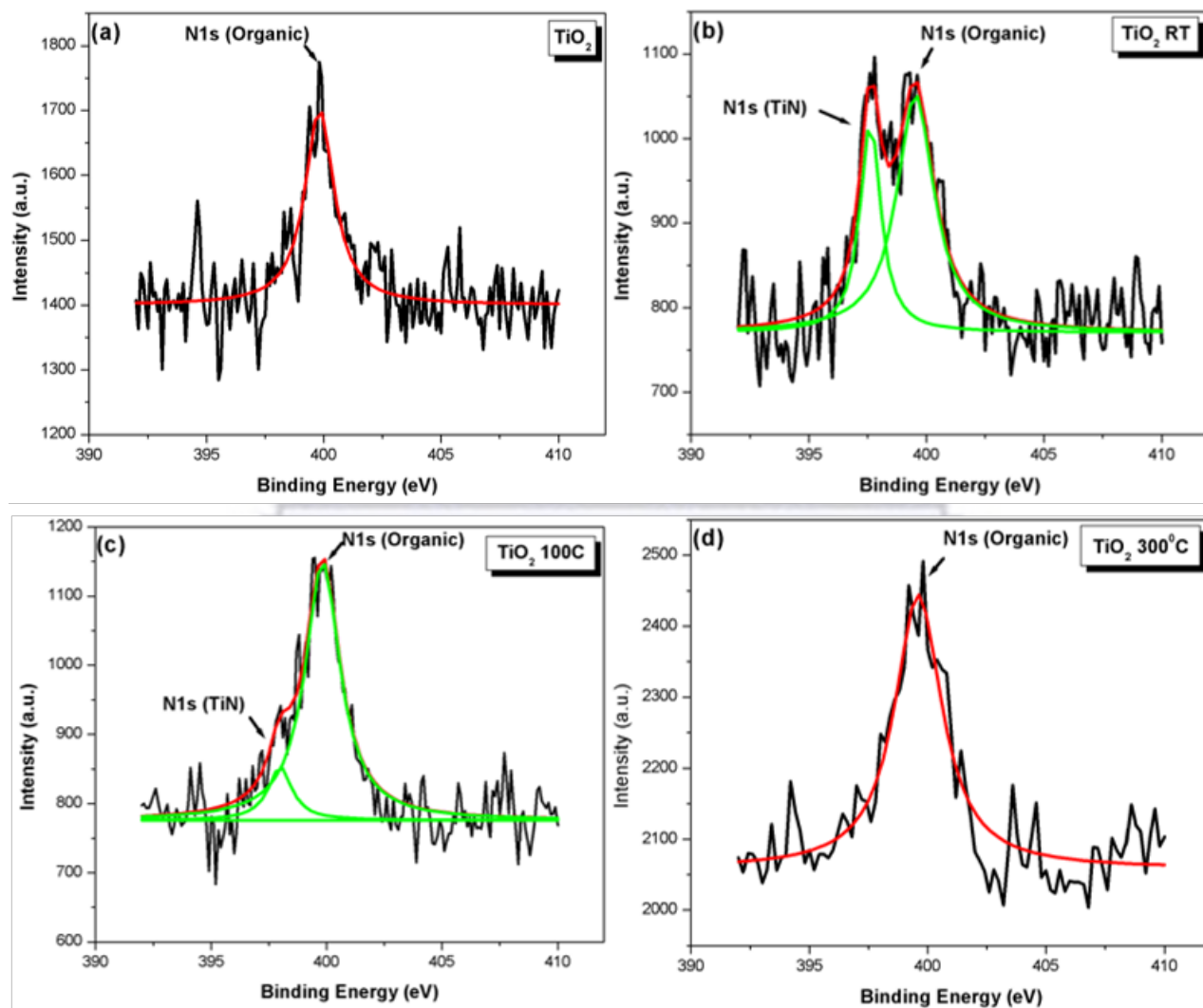
*(c) N-1s Line-Shape*

Fig. 4.19 compares the deconvoluted N1s XPS plots of the TiO<sub>2</sub> nanowire arrays exposed to 100, 300 and 500 W nitrogen plasma to that of an untreated nanowire array. In all experiments, the time of exposure and substrate temperature were kept fixed at 10 minutes and room temperature, respectively. Fig. 4.19 (a, b, c and d) all show a single N1s organic peak at 400 eV. Fig. 4.19 (b and c) both show a N1s (TiN) peak at 396.25 eV respectively. For Fig. 4.16 (b) it can be seen that the for the N1s organic to TiN<sub>states</sub> are in a relative ratio of 67.18% to 32.82%. For Fig 4.19 (c) it can be seen that the N1s organic to TiN<sub>states</sub> are in a relative ratio of 87.66% to 12.34%.

As in the power series, Cheng *et al* [4.12] reported on N1s peaks in a similar study. Therefore, a conclusion that the chemical states of the nitrogen doped into TiO<sub>2</sub> may be various and coexist in the form of substitutional N-Ti-O and Ti-N, also as interstitial NO/ NO<sub>2</sub> can be made. These multi-

type nitrogen doping can induce the formation of new energy level in the forbidden band of  $\text{TiO}_2$  and relate to the enhancement of photo-catalytic activity in the visible range [4.17].

Many of the substitutional-doped samples reported also show a small peak at 400 eV, indicating that they may contain some interstitial nitrogen as well and therefore it is not entirely reliable for evidence of a correlation between photocatalytic properties and either of the doping arrangements [4.18].



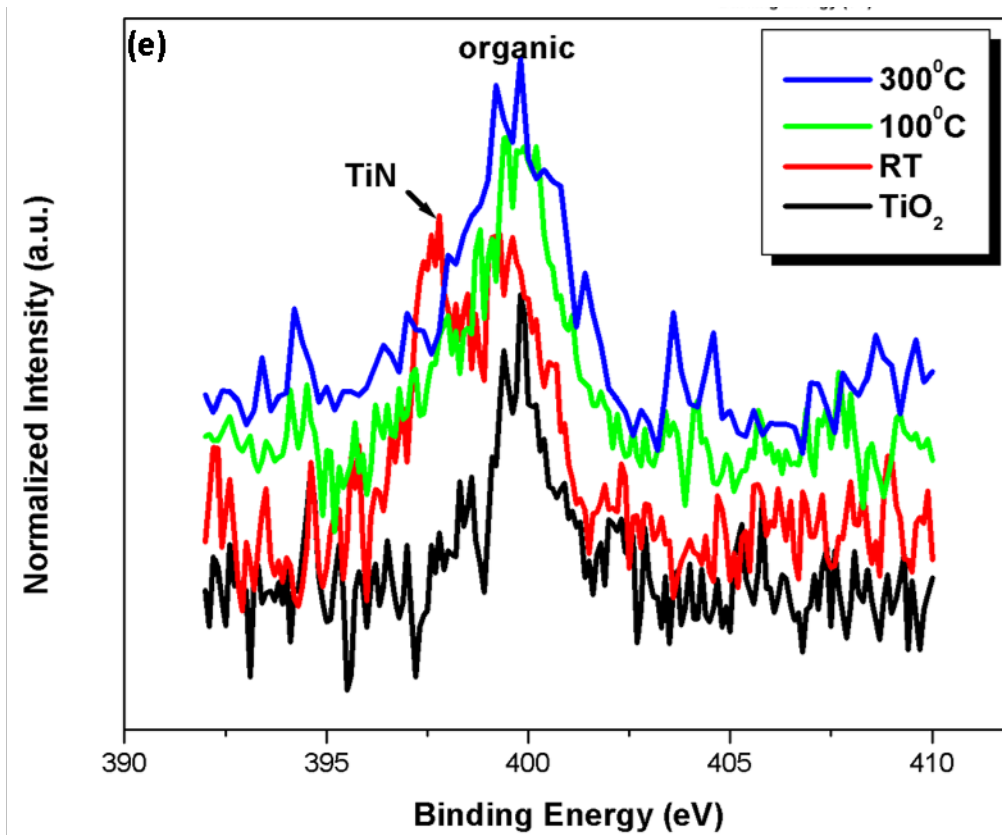


**Fig. 4.19:** N1s XPS plots for the deconvoluted treated TiO<sub>2</sub> NWs for the effect of temperature (a)-(d). Stacked XPS plot for the effect of temperature (e)

UNIVERSITY of the  
WESTERN CAPE

**Table 4.15:** Relative Quantum efficiencies of the de-convoluted N1s

	TiO <sub>2</sub>	TiO <sub>2</sub> RT	TiO <sub>2</sub> 100°C	TiO <sub>2</sub> 300°C
N1s (Organic)	1,8	1,8	1,8	1,8
N1s (TiN)	1,8	1,8	1,8	1,8
N1s (Organic)	709,6348	850,4	1077,2	1472,8
N1s (TiN)	0	415,52	151,7	0
(A/f <sub>1</sub> )	394,24	472,44	598,44	818,22
(B/f <sub>2</sub> )	0,00	230,84	84,28	0,00
(A/f <sub>1</sub> +B/f <sub>2</sub> )	394,24	703,29	682,72	818,22
<b>N1s (Organic)%</b>	<b>100,00</b>	<b>67,18</b>	<b>87,66</b>	<b>100,00</b>
<b>N1s (TiN)%</b>	<b>0,00</b>	<b>32,82</b>	<b>12,34</b>	<b>0,00</b>
<b>Total</b>	<b>100,00</b>	<b>100,00</b>	<b>100,00</b>	<b>100,00</b>

#### 4.4.4 Optical Properties

The change in substrate temperature does not change the transmission properties much between room temperature and 100 °C as shown in Fig. 4.20 This is to be expected as the TiO<sub>2</sub> lattice is stable in this temperature range. Again, as shown, the transmission peaks above 60% in the UV-Vis range, with the exception being the 300°C sample peaking at 22.1%. A sharp cut-off at approximately 400 nm is observed for the samples. Individually, the transmittance for each sample stabilises around 900 nm at: 63.9 % for untreated TiO<sub>2</sub>, 60.3 % for RT and 59.8 % for 30 min. A possibly reason for the transmittance varying may be due to the structure of the nanowires. Tables 4.13 and 4.14 indicate a large diameter coupled with a large nanowire length for the 300°C sample as compared to the RT and 100°C samples. Also seen in Fig 4.12 is a greater amount of alignment in the nanowire array for the 300°C samples as compared to both the RT and 100°C samples. These nanowires seen in Fig 4.12 for the 300°C sample therefore seem to inhibit transmission of light in

both the visible and near-infrared regions. It can be postulated that nanowires at these experimental conditions absorb light in the UV and near-IR regions through total internal reflection, given the much denser nanowire array.

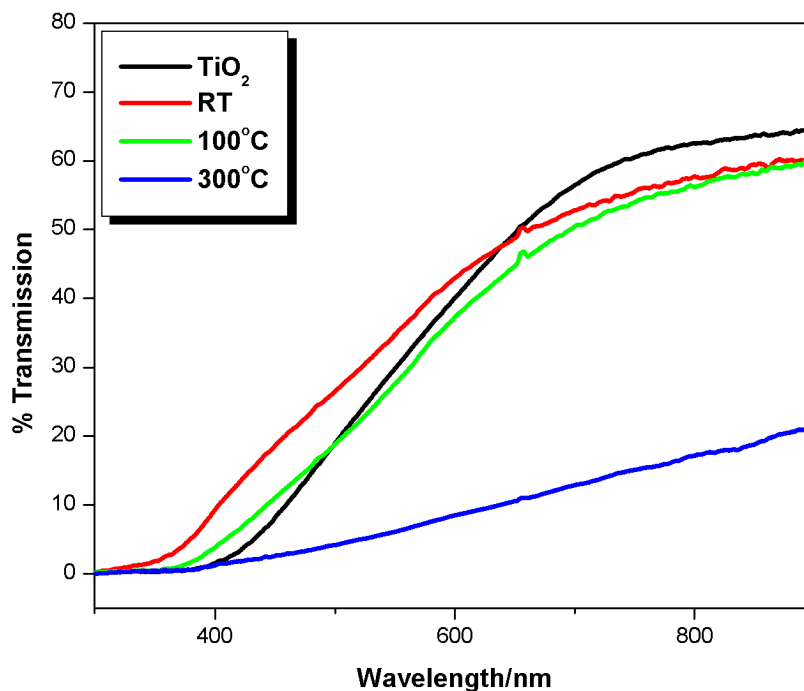


**Fig. 4.20:** UV-Vis transmission spectra of the N<sub>2</sub> plasma treated nanowire array on the FTO substrate. With the stacked raw patterns: (black) untreated TiO<sub>2</sub>, (red) Room Temperature, (green) 100°C, (blue) 300°C



## References

- [4.1] A. Wisnet, S. Betzler, R. Zucker, J. Dorman, P. Wagatha, S. Matich, C. Scheu, “*Model for hydrothermal growth of rutile wires and the associated development of defect structures*”, *Crystal Growth & Design* 14 (2014) 4658
- [4.2] B. Muhammad, N. Peterson, L. Kotsedi, F. Cummings, “*RF nitrogen plasma irradiation of metal-doped TiO<sub>2</sub> nanowire arrays as an effective technique for improved light transmission and optical bandgap manipulation*”, *Chem. Phys.* 538 (2020) 110922
- [4.3] Z. Zhou, J. Fan, X. Wang, W. Zhou, Z. Du, S. Wu, “*Effect of highly ordered single crystalline TiO<sub>2</sub> nanowire length on the photovoltaic performance of dye-sensitised solar cells*”, *ACS Appl. Mat. Int.* 8 (2011) 4349
- [4.4] G. Yuan, W. Zhang, J. Jie, X. Fan, J. Zapien, Y. Leung, L. Luo, P. Wang, C. Lee, S. Lee, “*P-type ZnO nanowire array*”, *Nano. Lett.* 8 (2008) 2591
- [4.5] S. Guimond, U. Schütz, B. Hanselmann, E. Körner, D. Hegemann, “*Influence of gas phase and surface reactions on plasma polymerisation*”, *Surf. Coatings Tech.* 205 (2011) 447
- [4.6] L. Youssef, S. Roualdès, J. Bassil, M. Zakhour, V. Rouessac, C. Lamy, M. Nakhil, “*Effect of plasma power on the semiconducting behavior of low-frequency PECVD TiO<sub>2</sub> and nitrogen-doped TiO<sub>2</sub> anodic thin coatings: photo-electrochemical studies in a single compartment cell for hydrogen generation by solar water splitting*”, *J. Appl. Electrochem.* 49 (2018) 135
- [4.7] V. Mote, Y. Purushotham, B. Dole, “*Williamson-Hall analysis in estimation of lattice strain in nanometer-sized ZnO particles*”, *J. Th. Appl. Phys.* 6 (2012) 6
- [4.8] T. Morikawa, R. Asahi, T. Ohwaki, K. Aoki, Y. Taga, “*Band-gap narrowing of titanium dioxide by nitrogen doping*”, *Jap. J. Appl. Phys.* 40 (2001) 561
- [4.9] J. Frandon, B. Brousseau, F. Pradal, “*Electronic excitations in in rutile TiO<sub>2</sub> and TiO measurement energy losses of electrons between 3 and 60 eV*”, *I. Phys.* 80 (1978) 839
- [4.10] T. Sham, M. Lazarus, “*X-ray photoelectron spectroscopy (XPS) studies of clean and hydrated TiO<sub>2</sub> on (Rutile) surfaces*”, *New York* 68 (1979) 2-3
- [4.11] H. Chermette, P. Pertosa, F. Calendini, “*Molecular orbital study of satellites in XPS spectra of BaTiO and TiO<sub>2</sub>*”, *Chem. Phys. Let.* 69 (1979) 2

- [4.12] X. Cheng, X. Yu, Z. Xing, J. Wan “Enhanced photocatalytic activity of nitrogen doped  $TiO_2$  anatase nano-particle under simulated sunlight irradiation”, E. Procedia 16 (2012) 598
- [4.13] Z. Wang, W. Cai, X. Hong, X. Zhao, F. Xu, C. Cai, “Photocatalytic degradation of phenol in aqueous nitrogen-doped  $TiO_2$  suspensions with various light sources”, Appl. Cat. B. 57 (2005) 223
- [4.14] G. Zhang, X. Ding, F. He, X. Yu, J. Zhou, Y. Hu, J. Xie, “Preparation and photocatalytic properties of  $TiO_2$ -montmorillonite doped with nitrogen and sulfur”, J. Phys. Chem. Solids 69 (2008) 1102
- [4.15] S. Sakthivel, H. Kisch, “Photocatalytic and photoelectrochemical properties of nitrogen-doped titanium dioxide”, Chem. Phys. 4 (2003) 487
- [4.16] J. Xu, J. Li, W. Dai, Y. Cao, H. Li, K. Fan, “Simple fabrication of twist-like helix N, S-codoped titania photocatalyst with visible-light response”, Appl. Cat. B: Env. 79 (2008) 72
- [4.17] C. Dunnill, I. Parkin, “Nitrogen-doped  $TiO_2$  thin films: photocatalytic applications for healthcare environments”, Dalton Trans. 40 (2011) 1635
- [4.18] C. Huang, L. Chen, K. Cheng, G. Pan, “Effect of nitrogen plasma surface treatment to the enhancement of  $TiO_2$  photocatalytic activity under visible light irradiation”, J. Mol. Cat. Appl. Chem. 261 (2007) 218
- [4.19] M. Barakat, R. Kumar, “Photocatalytic activity enhancement of titanium dioxide nanoparticles”, Springer Br. Mol. Sci. 1 (2016) 1
- [4.20] H. Ishihara, J. Bock, R. Sharma, F. Hardcastle, G. Kannarpady, M. Mazumber, A. Biris, “Electrochemical synthesis of titania nanostructure arrays and their surface modification for enhanced photoelectrochemical hydrogen production”, Chem. Phys. Lett. 489 (2010) 81
- [4.21] A. Franco, G. Zambrano, M. Gómez, “Photocatalytic activity of nitrogen-doped and undoped titanium dioxide sputtered thin films”, Superf. Vacío. 25 (2012) 1
- [4.22] J. Dhar, A. Mondal, S. Bhattacharya, N. Singhl, C. Ngangbam, K. Chattopadhyay, “Band gap tailoring of  $TiO_2$  nanowires by nitrogen doping under  $N_2/Ar$  Plasma Environment, Journal of Nanoscience and Nanotechnology”, J. Nano. Nanotech. 15 (2015) 3951
- [4.23] M. Wang, H. Lin, C. Wang, W. Hsuan-Chung, “Effects of annealing temperature on the photocatalytic activity of N-doped  $TiO_2$  thin films”, Ceram. Int. 38 (2012) 195

- [4.24] N. Martin, C. Rousselot, D. Rondot, F. Palmino, R. Mercier, “*Microstructure modification of amorphous titanium oxide thin films during annealing treatment*”, Th. Sol. Films 300 (1997) 113



## Chapter 5: Summary and Future Work

---

This study investigated the morphological, structural and optical properties resulting from the introduction of nitrogen plasma species as dopants in hydrothermally grown TiO<sub>2</sub> NWs.

Findings of Chapter 4 on the effect of doping showed N-doping under increasing power leads to dissociation of the electrostatic Van der Waals forces bundling apices of nanowires, resulting in non-aligned NW arrays post N<sub>2</sub> treatment – these may be advantageous and can improve the electron–hole dissociation interface during device operation of organic-photovoltaics. Furthermore, the increase in nanowire diameter with increasing plasma power may well be due to domination by the species-species collisions, subsequently increasing the growth rate. It was found that fundamentally, the higher plasma power, the greater the kinetic energy of the plasma species. With high kinetic energy, the N<sub>2</sub> plasma has a greater probability of dislodging an oxygen atom from the Ti-O bond, thereby replacing the oxygen with nitrogen forming a Ti-N bond. Moreover, a further observation is the clear shift in transmission towards longer wavelengths. This red-shift is directly assigned to the onset of the absorption curve at lower energy levels, which in turn, can be related to the increase in nitrogen doping at higher plasma power irradiation; nitrogen doping is well-known to decrease the optical bandgap of TiO<sub>2</sub>.

Similarly, increasing the exposure time also allows the plasma radicals to significantly distort the Van Der Waals electrostatic forces and as such the orientation of the nanowires to the FTO substrate. On a fundamental level, findings showed that the greater the elapsed time, the greater the probability for collision between the N<sub>2</sub> plasma and the nanowire array, which in turn results in greater doping of the sample. The XPS spectra showed a general trend, whereby the O-O bonds in the bulk of the sample decrease with increasing nitrogen plasma exposure time. This decrease in O-O bonds coincides with the increase of the surface Ti-OH bonds. This may be due to increased substitutional N-Ti-O and Ti-N as the O bonds are decreasing. However, it was observed that exposure time is inhibited when samples are exposed to a plasma power of 100 W – this may be as a result of nitrogen radicals with insufficient kinetic energy, preventing deep-level doping in the TiO<sub>2</sub> lattice.

Increasing the substrate temperature during irradiation showed that at higher temperatures, the polycrystalline structure forms with greater amounts of rutile. Previous literature state that nitrogen introduced in the TiO<sub>2</sub> lattice has a direct relation on both the crystallinity and electronic properties of the material. In this work, a similar trend was observed when increasing the substrate temperature to increasing the plasma power. Therefore, a conclusion that the chemical states of the nitrogen doped into TiO<sub>2</sub> may be various and coexist in the form of substitutional N-Ti-O and Ti-N, also as interstitial NO/ NO<sub>2</sub> can be made. These multi-type nitrogen doping can induce the formation of new energy level in the forbidden band of TiO<sub>2</sub> and relate to the enhancement of photo-catalytic activity in the visible range for controlled fabrication.

It was therefore concluded that for N-doped TiO<sub>2</sub> aligned NWs, controlled doping with lengths of 1 μm, minimal structural defects, successful implantation of N atoms from the plasma, optical transmission shifts towards longer wavelengths is as follows: A plasma power of 300W, exposure time of 30 min and a substrate temperature of 100°C.

Future optimisations include a more in-depth study into the effect of power, exposure time and temperature for N-doped TiO<sub>2</sub> NWs. Greater plasma power, longer exposure times and higher substrate temperature effects to be studied. A possible investigation into the effect of flow rate of the N<sub>2</sub> and Ar<sub>2</sub> plasmas on TiO<sub>2</sub> NWs. Furthermore, as the scope of this study was limited to synthesis and effect of controlled doping, future work may lead to investigations of the fabrication of a N-TiO<sub>2</sub> photovoltaic device. With the additional step of device testing and optimisations of the device as compared to optimisations of the N-doped TiO<sub>2</sub> NWs.